



BRNO UNIVERSITY OF TECHNOLOGY

VYSOKÉ UČENÍ TECHNICKÉ V BRNĚ

CENTRAL EUROPEAN INSTITUTE OF TECHNOLOGY

STŘEDOEVRÓPSKÝ TECHNOLOGICKÝ INSTITUT

**X-RAY NANO COMPUTED TOMOGRAPHY OF
STRUCTURED POLYMERIC BIOMATERIALS**

RENTGENOVÁ POČÍTAČOVÁ NANO TOMOGRAFIE POLYMERNÍCH STRUKTUROVANÝCH BIO
MATERIÁLŮ

DOCTORAL THESIS

DIZERTAČNÍ PRÁCE

AUTHOR

AUTOR PRÁCE

Ing. Dominika Kalasová

SUPERVISOR

VEDOUCÍ PRÁCE

prof. Ing. Jozef Kaiser, Ph.D.

BRNO 2019

Summary

This thesis is focused on an advanced imaging method X-ray computed nanotomography (CT). This non-destructive technique is used for the research of various biomaterials in tissue engineering and material science in general (scaffolds, polymers, ceramics, composites, etc.). Visualisation and quantification in 3D are advantageous in multidisciplinary approach usually applied in these fields. The objective of the thesis is divided into two topics. The first topic is about optimisation of the measurement procedure for various soft materials by CT with the laboratory X-ray sources. Mostly, the phase contrast propagation-based CT imaging (PBI) is involved here. This work theoretically describes the PBI and demonstrates this phenomenon via several sets of measurements. The necessary post-processing of PBI data is implemented and evaluated based on data quality enhancement. The second topic shows specific applications of CT in material engineering. Several studies with different CT devices show a few examples of possible applications and image processing options. Examples of correlation of CT with other complementary techniques show how CT can be applied in a multidisciplinary approach to solving complex scientific problems.

Abstrakt

Tato práce se zaměřuje na pokročilou zobrazovací technologii, rentgenovou počítačovou tomografií (CT). Tato nedestruktivní technika je využívána pro výzkum různých biomateriálů ve tkáňovém inženýrství a materiálové vědě obecně (skafoldy, polymery, keramické materiály, kompozity aj.). Vizualizace a kvantifikace ve 3D jsou výhodné v rámci multidisciplinárního přístupu, který je často v těchto odvětvích uplatňován. Záměr této práce lze rozdělit do dvou oblastí. Prvním tématem je optimalizace měřicí procedury různých měkkých materiálů pomocí CT s laboratorními rentgenovými zdroji. To zahrnuje převážně zobrazování ve fázovém kontrastu, konkrétně metodu volného šíření záření (VŠZ). Tato práce teoreticky popisuje VŠZ a demonstruje tento jev na řadě experimentů. Následné nezbytné zpracování dat získaných VŠZ je implementováno a vyhodnoceno na základě míry zlepšení obrazových dat. Druhé téma ukazuje konkrétní aplikace CT v materiálovém inženýrství. Několik studií s různými CT zařízeními ukazuje příklady možných aplikací a obrazového zpracování. Příklady korelace CT dat s jinými doplňkovými technikami ukazují, jak může být CT aplikována v multioborovém přístupu ke komplexnímu řešení vědeckých problémů.

Keywords

X-ray computed tomography, nanotomography, nCT, phase contrast, phase retrieval, polymers, biomaterials

Klíčová slova

rentgenová počítačová tomografie, nanotomografie, nCT, fázový kontrast, polymery, biomateriály

KALASOVÁ, Dominika. *X-ray nano computed tomography of structured polymeric biomaterials*. Brno, 2019. 84 pp. Doctoral thesis. Brno University of Technology. Central European Institute of Technology. Supervisor Jozef KAISER.

Rozšířený abstrakt

Tato práce se zaměřuje na pokročilou zobrazovací technologii, rentgenovou počítačovou tomografií (CT). Tato nedestruktivní technika je využívána pro výzkum různých biomateriálů ve tkáňovém inženýrství a materiálové vědě obecně (skafoldy, polymery, keramické materiály, kompozity aj.). Vizualizace a kvantifikace ve 3D pomocí CT jsou výhodné v rámci multidisciplinárního přístupu, který je často v těchto odvětvích uplatňován.

Záměr této práce lze rozdělit do dvou oblastí. Prvním tématem je optimalizace měřicí procedury měkkých materiálů pomocí CT zařízení s laboratorními rentgenovými zdroji. To zahrnuje převážně zobrazování ve fázovém kontrastu, konkrétně metodu volného šíření záření (VŠZ). V této práci je popsán princip VŠZ a uvedené vztahy jsou aplikovány na popis jednotlivých CT zařízení. Na základě jejich analýzy jsou CT zařízení hodnocena z hlediska možností využití VŠZ. Jev je demonstrován na řadě experimentů měření polymerového kompozitu za různých nastavení přístroje. Následně nezbytné zpracování dat získaných VŠZ ve formě tzv. algoritmů pro získání fáze je implementováno a vyhodnoceno na základě míry zlepšení obrazových dat. Byl navržen software pro implementaci několika těchto algoritmů v případě CT zařízení RIGAKU nano3DX. Tento software bude implementován do oficiálního software firmy.

Druhé téma představuje některé konkrétní aplikace CT v materiálovém inženýrství. Několik studií s různými CT zařízeními ukazuje příklady možných využití VŠZ pro biomateriály a obrazovou analýzu dat. Jednou z aplikací je zobrazování buněk ve skafoldech. Je ukázáno zobrazení jak jednotlivých buněk s velkým rozlišením, tak i většího množství materiálu, což umožňuje celkové zhodnocení většího objemu vzorku. Druhým příkladem je analýza pórovitosti hydroxyapatitové pěny. Příklady korelace CT dat s jinými doplňkovými technikami ukazují, jak může být CT aplikována v multioborovém přístupu ke komplexnímu řešení vědeckých problémů. Je ukázána kombinace CT, skenovacího elektronového mikroskopu a světelné mikroskopie na vzorku skafoldu a kombinace CT, 3D energově disperzní spektroskopie a světelné mikroskopie na vzorku vápence.

Konkrétním přínosem práce je rozšíření expertízy Laboratoře rentgenové počítačové tomografie na CEITEC VUT v oblasti zobrazování ve fázovém kontrastu. Implementace této metody na konkrétních tématech z materiálových věd rozšiřuje možnosti charakterizace především materiálů složených z lehkých prvků. Obecně tato práce přispívá k zavedení rentgenové počítačové tomografie jako běžné techniky k 3D zobrazování a analýze biologických vzorků. Nejdůležitější výsledky práce jsou autorkou publikovány v odborných impaktovaných časopisech a byly prezentovány na mezinárodních konferencích.

I declare that I carried out this doctoral thesis *X-ray nano computed tomography of structured polymeric biomaterials* independently, and only with the cited sources, literature and other professional sources.

Ing. Dominika Kalasová

I would first like to thank my supervisor, prof. Ing. Jozef Kaiser, Ph.D., for guiding me through my Ph.D. studies and for providing opportunities. I would also like to thank all the colleagues from the Laboratory of X-ray micro and nano computed tomography at CEITEC BUT, namely its leader, Ing. Tomáš Zikmund, Ph.D., and fellow Ph.D. candidates and researchers, for their advice, comments, patience and relaxing moments while drinking coffee. I want to express my gratitude to colleagues I met at my internships abroad, Dr. Kazuhiko Omote and Dr. Yoshihiro Takeda from RIGAKU company, Japan, and prof. Markku Kataja and Dr. Joni Parkkonen from University of Jyväskylä, Finland, for their kindness, hospitality, professional advice and beautiful memories. Thanks to RNDr. Karel Kolář, Ph.D., for accepting the Ph.D. thesis writing challenge and congratulations to finish two months earlier. Finally, last but by no means least, I am also grateful to my family, especially my parents and Michal, for being with me all the time.

Ing. Dominika Kalasová

Contents

Introduction	1
1. Literature review	3
1.1. Principles	3
1.1.1. X-ray sources	3
1.1.2. Interaction of X-rays with matter	4
Linear attenuation coefficient	4
Atomic form factor	7
Index of refraction in X-ray region	8
Transmission function	8
1.1.3. Image reconstruction	9
1.1.4. Databases of materials properties in X-ray region	14
1.2. Phase contrast imaging	14
1.2.1. Propagation-based imaging	15
1.2.2. Phase retrieval	19
Paganin algorithm (PA)	19
Modified Bronnikov Algorithm (MBA)	20
Bronnikov Aided Correction (BAC)	20
1.3. Technology	21
1.3.1. Medical CT	21
1.3.2. MicroCT, μ CT	22
1.3.3. Sub- μ CT, nCT	22
2. Aims of thesis	25
2.1. Propagation-based phase contrast imaging	25
2.2. Applications on biomaterials	25
3. Methods	27
3.1. CT devices	27
3.2. Software	30
3.3. Image evaluation parameters	30
4. Propagation-based imaging	33
4.1. Characterization of lab-CT systems for PBI	33
4.1.1. PBI on nano3DX	33
4.1.2. PBI on HeliScan	34
4.2. Phase retrieval implementation	36
4.2.1. Influence of phase retrieval on image quality	36

4.2.2.	Matlab GUI	38
4.2.3.	Optimisation of phase retrieval parameters	40
4.2.4.	Comparison of phase retrieval algorithms	43
4.3.	Optimisation of measurement parameters for PBI with nano3DX	46
5.	Applications	55
5.1.	Scaffolds with cells	55
5.1.1.	High resolution: single cell	57
5.1.2.	Large field of view: statistical evaluation	59
5.2.	Porosity of open foam structures	61
5.3.	Correlation of CT data with 2D imaging techniques	62
5.3.1.	nCT, SEM and LM of scaffolds	62
5.3.2.	CT, 3D EDS analysis and LM of limestone	63
	Conclusion	65
	References	67
	List of symbols and shortcuts	81
	A. Supplementary data	i
	B. Publications	iii

Introduction

X-ray computed tomography (CT) is a nondestructive method for imaging of materials. In principle, it acquires 3D information about the sample via a set of X-ray projections under different angles of a sample's rotation. In such a CT scan, an inner structure of an object is visualised. Based on the different response of materials to X-rays, an absorption or phase contrast can be measured or derived from the X-ray projections. In CT data, it is possible to get a slice through an object in an arbitrary direction. Various materials and structures can be distinguished, segmented and further analysed. Apart from visualisation, a number of useful information can be derived – size, volume, surface, 3D distribution, porosity, etc., and a variety of analyses including dimensional measurements and modelling of physical properties can be performed.

Many fields of science and industry take advantages of CT. The main features used by industry follow the quality control – dimensional measurements of otherwise inaccessible parts, comparison of manufactured parts to a CAD model, control of geometrical tolerances, various analyses of porosity, fibre orientation and wall thickness, etc. Some of them are also used in the science field. In the case of biomaterials, the challenge of segmentation, e.g. of determination of surface/border of different materials, is often more difficult than in industry. The reason is that those materials contain a lot of various structures, which may have similar or low contrast to be distinguished easily. Often, some a priori knowledge about the sample is needed. The purpose of the further analysis is often case-dependent and requires the development of specific post-processing procedures, usage of specialised CT software or utilisation of advanced programming methods.

Obtaining CT data of structures from biomaterials and establishing a meaningful post-processing method is a challenging task. They are composed of light materials with low X-ray absorption and/or contrast, which makes use of absorption CT used in industry difficult or even impossible. This can be overcome by staining of the sample with heavier elements or by use of phase contrast imaging methods. The latter requires careful mathematical post-processing of X-ray projections to get meaningful data. Once the CT data are acquired, and the desired structures are visible, the segmentation and quantification bring another challenge for both CT-devoted software and programmers working with image analysis. To get a reliable interpretation of CT data, often additional 2D/3D imaging methods are required to complement CT results and to establish the technique in the framework of currently used methods.

In the first chapter of this thesis, a literature review regarding the CT imaging of biomaterials topic is given. It includes subsections explaining principles of CT technique, selected topics from physics of X-ray imaging with the emphasis on materials with a low atomic number, phase contrast imaging focusing on laboratory-based X-ray sources and insight into state-of-the-art CT technology with a description of terminology used in this

INTRODUCTION

work. The second chapter sums up the aims of the thesis. In the third chapter, the CT devices, software and image evaluation tools used in this thesis are described.

The next two chapters form the main content of the thesis. The fourth chapter explores the propagation-based method of phase contrast imaging with laboratory-based X-ray sources from the theoretical and experimental point of view. It includes characterisation of two laboratory-based CT systems for propagation-based imaging (PBI), implementation and optimisation of phase retrieval algorithms and optimisation of measurement parameters for PBI. In chapter five, examples of phase contrast imaging and subsequent post-processing of light materials are shown. The most important results from the fourth and fifth chapter are published in impacted journals. Some of the results were presented at international conferences. All of the first-author publications, four in total, are included in the Appendix.

1. Literature review

The first section describes principles of CT technique from X-ray radiation, its origin and interaction with matter up to image reconstruction. The second section describes phase contrast imaging, as it is the primary CT examination method applied in this thesis. In the third section, a review of CT technology nowadays available is given.

1.1. Principles

In CT measurements, the sample is placed on a rotating table between the X-ray tube and the detector. Projections from different angles of rotation of the sample are recorded. From these projections slices through the sample are reconstructed and stacked to get 3D data. In this section, principles and technical details of these steps are explained.

1.1.1. X-ray sources

X-ray radiation is part of the electromagnetic spectrum with frequencies 30 PHz–30 EHz, wavelengths 10 pm–10 nm or energies 100 eV–100 keV. In general, there are two cases when X-rays are emitted: when a charged particle is moving with non-zero acceleration and when electrons change their position between atomic orbitals. [1]

The X-ray source used in laboratory CT devices is schematically shown in Fig. 1.1. Electrons are emitted from a cathode made of a heated filament (most often W) and accelerated by a potential difference to a metal target (most often Cu, Mo, Cr, Ag or W). The acceleration voltage usually fits into the interval 30 kV–450 kV. [1]

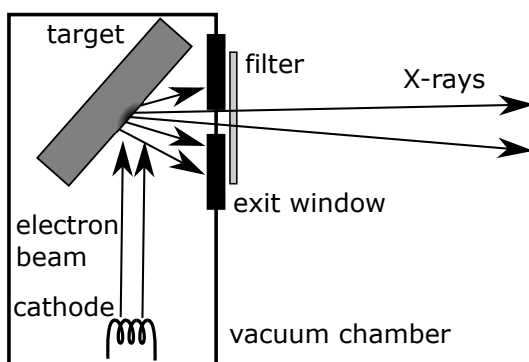


Figure 1.1: Scheme of a laboratory X-ray source.

When electrons hit the target, they interact with the material. Most of their energy (over 99%) is dissipated as heat. An accelerated electron is, in the proximity of an atom nucleus, slowed down and is emitting braking radiation (Fig. 1.2). It is a continuous

1. LITERATURE REVIEW

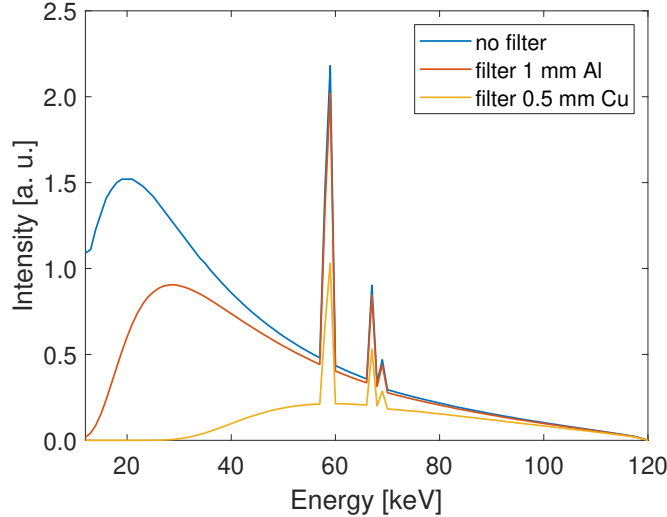


Figure 1.2: X-ray spectrum of a tungsten target for incident electrons with the energy of 120 keV, with use of 1 mm of Al filter and 0.5 mm of Cu filter. The spectra were generated by the SpecCalc software [2].

spectrum of energies, and the largest one equals to the energy emitted by electron if it hits the nucleus directly. Low energies are usually filtered out by filters placed directly by X-ray tube window. The overall intensity of breaking radiation is directly proportional to an atomic number of protons, therefore the efficiency of emitting breaking radiation is higher for materials with higher atomic number [1, 3].

Peaks in breaking radiation are characteristic peaks of the material of the target (Fig. 1.2). They are emerged when impinging electron removes an electron from inner atomic shells (K, L, M, ...). The free space gets occupied by an electron from a more energetic shell. During the electron transfer between the shells, an energy equal to the energetic difference between the shells is released. These energies are typical for every material. [1]

Another significant X-ray source is a synchrotron. Electrons are accelerated by an electric field in a linear accelerator and later in a ring. A direction of their trajectory is controlled by magnetic fields. Electric and magnetic fields are synchronised with particles' movement so that the particles are moving with a speed of light. High-energetic particles emit X-ray radiation when they experience centripetal acceleration. Synchrotron X-ray sources provide, in comparison with laboratory sources, high-flux X-ray beam with a high degree of coherence. With the use of Bragg crystals, it is possible to get very monochromatic beam and tune its energy. Many experiments take advantage of synchrotron radiation to perform experiments in phase contrast or 4D CT measurements. [1]

1.1.2. Interaction of X-rays with matter

Linear attenuation coefficient

For a monochromatic radiation of intensity I_0 , the intensity I of radiation passing through a material of thickness x is given by Beer-Lambert law

$$I = I_0 \exp(-\mu x),$$

where μ is the linear attenuation coefficient. μ is related to a mass attenuation coefficient $\mu_{\text{mass}} = \mu/\rho$, where ρ is a density of a material. [1]

In general, the coefficient μ varies within the sample: $\mu = \sum_i N_i \sigma_i$, where σ_i is the attenuation cross-section of the atoms with number density N_i and the summation is over all attenuating species i . For a beam moving along the line Φ^1 (Fig. 1.3), the Beer-Lambert law takes the form of

$$I = I_0 \exp \left(- \int_{\Phi} \mu dt \right) = I_0 \exp \left(- \int_{\Phi} \sum_i N_i \sigma_i dt \right). \quad (1.1)$$

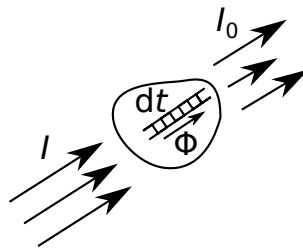


Figure 1.3: Each voxel (a volumetric element with dimension dt in the direction of the line Φ) contributes to total linear attenuation coefficient μ . [1]

For a monochromatic, resp. a polychromatic beam of photons with different energies E , the intensity after passing through the sample is given as

$$I = I_0 \exp \left(- \int_{\Phi} \mu dt \right), \quad \text{resp.} \quad I = \int_E j_0(E) \exp \left(- \int_{\Phi} \mu(E) dt \right) dE,$$

where $j_0(E)$ is the spectral density of intensity of a beam before entering the sample. [1] In tomographic measurements, the ratio I/I_0 is recorded. The main task of CT reconstruction in absorption regime is to find a map of μ throughout the sample.

Several physical mechanisms contribute to the linear absorption coefficient in the X-ray to the gamma region (tens of eV to MeV) (Fig. 1.4). These phenomena have a different probability of occurrence for different photon energies (Fig. 1.5).

- Scattering

For most of the energies used in CT (above approximately 50 keV), the scattering is the dominant process contributing to X-ray absorption.[1]

Compton scattering (Fig. 1.4) describes an inelastic scattering of free electrons. The incoming photon is deflected through a certain angle with respect to its original direction with lower energy (higher wavelength). Part of the photon energy is transferred to the electron, which is assumed to be initially at rest. It is, in general, the most dominant process of X-ray interaction with matter in energy range approximately from 100 keV to 10 MeV. [1]

Thompson scattering is a special case of Compton scattering for low energies (photon energies are much smaller than mass energy of the particle). The energy of the incident and the deflected photon is the same, and the scattering is elastic. [1]

¹ $\int_{\Phi} f dt$ means a curve integral of function f along a curve Φ . [1]

1. LITERATURE REVIEW

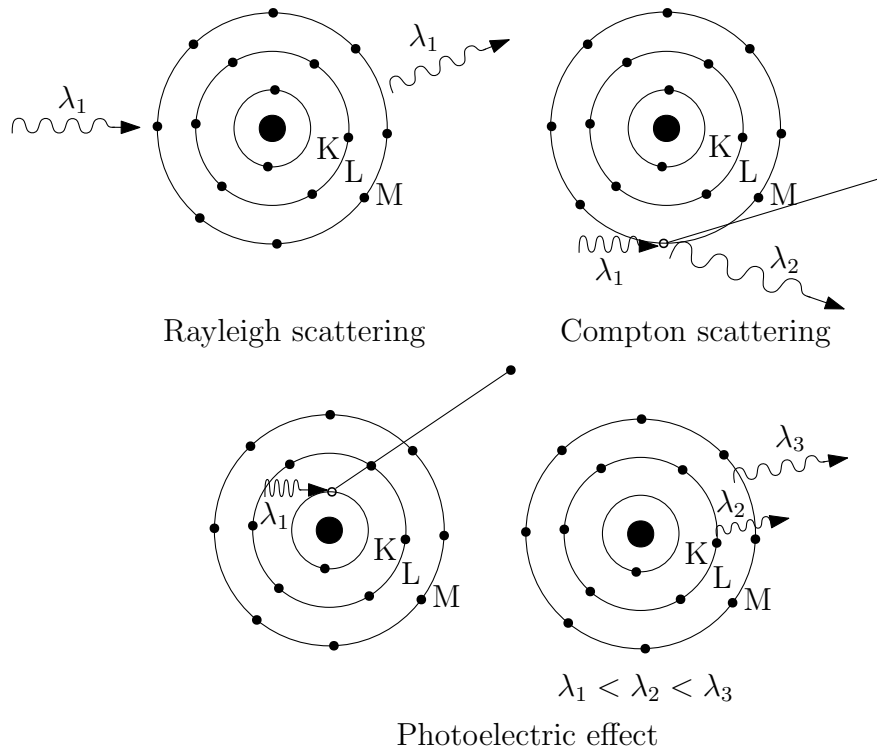


Figure 1.4: Interaction of electromagnetic radiation with matter in X-ray region. According to [1].

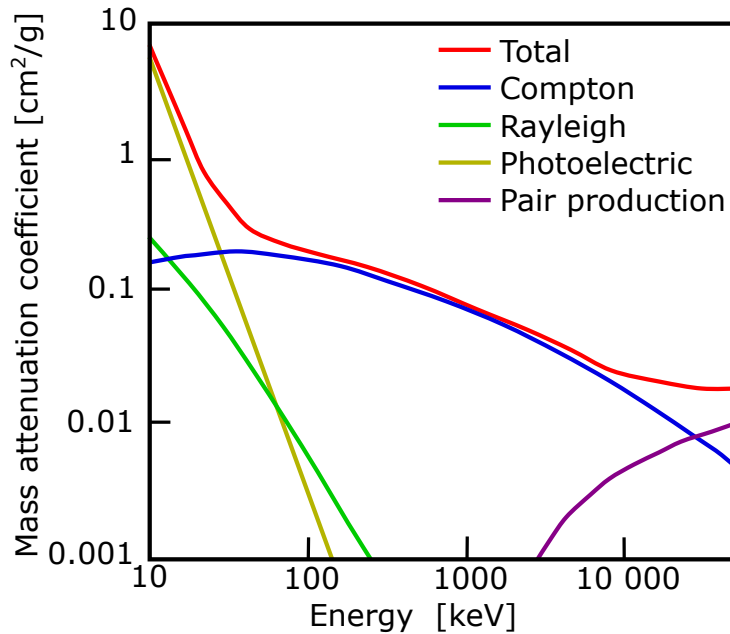


Figure 1.5: Contributions of individual phenomena to mass attenuation coefficient of soft tissue ($Z \approx 7$) for different energies. According to [4].

Rayleigh scattering (Fig. 1.4), in contrary, describes the scattering of the whole atom. The electric field of photons encountering the atom causes the whole atom to irradiate the photons with the same energy. No ionisation of an atom occurs, thus the process is elastic. The probability of Rayleigh scattering decreases with increasing energy. [1]

- Photoelectric effect (Fig. 1.4)

This effect dominates at lower X-ray energies (roughly below 50 kV). The atom absorbs the photon, and the electron from inner atomic shells is ejected. The energy of the photon has to be larger than the binding energy of the electron. The free space left after the released electron gets occupied by an electron from higher atomic shells, and at the same time, Auger electrons or X-rays with energy equal to the difference between the shells are emitted. These energies are typical for each element, and they form the characteristic peaks of emission spectra of a given element. [1]

- Positron-electron pair production

If a high-energetic photon enters an electric field of an atom, a positron-electron pair can be produced. The minimal photon energy required for this process is twice the energy of an electron at rest 0.511 MeV, which is 1.022 MeV. The rest of the energy is dissipated to the kinetic energy of the rest of the electrons in the atom. Electrons and positrons lose their kinetic energy through excitation and ionisation. When a positron loses all its kinetic energy, it annihilates with electron and two photons, each of energy 0.511 MeV and with opposite directions, are created. In the range of energies used in CT, this interaction does not occur. [1]

Atomic form factor

Phase contrast effects are related mainly to the Thompson elastic scattering at low energies. The energy of the photon remains invariant, but the direction, or the wave vector \vec{k} ($|\vec{k}| = k = 2\pi/\lambda$, k is a wave number and λ is a wavelength), can change: $|\vec{k}_{\text{in}}| = |\vec{k}_{\text{out}}|$, but $\vec{k}_{\text{in}} - \vec{k}_{\text{out}} = \vec{Q}$. \vec{Q} is called the scattering vector. The angle between the incident wave vector \vec{k}_{in} and the scattered wave vector \vec{k}_{out} is 2ϑ (Fig. 1.6). It follows from Fig. 1.6 that $Q = 2k \sin \vartheta = 4\pi/\lambda \sin \vartheta$.

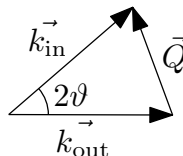


Figure 1.6: Elastic scattering of a photon on an electron.

This scattering is described by atomic form factor (sometimes atomic scattering factor) f as a function of angle, energy $\hbar\omega$ (ω is an angular frequency) and atom type. Scattering amplitude in direction ϑ from the entire electron cloud is expressed as $f(Q)$ or $f(\sin \vartheta/\lambda)$. It is a complex quantity:

$$f(Q, \hbar\omega) = f_1(Q, \hbar\omega) + i f_2(\hbar\omega),$$

which can be further developed as $f_1(Q, \hbar\omega) = f^0(Q) + f'(\hbar\omega)$.

The $f^0(Q)$ describes scattering on a free electron, i.e. an electron is not hindered by the fact that he is bound to atomic nuclei. It can be expressed as the sum of four Gaussians plus a constant: $f^0(Q) = f^0(\sin \vartheta/\lambda) = \sum_{i=1}^4 a_i \exp(-b_i \sin^2 \vartheta/\lambda^2) + c$. Values of every element a_i , b_i and c in this expression are tabulated. This approximation is valid for photon energies much larger than the binding energy.

1. LITERATURE REVIEW

The damping due to electron-nucleus binding is expressed by the dispersion correction term $f'(\hbar\omega)$ ($f' \leq 0$ and $f_1 \leq f^0$). This is most pronounced at resonance, where the photon energy equals the binding energy of the electron to the atom.

Another dispersion term $f_2(\hbar\omega)$ considers the absorption of X-rays. It increases abruptly at resonance. f_2 lags f_1 by 90 degrees, which is expressed as being imaginary part of f . [5, 6]

Index of refraction in X-ray region

The response of a material to passing X-rays can be described by a complex index of refraction n . It is related to the atomic form factor via [5, 6]

$$n = 1 - \frac{r_0}{2\pi} \lambda^2 \sum_i N_i f_i(0),$$

where $r_0 = 2.82 \cdot 10^{-5} \text{ \AA}$ is the classical radius of electron. The sum is over all elements i within the material of the number density N_i , multiplied by the real part of the atomic form factor in the forward direction. By expansion of the f term, this can be rewritten and further simplified as

$$n = 1 - \frac{r_0}{2\pi} \lambda^2 \sum_i N_i f_{1i}(0) - i \frac{r_0}{2\pi} \lambda^2 \sum_i N_i f_{2i}(0) \equiv 1 - \delta + i\beta.$$

The coefficient δ is known as a refractive index decrement. The sum $\sum_i N_i f_{1i}(0)$ is equated to effective electron number density ρ_e , the δ is then expressed as $\delta = \frac{\rho_e r_0 \lambda^2}{2\pi} = \frac{2\pi \rho_e r_0}{k^2}$.

δ determines the phase shift of a wave relative to the wave propagating in vacuum. At every scattering event, the phase of a wave going through the object is different from an unscattered wave. This difference gets bigger with every other event. The phase velocity of radiation in an object is higher than the velocity of propagation of radiation, which leads to the change of index of refraction. [1]

The coefficient β determines attenuation. It is related to the linear attenuation coefficient by relation [7]

$$\mu = \frac{4\pi}{\lambda} \beta,$$

Values of δ , resp. β of light materials for X-rays are typically from 10^{-5} to 10^{-6} , resp. from 10^{-8} to 10^{-9} . The ratio δ/β can be used as a figure of merit for phase effects compared to attenuation effects (Fig. 1.7). [7]

Transmission function

A wave passing through a sample is modulated in both phase and intensity. For simplicity, propagation of wave inside the sample is neglected, and the sample is projected only to a single plane x, y perpendicular to the direction of propagation z . The transmission function $T(x, y)$ gives the ratio of amplitudes of the incident and transmitted wave [1, 8]

$$T(x, y) = \exp(i\varphi(x, y) - \tilde{\mu}(x, y)/2). \quad (1.2)$$

The term $\tilde{\mu}$ denotes the integral in the argument of the exponential function in the Beer-Lambert law (Eq. 1.1): $\tilde{\mu} \equiv \int_{\Phi} \mu dt$. $\varphi(x, y)$ is the phase of the wave.

The transmission function corresponds to the projection of n distribution via

$$T(x, y) = A(x, y) \exp(i\varphi(x, y)),$$

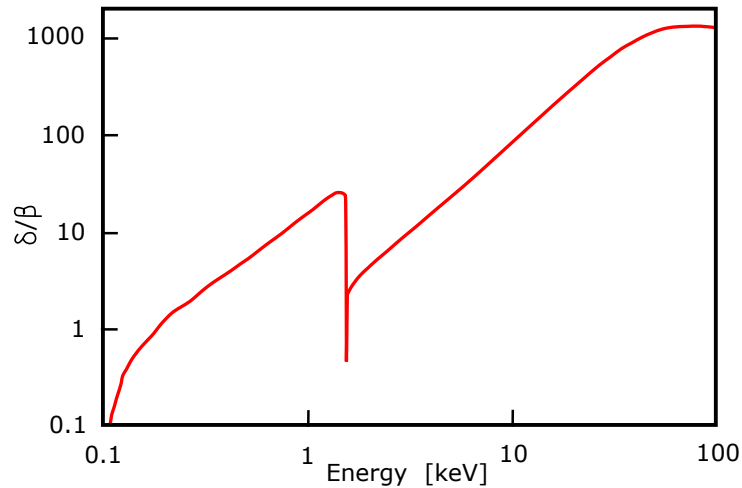


Figure 1.7: δ/β ratio as a function of energy for aluminium. According to [7].

where the amplitude is

$$A(x, y) = \exp(-B(x, y)), \quad B(x, y) = \frac{2\pi}{\lambda} \int_{-\infty}^{\infty} \beta(x, y, z) dz$$

and the phase modulation

$$\varphi(x, y) = \frac{2\pi}{\lambda} \int_{-\infty}^{\infty} [1 - \delta(x, y, z)] dz = \varphi_0 - \frac{2\pi}{\lambda} \int_{-\infty}^{\infty} \delta(x, y, z) dz,$$

where φ_0 is the phase modulation that would occur in the absence of the object. [1, 7]

For a homogenous material ($\delta = \text{konst.}$), the phase modulation is directly proportional to a thickness of the material $t(x, y)$:

$$\varphi(x, y) - \varphi_0 = -\frac{2\pi\delta}{\lambda} t(x, y). \quad (1.3)$$

1.1.3. Image reconstruction

The result of a CT scan of a sample $f(x, y)$ is a set of projections $p(\varrho, \theta)$. The goal of a reconstruction is to calculate a slice through the object from obtained projections. It is a large area of study. Here, only a basic reconstruction method called filtered back-projection for a parallel beam is described. The meaning of the variables is illustrated in Fig. 1.9. [1]

1. LITERATURE REVIEW

Radon transform

Every point of projection $p(\varrho, \theta)$ for a given angle θ is given by a line integral

$$p(\varrho, \theta) = \int_{\Phi_{\varrho, \theta}} f dt,$$

which is generated by summing up all contributions of the sample to the absorption along the line Φ implicitly given by the equation $x \cos \theta + y \sin \theta = \varrho$ with parameters θ, ϱ . With the use of δ -distribution², this can be rewritten as [1]

$$p(\varrho, \theta) = \int_{-\infty}^{\infty} \int_{-\infty}^{\infty} f(x, y) \delta(x \cos \theta + y \sin \theta - \varrho) dx dy, \quad (1.4)$$

which is the expression of the Radon transform of function $f(x, y)$. A sinogram is used for visualisation of the Radon transform (Fig. 1.8) [1, 9, 10].

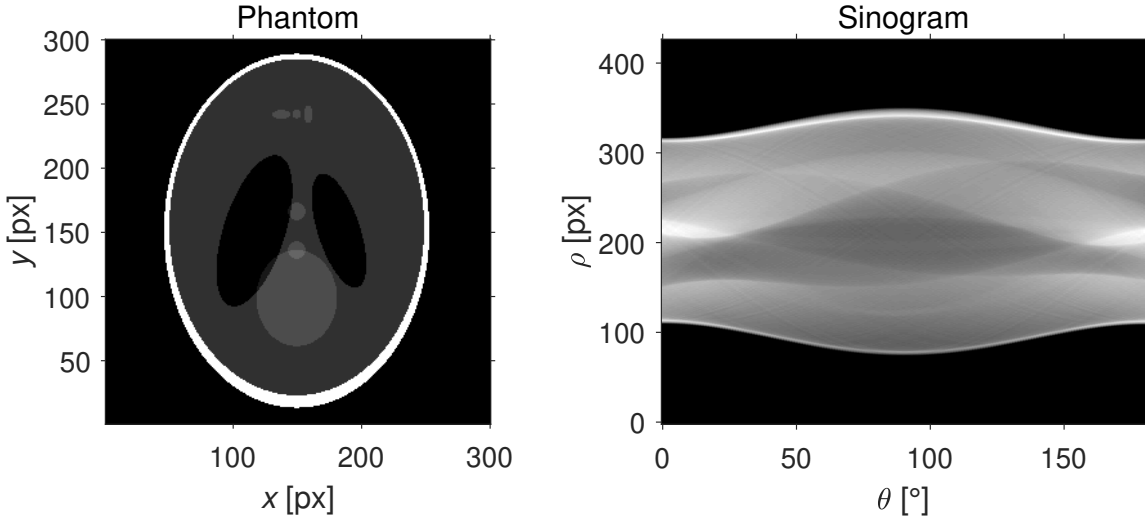


Figure 1.8: Left: a phantom generated in Matlab, right: a sinogram of the phantom. [1]

Fourier slice theorem

The 1D Fourier transform³ of a parallel projection $p(\varrho, \theta)$ of an object $f(x, y)$ obtained at angle θ equals a line in a 2D Fourier transform of object $F(u, v)$ taken at the same angle (Fig. 1.9). [1, 3].

Proof. Let $P(\Omega, \theta)$ be the 1D Fourier transform of the projection $p(\varrho, \theta)$

$$P(\Omega, \theta) = \mathcal{F} \{p(\varrho, \theta)\} (\Omega, \theta) = \int_{-\infty}^{\infty} p(\varrho, \theta) \exp(-i2\pi\Omega\varrho) d\varrho.$$

² δ -distribution is a generalized function which equals to 0 everywhere except at the origin, $\delta(x) = 0$ if $x \neq 0$. It is also constrained to satisfy $\int_{-\infty}^{\infty} \delta(x) dx = 1$.

³ N -dimensional Fourier transform: $\mathcal{F} \{f(\vec{x})\}(\vec{\omega}) = \int_{\mathbb{R}^N} f(\vec{x}) \exp(-i2\pi\vec{x} \cdot \vec{\omega}) d^N \vec{x}$.

Inverse N -dimensional Fourier transform: $\mathcal{F}^{-1} \{F(\vec{\omega})\}(\vec{x}) = \int_{\mathbb{R}^N} F(\vec{\omega}) \exp(i2\pi\vec{x} \cdot \vec{\omega}) d^N \vec{\omega}$.

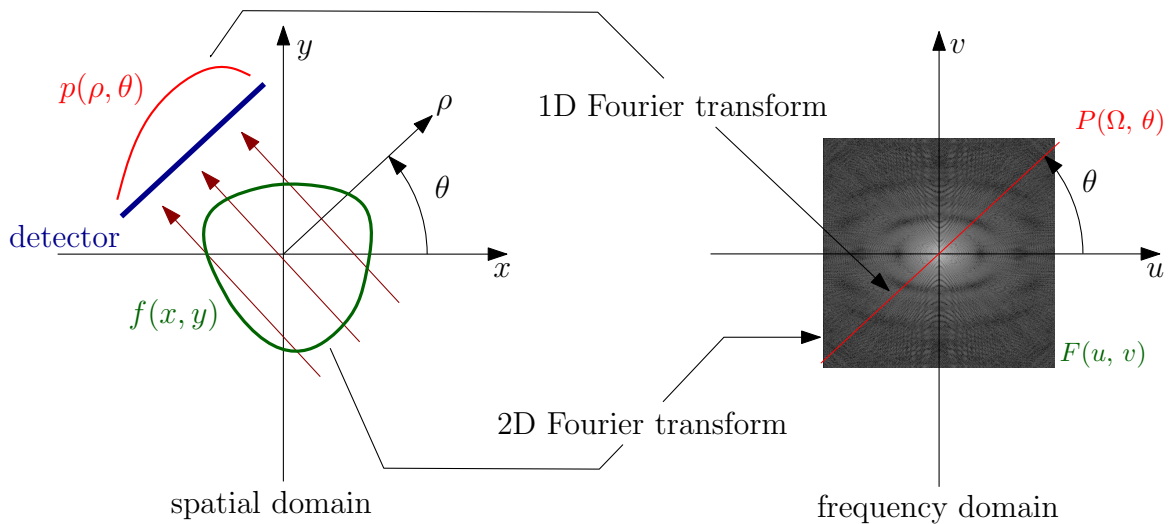


Figure 1.9: Illustration of the Fourier slice theorem. According to [1, 10].

This relation can be further transformed. The projection $p(\varrho, \theta)$ is the Radon transform of the object according to Eq. 1.4. Next, the order of integration is changed according to the Fubini's theorem (verification of assumption is left out). With the use of the definition of δ -distribution, the expression arrives to

$$\begin{aligned}
 & \int_{-\infty}^{\infty} p(\varrho, \theta) \exp(-i2\pi\Omega\varrho) \, d\varrho = \\
 & = \int_{-\infty}^{\infty} \left[\int_{-\infty}^{\infty} \int_{-\infty}^{\infty} f(x, y) \delta(x \cos \theta + y \sin \theta - \varrho) \, dx \, dy \right] \exp(-i2\pi\Omega\varrho) \, d\varrho = \\
 & = \int_{-\infty}^{\infty} \int_{-\infty}^{\infty} f(x, y) \left[\int_{-\infty}^{\infty} \delta(x \cos \theta + y \sin \theta - \varrho) \exp(-i2\pi\Omega\varrho) \, d\varrho \right] \, dx \, dy = \\
 & = \int_{-\infty}^{\infty} \int_{-\infty}^{\infty} f(x, y) \exp(-i2\pi\Omega(x \cos \theta + y \sin \theta)) \, dx \, dy = \\
 & = \mathcal{F} \{f(x, y)\} (\Omega \cos \theta, \Omega \sin \theta) = P(\Omega, \theta).
 \end{aligned}$$

The penultimate row represents the slice through 2D Fourier transform of the object labeled $P(\Omega, \theta)$. This proves the Fourier projection theorem. [1].

In theory, it is possible to reconstruct a slice through the object from projections in the following way:

1. calculate the 1D Fourier transform of all projections,
2. use these transformed projections to create 2D Fourier image of the object,
3. calculate the image of the object by inverse Fourier transform.

However, the inverse Fourier transform is numerically unstable, and in practice, the reconstruction is done in another way. [1].

1. LITERATURE REVIEW

Filtered backprojection

The goal is to obtain the image of the object

$$f(x, y) = \mathcal{F}^{-1} \{F(u, v)\} (x, y) = \int_{-\infty}^{\infty} \int_{-\infty}^{\infty} F(u, v) \exp(i2\pi(ux + vy)) \, du \, dv.$$

This can be rewritten in polar coordinates as

$$\begin{aligned} f(x, y) &= \int_0^{\pi} \int_{-\infty}^{\infty} |\Omega| P(\Omega, \theta) \exp(i2\pi\Omega(x \cos \theta + y \sin \theta)) \, d\Omega \, d\theta = \\ &= \int_0^{\pi} \int_{-\infty}^{\infty} |\Omega| \left(\int_{-\infty}^{\infty} p(\varrho, \theta) \exp(-i2\pi\Omega\varrho) \, d\varrho \right) \exp(i2\pi\Omega(x \cos \theta + y \sin \theta)) \, d\Omega \, d\theta. \end{aligned} \quad (1.5)$$

The expression 1.5 is the analytical formulation of the inverse Radon transform of the object. The expression $|\Omega| \int_{-\infty}^{\infty} p(\varrho, \theta) \exp(-i2\pi\Omega\varrho) \, d\varrho$ represents the projection filtered in the frequency domain by the filter $|\Omega|$. The real data contain noise, which is even highlighted by the filter $|\Omega|$ itself ($|\Omega|$ highlights high frequencies). For numerical reasons, the filter $|\Omega|$ is multiplied by yet another function that is replaced at some point by a zero function. The list of commonly used filters $\zeta(\Omega)$ is in Tab. 1.1 [3, 11]. [1]

The middle integral is the same for all x, y on the line $\Phi_{\varrho, \theta}$. It is thus possible to imagine it by calculating its value at one point and then assigning it to each point of the relevant line (backprojection). The whole process is called the filtered backprojection. It is summarised in steps in the diagram in Fig. 1.10. [1]

The filter can also be applied in a spatial domain using convolution⁴ of the inverse 1D Fourier transform of filter $\zeta(\Omega)$ with the projection p [1, 3, 10]:

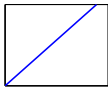
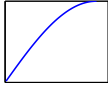
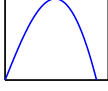
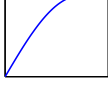
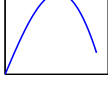
$$\mathcal{F}^{-1}\{p(\varrho, \theta)\}(\Omega, \theta) = p(\varrho, \theta) * \mathcal{F}^{-1}\{\zeta(\Omega)\}(\varrho).$$

This relationship follows from the Eq. 1.5 using the following Fourier transform property: [1].

$$\mathcal{F}\{f_1(x) * f_2(x)\} = \mathcal{F}\{f_1(x)\} \cdot \mathcal{F}\{f_2(x)\}.$$

⁴Convolution of functions $f_1(x)$ and $f_2(x)$: $(f_1 * f_2)(x) = \int_{\mathbb{R}} f_1(y) f_2(x - y) \, dy$.

Table 1.1: The list of commonly used filters $\zeta(\Omega)$ in filtered backprojection. [1]

Filter name	$\zeta(\Omega)$	Shape
Ram-Lak (ramp)	$ \Omega $	
Shepp-Logan	$ \Omega \operatorname{sinc} \Omega$	
Cosine	$ \Omega \cos \Omega$	
Hann	$ \Omega ^{\frac{1}{2}}(1 + \cos \Omega)$	
Hamming	$ \Omega [\alpha + (1 - \alpha) \cos \Omega],$ $\alpha \dots \text{konst.}$	

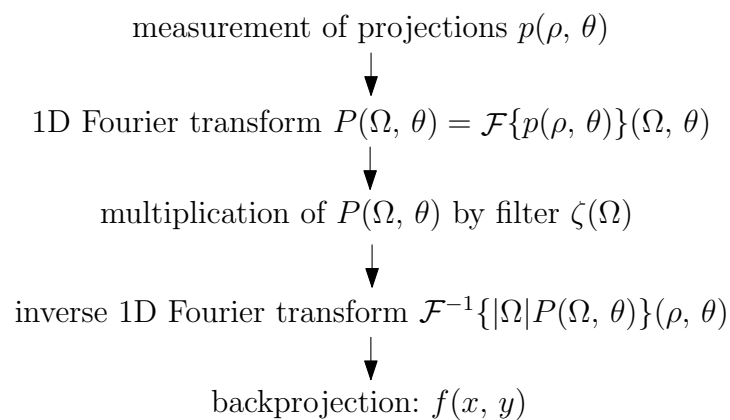


Figure 1.10: The diagram of filtered backprojection. [1]

1. LITERATURE REVIEW

1.1.4. Databases of materials properties in X-ray region

The following list contains links to Internet databases which provide information about properties of materials, elements and tissues in X-ray region, up-to-date to the thesis publication. [1] The italics items in the list are links to the cited websites.

- *X-ray interactions with matter* – databases of material and atom properties [12]
 - *Index of refraction*
 - *X-ray data booklet* [13]
- *X-ray form factor, attenuation, and scattering tables* – detailed tabulation of atomic form factors, photoelectric absorption and scattering cross-section, and mass attenuation coefficients for $Z = 1-92$ from $E = 1-10$ eV to $E = 0.4-1.0$ MeV (NIST Standard Reference Database 66) [14]
- *X-ray mass attenuation coefficients* – tables of X-ray mass attenuation coefficients and mass energy absorption coefficients from 1 keV to 20 MeV for elements $Z = 1$ to 92 and 48 additional substances of dosimetric interest [15]
- *X-ray absorption edges* – tabulations of the characteristic X-ray absorption edge energies and atomic form factors as a function of incident X-ray energy [16]
- *Periodic table* – edge energies, edge jumps and fluorescent yields of elements [17]
- *XOP (X-ray oriented programs)* – a widget-based driver program that is used as a common front-end interface for computer codes of interest to the synchrotron radiation community. [18]

1.2. Phase contrast imaging

The absorption CT is based on X-ray attenuation. The greyscale of images corresponds to the linear attenuation coefficient μ of an imaged sample. For the same sample thickness, a material with a higher μ is more difficult to be penetrated by X-rays than material with a lower μ , which is less X-ray absorbing. In X-ray projection, those two materials have different intensities, resulting in absorption contrast. However, samples from light materials, such as polymers, polymer composites, biomaterials, soft tissues, etc., have low X-ray absorption and thus poor absorption contrast. In these cases, either some staining methods for an increase of absorption or phase contrast imaging methods have to be used.

Staining of samples is a very common way to enhance the absorption contrast of soft materials in CT. For example, phosphotungstic acid, iodine solution, osmium tetroxide or phosphomolybdic acid are commonly used stains [19–21]. Staining procedures usually include several steps (fixation, staining, drying) and last from several hours to several weeks [22–25].

Phase contrast methods, on the other hand, do not require any sample preparation protocol. Instead, they exploit the phase change of X-rays going through an object. [26] Each material interacts with X-rays differently because of the different electron configuration of atom's shells, which results in phase contrast. These effects are much stronger for light materials than for heavy ones.

The phase of an X-ray beam transmitted through a material is shifted due to its interaction with the electron shells of atoms [7]. There are several ways of recording this phase shift and obtaining phase contrast. X-ray interferometer technique is based on the interference of a reference beam with a beam transmitted through the sample [27, 28]. Analyser-based methods involve the reflection on Bragg crystals, which filter different X-rays based on their angle [29, 30]. Talbot-Lau grating interferometry uses the self-imaging property of gratings to make the phase changes visible [31–36]. Phase contrast can also be observed with the use of X-ray optics in X-ray microscopes [37–39].

X-rays transmitted through the sample are also slightly deviated from the original direction as they diffract on inner structures of material. When X-ray deviations associated with different structure sizes propagate through a certain distance, their wavefronts interfere and form an inline phase contrast [40]. If the tomographic setup is modified just by enlarging the distance between the sample and the detector, this phase contrast becomes visible in the form of edge enhancement [41]. This approach is called the propagation-based imaging (PBI), and it is the main CT method utilised in this work.

PCI is utilised in various fields in biology for imaging of small animals and soft tissues [42–44] and in material science as well, for example in imaging of material discontinuities in polymer composites composed of light materials with similar attenuation coefficient [45–47]. Edge enhancement via PBI with a laboratory, polychromatic X-ray sources has been reported on various examples of fibres in the polymer matrix [48–50], mouse lungs [51], liver tissue [52] or cochlea [53] or leaves and insects [54]. Many works deal with optimisation of PBI in laboratory conditions regarding the setting of hardware setup or post-processing of data [55–60] and there is still much room for improvement.

1.2.1. Propagation-based imaging

“X-ray wavefronts passing through the sample are distorted on sample’s structures proportionally to the phase shift imposed by the sample. After propagating through a given distance, they interfere to form Fresnel diffraction fringes [49, 61].” [37] In the image, this is visible in the form of edge enhancement.

Imaging regime

The intensity of the phase contrast signal depends on a so-called effective propagation distance $z_{\text{eff}} \equiv \text{SSD} \times \text{SDD} / (\text{SSD} + \text{SDD})$, where SSD is the source–sample distance and SDD is the sample–detector distance. z_{eff} defines the imaging regime (Fig. 1.11). In paraxial approximation, the imaging regime is characterised by Fresnel number N_{F} [7]

$$N_{\text{F}} = \frac{a^2}{\lambda z_{\text{eff}}}, \quad (1.6)$$

where a is the size of a feature of interest. “The edge enhancement for the given feature size is pronounced when $N_{\text{F}} \approx 1$ [51, 62], and from the obtained images, it is possible to directly extract the morphological information about the sample. For $N_{\text{F}} \ll 1$, not only edge enhancement but also multiple fringes appear, and the real structure is no longer recognizable. This is a so-called holographic, or for very low N_{F} far-field, regime.

To have the structures of the sample directly recognizable, the holographic regime, e.g. large sample–detector distances, should be avoided. In such case, in order to stay

1. LITERATURE REVIEW

in the near-field regime, $N_F > 1$ should be fulfilled for every structure visible in the image. At the same time, the Fresnel number should not be too large ($N_F \gg 1$) since for small SDDs, the propagation effects are negligible and the results are only absorption images.” [37]

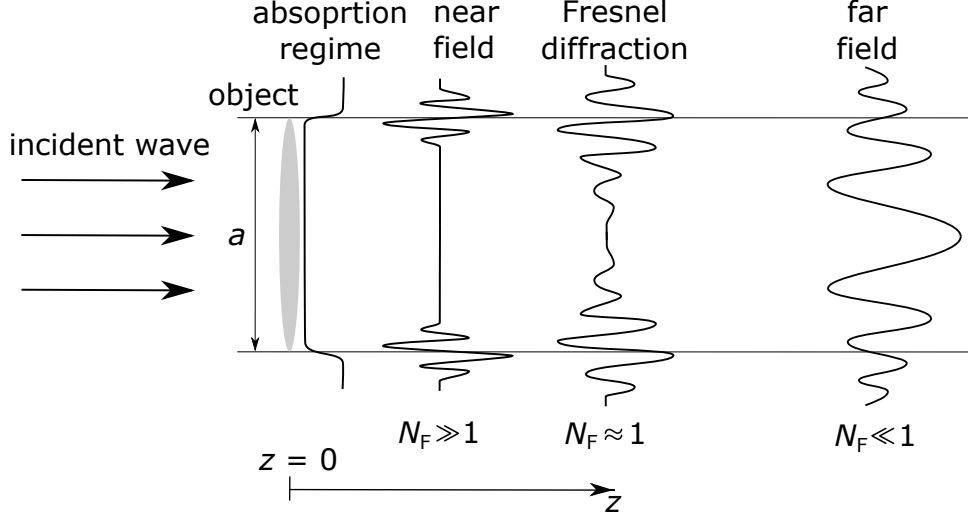


Figure 1.11: Diffraction of a plane wave on an object of size a . [1]

Contrast transfer function

Under the assumption that the specimen is sufficiently thin and/or weakly interacting (“weak object approximation”), the transmission function (Eq. 1.2) may be written as [8]

$$T(x, y) = \exp(i\varphi(x, y) - \tilde{\mu}(x, y)/2) \approx 1 + i\varphi(x, y) - \tilde{\mu}(x, y)/2.$$

Then, the wave intensity in the frequency domain $I_F(u, v) \equiv \mathcal{F}\{I(x, y)\}(u, v)$ becomes [8]

$$I_F(u, v) = \delta(u, v) + 2\mathcal{F}\{\varphi(x, y)\}(u, v) \sin \chi - 2\mathcal{F}\{\tilde{\mu}(x, y)/2\}(u, v) \cos \chi,$$

where $\chi = \pi\lambda z(u^2 + v^2)$. Here, δ denotes the Dirac δ distribution, and z is a propagation distance for a parallel beam and effective propagation distance z_{eff} for a cone-beam [63]. “The functions $\sin \chi$ and $\cos \chi$ are called the phase and amplitude contrast transfer functions (CTFs) and may be thought of as linear filters which determine the transfer of spatial frequencies from the phase and amplitude components of the object transmission function to the image (Fresnel diffraction pattern). These (1D) phase and amplitude CTFs are shown in Fig. 1.12 as a function of the reduced variable $\sqrt{\lambda z}u$. From this, one can determine, for instance, the imaging distance for which the phase CTF of a given spatial frequency u achieves a first maximum” [8, 64]:

$$z_u = \frac{1}{2\lambda u^2}.$$

The optimal condition for absorption contrast, $\cos \chi = 1$, is satisfied at $z = 0$, e.g. just after the sample with no phase contrast. This holds for all wavelengths and spatial frequencies. The absorption and phase contrast are largely complementary as the imaging

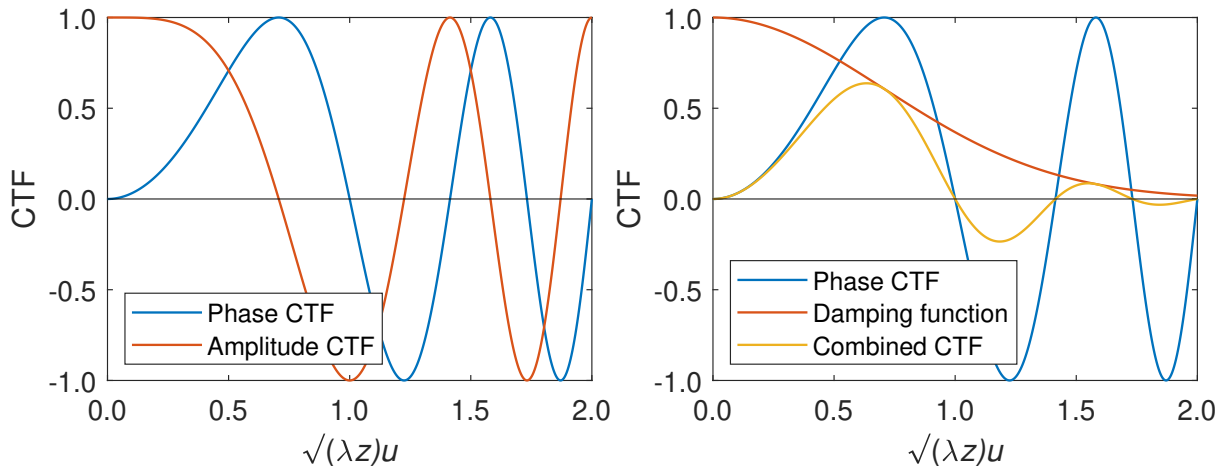


Figure 1.12: Left: contrast transfer function (CTF), right: damping of phase CTF due to finite source size. According to [8].

conditions are varied. In particular, in the near-field regime, absorption contrast will best show relatively large, slowly varying features, whereas phase contrast will best show small or rapidly varying features, such as sharp edges. [8]

In practice, it is difficult to choose one optimal distance, since real samples often have many spatial frequencies. Fresnel diffraction pattern enhances different structures of an object based on imaging distance. For PBI, the sample–detector distance has to be chosen such as the sample is in near field regime, which is achieved for $\chi \lesssim \pi$. [1, 8]

Degree of X-ray coherence

The previous equations are strictly valid only for the fully coherent beam. This situation does not occur in practice. The beam has a certain spatial distribution of intensity instead of a point-like source and also a wavelength spread. These two aspects are referred to as spatial and temporal coherence, respectively. [8]

Spatial coherence is influenced by transverse source intensity labeled $s(x, y)$ contributing to point spread function. In the Fourier optics formulation, this can be expressed as damping of the CTF by the Fourier transform of suitably normalised $s(x, y)$ (Fig. 1.12). The spectral distribution contributing to temporal coherence can be modelled by choosing a plausible distribution for the source (i.e. Gaussian). This distribution also contributes to damping of CTF. [8]

Under the simplifying assumption of evenly distributed intensity of spot of size s , the lateral coherence length is defined as $L_{\text{lat}} = \lambda \times \text{SSD}/s$. “Phase contrast is formed between interfering waves from positions separated by a shearing length $L_{\text{shear}} = \lambda \times \text{SDD}/(Ma)$, where $M = (\text{SSD} + \text{SDD})/\text{SSD}$ stands for magnification. The wave has to have sufficiently high degree of coherence over this length to make phase contrast visible. Visibility of phase contrast is therefore characterized by ratio $L_{\text{shear}}/L_{\text{lat}}$. [40, 65]

The X-ray beam is almost fully coherent if the ratio $L_{\text{shear}}/L_{\text{lat}} \ll 1$. In practice, the phase contrast fringes occur also when the X-rays are partially coherent and their visibility is improved with an increasing degree of coherence. The criterion for partial coherence can be therefore stated as” [37]

$$\frac{L_{\text{shear}}}{L_{\text{lat}}} = \frac{s \times \text{SDD}}{a(\text{SSD} + \text{SDD})} < 1. \quad (1.7)$$

1. LITERATURE REVIEW

Geometrical unsharpness due to focal spot size

“Lastly, a restriction following from a finite focal spot of X-ray tube has to be mentioned. The resolution is restricted by the focal spot size because at a given sample–detector distance, the X-rays from the whole area of the focal spot start to form an unsharpened spot of size U on the detector larger than pixel size p (Fig. 1.13). To avoid this unsharpness, the condition $U < p$ must be fulfilled. From the geometry of the system, this means [66]” [37]

$$\frac{\text{SDD}}{\text{SSD}} \times s < p. \quad (1.8)$$

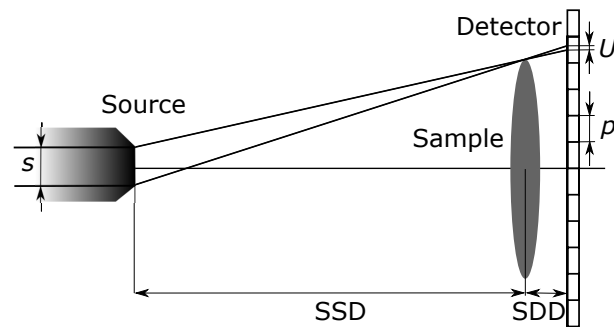


Figure 1.13: Formation of geometrical unsharpness U at the detector with linear pixel size p due to finite focal spot size s . SSD stands for the source–sample distance, SDD stands for the sample–detector distance. [37]

1.2.2. Phase retrieval

The problem of retrieving information about the phase change is solved by phase retrieval algorithms. There are various approaches to this task. They can be either iterative (numerical) [67, 68] or analytical (derived from physics principles). These non-iterative methods differ in the amount of raw data needed (some of the methods require images taken at multiple propagation distances), restrictions on sample composition, properties of the X-ray beam, and quality of the reconstruction (accuracy of the reconstructed phase values and spatial resolution of the results) [69].

The following text is focused on the most widely used analytical algorithms for single-distance data, which are based on the transport of intensity equation (Eq. 1.9) [70–72]. Several examples presented here are derived for monochromatic radiation, but they would still be appropriate if average X-ray energy or the main characteristic peak is considered [65, 73]. Phase retrieval approaches directly taking into account the wavelength spread of laboratory-based X-ray source are shown for instance in [73].

From an image processing point of view, the application of phase retrieval algorithm is necessary to get data with less noise and multi-modal histogram, which are easier to segment [37, 41]. Examples are shown in detail in the chapters 4 and 5.

Transport of intensity equation (TIE)

The TIE describes the relation of intensity $I_z(x, y)$ and phase $\varphi_z(x, y)$ of a paraxial monochromatic wave propagating along the optical axis z^5 [62]

$$\nabla_{\perp} [I_z(x, y) \nabla_{\perp} \varphi_z(x, y)] = -\frac{2\pi}{\lambda} \frac{\partial I_z(x, y)}{\partial z}. \quad (1.9)$$

In the following, $I_z(x, y)$ represents the intensity corrected by the intensity distribution of the incident radiation [74].

Paganin algorithm (PA)

For the derivation of PA, the object is assumed to be composed of a single material with a constant index of refraction. The absorption then follows the Beer-Lambert law (Eq. 1.1). The phase $\varphi(x, y)$ of a sufficiently thin object is proportional to the projected thickness $t(x, y)$ (Eq. 1.3). Inserting these expressions into the TIE (Eq. 1.9) and rearranging the result using the identity $\exp(f(x)) \nabla_{\perp} f(x) = \nabla_{\perp} \exp(f(x))$ yields [74, 75]

$$\left(-\frac{\delta}{2k\beta} z_1 \nabla_{\perp}^2 + 1 \right) \exp(-2k\beta t(x, y)) = I_{z=z_1} t(x, y).$$

By inverting the Laplacian in Fourier space, leading to filtering with the function $-\frac{1}{(u^2+v^2)}$, the phase of the wave in the object's exit plane $z = 0$ can be retrieved via [74, 75]

$$\varphi(x, y) = \frac{\delta}{2\beta} \ln \left(\mathcal{F}^{-1} \left\{ \frac{\mathcal{F} \{ I_{z=z_1}(x, y) \}}{\frac{\delta}{2k\beta} z_1 (u^2 + v^2) + 1} \right\} \right). \quad (1.10)$$

⁵ $\nabla_{\perp} = \left(\frac{\partial}{\partial x}, \frac{\partial}{\partial y} \right)$

1. LITERATURE REVIEW

Modified Bronnikov Algorithm (MBA)

For the small propagation distances z_1 , the partial derivative in the TIE (Eq. 1.9) can be approximated as $\frac{\partial I_z(x, y)}{\partial z} \approx \frac{I_{z=z_1}(x, y) - I_{z=z_0}(x, y)}{z_1}$, leading to the following expression for the intensity distribution [74]

$$I_{z=z_1}(x, y) = I_{z=0}(x, y) - \frac{\lambda z_1}{2\pi} \nabla_{\perp} [I_{z=0}(x, y) \nabla_{\perp} \varphi(x, y)].$$

Under the assumption of a weakly absorbing object $\nabla_{\perp} I_{z=0}(x, y) \approx 0$, this leads to [74]

$$I_{z=z_1}(x, y) = I_{z=0}(x, y) \left[1 - \frac{\lambda z_1}{2\pi} \nabla_{\perp}^2 \varphi(x, y) \right]. \quad (1.11)$$

Analysing this result, “the weak intensity distribution imparted on the wave by the object does not undergo diffraction within the given assumptions (weak absorption, small propagation distance z_1), while the second derivative of the phase creates intensity variations increasing with propagation distance. In this so-called direct contrast regime, the phase contrast is hence visible in form of an edge-enhancement, as given by the Laplacian of the object’s projected phase function.” [74].

For a pure phase object, Eq. 1.11 can be further simplified to [74]

$$I_{z=z_1}(x, y) = 1 - \frac{\lambda z_1}{2\pi} \nabla_{\perp}^2 \varphi(x, y). \quad (1.12)$$

As in the case of PA, by inverting the Laplacian in Fourier space, the phase of the wave can be retrieved. In order to avoid singularity at $u^2 + v^2 = 0$, a regularization parameter α is added to the denominator, which leads to expression [74, 76]

$$\varphi(x, y) = \frac{2\pi}{\lambda z_1} \mathcal{F}^{-1} \left\{ \frac{\mathcal{F} \{ I_{z=z_1}(x, y) - 1 \}}{(u^2 + v^2) + \alpha} \right\}. \quad (1.13)$$

“The regularization parameter α also accounts for the object’s residual absorption which amplifies low spatial frequencies in the image. Hence, applying an unregularized filter would inevitably corrupt these Fourier components and yield strong artifacts and blurring. Therefore, α must be chosen sufficiently high, depending on the (residual) absorption of the object. At the same time this compromises the correct filtering for the phase and may result in incomplete inversion of the edge-enhancement.” [74]

Bronnikov Aided Correction (BAC)

To avoid problems mentioned with the MBA algorithm, a further reconstruction step can be applied to objects with non-negligible absorption. The phase φ_{MBA} reconstructed via the MBA (Eq. 1.13) can be used for correction of intensity function as [77]

$$I_{z=0}(x, y) = \frac{I_{z=z_1}(x, y)}{1 - \gamma \nabla_{\perp}^2 \varphi_{\text{MBA}}(x, y)}. \quad (1.14)$$

“The coefficient $\frac{\lambda z_1}{2\pi}$ was replaced by an α -dependent regularization parameter γ to avoid residual edge-enhancement (γ too small) or an inversion of the edges (γ too large).” [74]. This should result in sharp image of intensity directly behind the object.

1.3. Technology

X-ray computed tomography devices offer various possibilities in many fields. They are commonly divided into several categories based on sample size and achievable resolution, as it is suggested in [78]. In general, for thicker and denser samples, higher X-ray power is needed, and the highest achievable resolution gets lower (Fig. 1.14). In this section, all categories are briefly introduced and commented. In the following chapters, mostly the general shortcut CT is used to avoid unnecessary confusion about terminology.

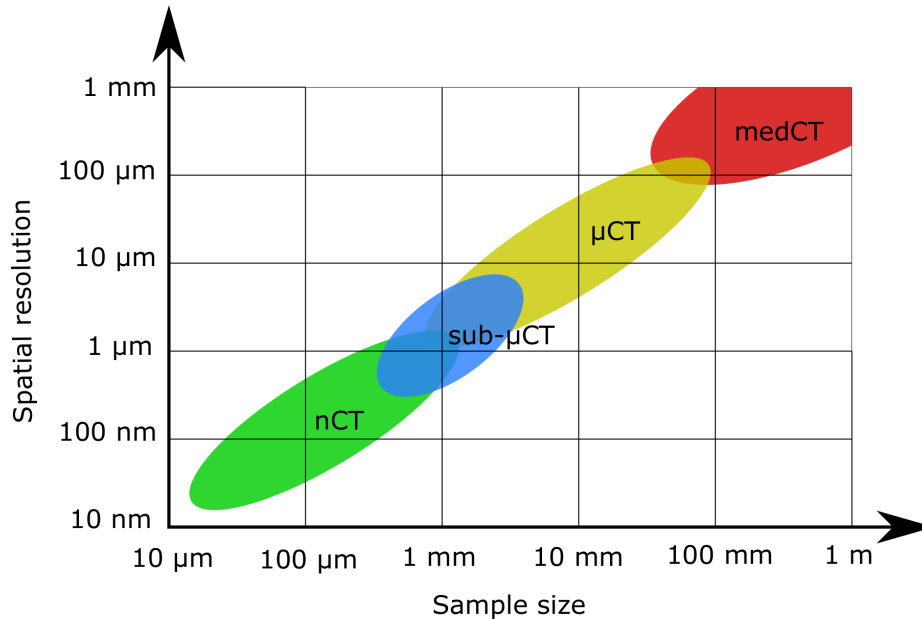


Figure 1.14: Division of CT devices according to the typical spatial resolutions and object sizes: medical X-ray computed tomography (medCT), X-ray computed microtomography (CT), X-ray computed nanotomography (nCT). Sometimes, also X-ray computed sub-micron tomography (sub- μ CT) is used for measurements at the boundary between nCT and μ CT. Inspired by [78].

1.3.1. Medical CT

Originally, applications and development of CT technology were made in clinical research. The first CT devices were constructed in the 1960s, about 70 years after the discovery of X-rays by William Roentgen in 1895 and nearly 50 years after Radon suggested the mathematical principle of the technique by publishing the Radon transform in 1917 [3, 79]. In 1979, Allan M. Cormack and Godfrey N. Hounsfield were awarded a Nobel prize in Physiology or Medicine for the development of computer-assisted tomography [80].

Nowadays, medical CT (medCT) scanners are in every modern hospital and play an essential role in a patient examination. Manufacturers of medCT must take into account the difficulties with scanning of a living patient, mainly reducing the X-ray dosage and decreasing of blurring caused by involuntary patient movement (breathing) [79, 81]. Because of these constraints, medCT scanners are generally constructed as having a patient lying on a table with an X-ray source and detector rotating at high speed around him. The only movement of a patient is the translation along the axis of the scanner.

1. LITERATURE REVIEW

Combining all those factors limiting the accuracy and precision, the typical spatial resolution is around several mm, which is sufficient for purposes of medical help, but too low for most of the applied research in any other field.

1.3.2. MicroCT, μ CT

Later, CT had spread into other fields, to industry for material analysis, metrology and quality control [79, 82, 83], and to biology and material science. In contrary to medicine, industrial X-ray computed microtomography (microCT, CT) scanners are not so concerned with X-ray dosage to the sample, therefore they are capable of using high-intensity X-ray sources and adjusting the geometry to achieve higher resolution, accuracy and precision than medCT (in this category up to $1\ \mu\text{m}$). This includes reversed geometry system: X-ray source and detector are stable during the measurement, and the sample is rotating to get projections from different angles.

Many information can be derived from CT data: measurement of dimensions, surfaces, volumes, detection and analysis of cracks, voids, inclusions, fibres, 3D visualisation of inner structure, comparison to CAD models, export of surface for 3D print etc. A lot of scientific works from various fields take advantage of some of CT features: developmental biology [84], civil engineering [85], geology [86], planetary materials [87], archaeology [88], food science [89] and others.

1.3.3. Sub- μ CT, nCT

The X-ray computed sub-micron tomography (sub- μ CT) or X-ray computed nanotomography (nCT) term is used for devices that reach spatial resolution below $1\ \mu\text{m}$ [37, 78, 85, 90]. In some works, only the term sub-micron tomography is used [91–93]. Authors may want to avoid confusion with nCT devices that reach a spatial resolution in tens of nm, but general characteristics as stated about nCT devices apply here as well. Also, authors who work with methods of several nanometers scale (as FIB and EDS in [94]) prefer to reserve the prefix nano for methods capable of nanometer resolution. In both categories, the CT devices often have highly precise mechanical parts, advanced detectors and may employ additional units and X-ray optics. This makes them different from mostly large, robust μ CT devices.

nCT and sub- μ CT laboratory devices without additional X-ray optics use two ways to reach this resolution. The one type employs geometrical magnification by the cone-beam shape of X-rays: the sample is placed close to the X-ray tube and projected to the large-area detector placed in the certain distance (Fig. 1.15a) [95]. The small voxel size is restricted by a small size of the focal spot (below $1\ \mu\text{m}$). Large area detectors similar as in μ CT can be used (e.g. GE nanotom [96]).

In another approach, the sample is not placed directly in front of the X-ray tube, but the source–sample distance is fixed at a relatively large distance compared to the sample size (a so-called inverse geometry [55, 97, 98]. The detector is placed close to the sample. The beam at the sample stage is considered semi-parallel because only a small part of the cone-beam at the sample position is used (Fig. 1.15b). The detector consists of a scintillator, which is followed by an optical system providing magnification of the image. The small voxel size is achieved by small pixels of CCD or sCMOS detectors, thus a larger focal spot size is acceptable (e.g. RIGAKU nano3DX [99]). It is the case of rotating anodes, where the electrons are distributed not into one spot as in the reflection

or transmission sources, but to a ring along the anode. This results in relatively large focal spot sizes in a range of 50–200 μm , but it also creates a beam with a large flux, which makes the exposure times and thus the whole measurements shorter. Moreover, this kind of system is less prone to focal spot drift and sample movement artefacts than the previously described one. [37] The other laboratory CT devices in this category employ some kinds of X-ray optics, which enables users to use phase contrast imaging as well: zonal plates and phase ring (e.g. Zeiss Xradia [100]) or gratings (e.g. Bruker Skyscan [101]).

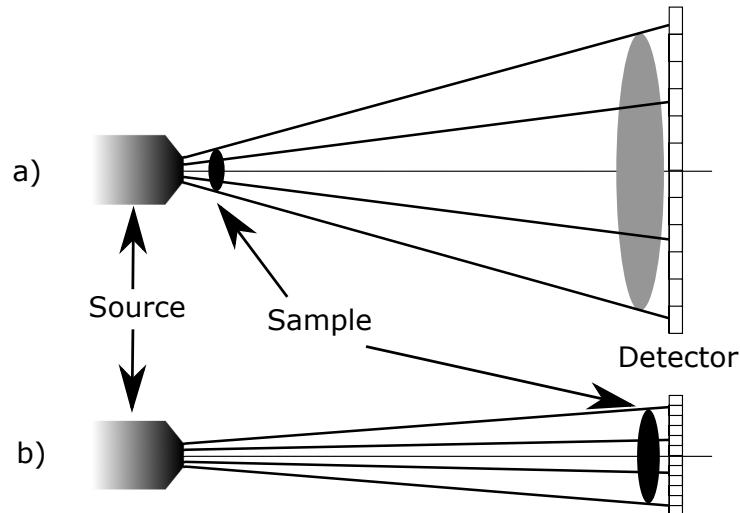


Figure 1.15: Different approaches in nCT systems: a) geometrical magnification is reached by use of cone-beam X-ray, b) long SSD is used to achieve semi-parallel X-ray beam at sample stage, and the image is magnified by the optical system after scintillator. [37]

One of the modern trends in nCT is the use of liquid metal jet X-ray source introduced by Excillum company [102]. Here, a solid metal anode is replaced by liquid metal. This type can bear much higher electron-beam power because it is not focused only on one spot or ring, but the electrons hit the flowing jet of metal. The resulting X-ray beam has a very high brightness while maintaining small (in micrometres), stable, tunable focal spot size. This property is useful for propagation-based phase contrast imaging (Sec. 1.2.1) [103–105].

1. LITERATURE REVIEW

2. Aims of thesis

The general aim of this thesis is to study, explore and bring new insights into the field of imaging of polymer biomaterials by X-ray computed nanotomography. This is achieved by the exploration of two areas of interest: research and development of CT imaging itself, specifically propagation-based phase contrast imaging, and application of this technique on specific applications in material science.

2.1. Propagation-based phase contrast imaging

CT imaging of light materials like polymers and soft tissues is not as easy and straightforward as imaging of heavy, metal samples from industry, geology, and similar. These materials often do not have sufficient X-ray absorption and/or contrast in X-ray region. The problem of CT imaging of such samples is, in general, solved by staining to increase contrast or by use of specific imaging methods like phase contrast imaging.

The goal here is to explore phase contrast imaging with laboratory-based CT devices. Experiments optimising the propagation-based imaging (PBI) procedures will be designed, performed and evaluated. Results of this technique from several CT machines will be shown, including the work from the author's internships abroad.

Special focus will be on the post-processing of data acquired via PBI. This includes mainly the implementation of phase retrieval algorithms. A simple tool for easy testing and application of phase retrieval will be developed specifically for the needs of the Laboratory of X-ray computed micro and nanotomography at CEITEC BUT. Also, the influence of phase retrieval on data quality in dependence on measurement parameters will be studied.

2.2. Applications on biomaterials

Among other methods of material's imaging, the CT technique is distinguished by the possibility of studying the whole sample without its destruction and in 3D. A lot of information of interest can be derived from CT data (morphology characteristics, pore analysis, etc.) Nevertheless, it is often advantageous to complement CT data with other, quantitative technique since a basic CT measurement cannot determine the composition of the sample.

Several case-studies of CT imaging of various biomaterials (scaffolds, foams, ...) will be shown. They include phase contrast imaging and a few image analysis procedures. They may be done in VG Studio MAX software, Matlab, ImageJ or any other convenient tool. Another task in the thesis is a combination of CT data with other 2D or 3D analysing

2. AIMS OF THESIS

and imaging methods, such as optical or electron microscopy, serial sectioning etc. Two studies presenting such correlation will be shown.

3. Methods

3.1. CT devices

In this section, the CT devices used for experiments in this doctoral thesis topic are described: RIGAKU nano3DX, GE phoenix v|tome|x L240 and Thermo Fisher Scientific HeliScan located at the Brno University of Technology, and Zeiss Xradia nanoXCT-100 located at the University of Jyväskylä in Finland (Fig. 3.1). Technical details and specifications regarding sample preparation and imaging are included. The following shortcuts are used: LPS – linear pixel size, LVS – linear voxel size, FOV – field of view.

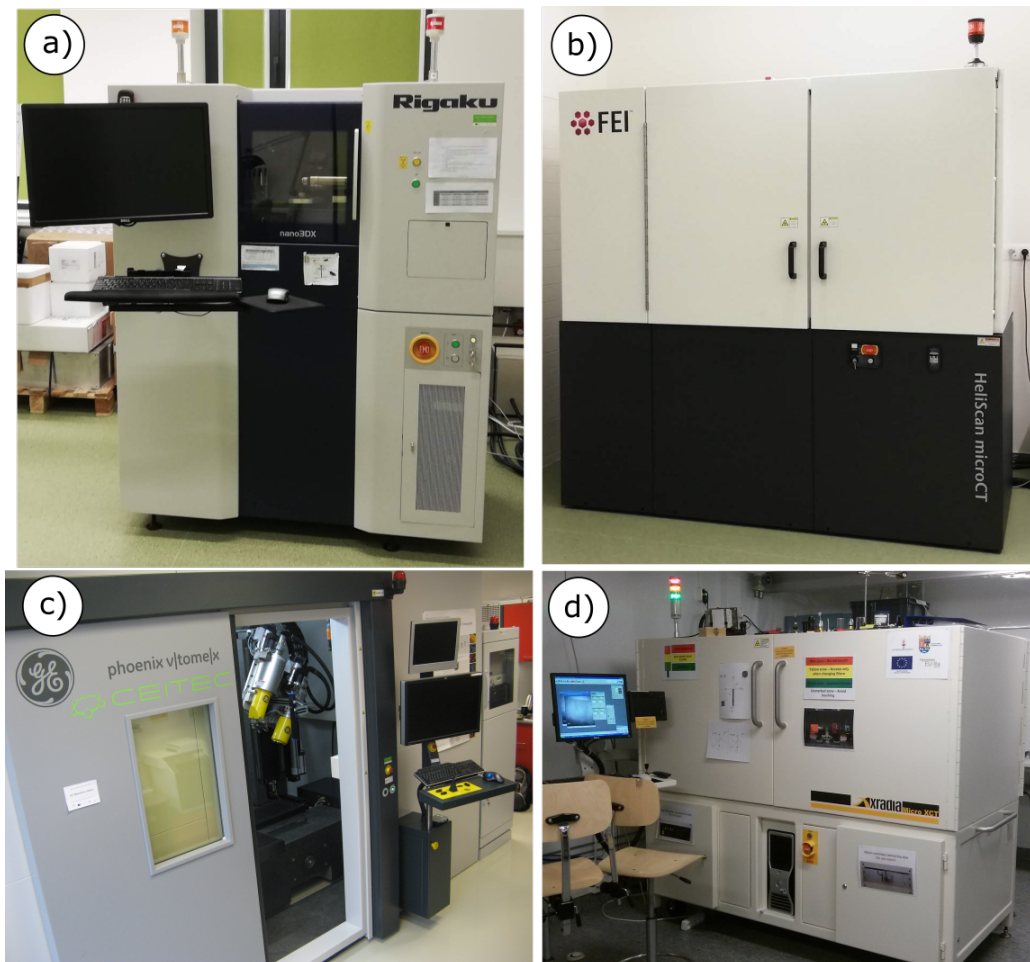


Figure 3.1: CT machines used in the thesis: a) RIGAKU nano3DX, b) Thermo Fisher Scientific HeliScan, c) GE phoenix v|tome|x L240, d) Zeiss Xradia nanoXCT-100.

3. METHODS

RIGAKU nano3DX

Most of the measurements are performed with CT device RIGAKU nano3DX, located at the Central European Institute of Technology, Brno University of Technology (Fig. 3.1a). The schematic diagram of the machine is in Fig. 1.15b). Sample–source distance is relatively large (≈ 260 mm) compared to the typical sample size (few mm), so the beam is considered semi-parallel at the sample stage.

The X-ray source is the RIGAKU rotating anode with three target materials available (Cu (40 kV tube voltage, 30 mA tube current), Mo (50 kV, 24 mA), and Cr (35 kV, 25 mA)). The focal spot size is $73\ \mu\text{m}$ for Cu and $156\ \mu\text{m}$ for Mo target measured according to the EN 12543-5 norm.

Experiments in the thesis are performed with two different types of X-ray cameras, CCD (charge-coupled device) and sCMOS (scientific complementary metal-oxide-semiconductor). The camera consists of a scintillator, magnification optics and a detector. Several optical units with different magnifications can be used to reach different effective LPS and FOV (for the smallest optical unit for CCD camera: LPS $0.27\ \mu\text{m}$, FOV $0.7 \times 0.9\ \text{mm}^2$).

CT measurements can be performed either in Continuous mode (the sample is continuously rotating during the measurement) or Step mode (the sample does not move during the acquisition of a projection). The typical scanning times are 1–3 hours. According to the author’s experience, it is necessary to prepare the sample in advance and to let it temperate in the sample chamber for at least several hours to avoid sample movement due to thermal expansion.

Thermo Fisher Scientific HeliScan

Thermo Fisher Scientific HeliScan CT device is located at the Central European Institute of Technology, Brno University of Technology (Fig. 3.1b). The system is equipped with micro-focus X-ray source with 8 W power with up to 160 kV voltage. The target material is tungsten. The focal spot size varies between $0.8\ \mu\text{m}$ and $4\ \mu\text{m}$ according to the applied settings (it is possible to choose from three different spot sizes in this range). The geometry of the system allows to set maximum source–sample distance 130 mm and maximum source–detector distance 750 mm. The detector is a large area 16-bit detector with 3072×3072 pixels with $139\ \mu\text{m}$ pixel size. When performing CT measurements, several scanning trajectories are available: circular and helical ones – single helix, double helix and space filling.

GE phoenix v|tome|x L240

CT device GE phoenix v|tome|x L240,, located at the Central European Institute of Technology, Brno University of Technology (Fig. 3.1c), was used for an application study. This large microCT system is placed in an air-conditioned cabinet. All components are on the granite-based 7-axis manipulator for long-term stability. The system has a cone beam geometry. The samples up to $500 \times 800\ \text{mm}^3$ and 50 kg can be scanned. The machine is equipped with a GE DXR 250 flat panel detector.

Zeiss Xradia nanoXCT-100

CT device Zeiss Xradia nanoXCT-100, located at the University of Jyväskylä in Finland (Fig. 3.1d), was used for an application study. Images were taken during 4-months Erasmus internship at this university from February to May 2018. With this machine, two imaging modes are available: absorption (without the phase ring) and phase contrast mode (with the phase ring). Rotating RIGAKU Cu anode (40 keV, 30 mA) emerges X-rays from $70\mu\text{m}$ focal spot. Two imaging modes are available: “Large field of view”, LFoV (LVS 65 nm , FOV $60 \times 60\mu\text{m}^2$), and “High resolution”, HiRes (LVS 10 nm , FOV $15 \times 15\mu\text{m}^2$).

The schematic diagram of the machine is in Fig. 3.2. A condenser capillary lens is installed to capture the X-rays and to focus them on the sample. To obtain a single focal spot, a pinhole is inserted just before the sample to isolate only the first order reflected X-rays. Fresnel zone plate is used as an objective. Optional phase ring is used to form a negative Zernike phase contrast. To reduce the loss of throughput, X-rays pass through flight tube filled with He gas. The detector consists of two magnifying lenses with scintillators (for alignment and imaging). X-rays converted to light are captured on a CCD camera.

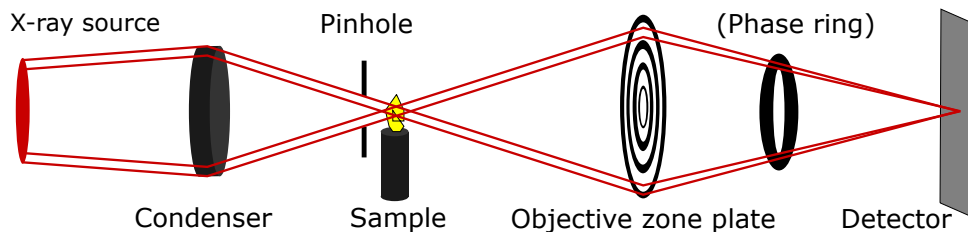


Figure 3.2: Xradia Zeiss nanoXCT-100 setup.

The whole system is very sensitive to the geometrical alignment of all components because X-rays are focused on a small spot on the sample. To reach optimal data quality, scanning times can be as high as several days. The final resolution is higher than the precision of mechanics of the sample stage. To overcome this difficulty, for every measurement, a gold microparticle has to be inserted into the sample. It is also used later for alignment of projections.




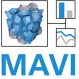

Since the field of view is very small, additional tools have to be used for sample preparation. For manipulation with the sample and the needle, micro-manipulators Sensapex SMX and micro-grippers SmarAct are used. The preparation is observed via a Leica Z16 APO microscope. If needed, the sample can be cut via laser on a QuikLaze CMPS-888L machine.

3. METHODS

3.2. Software

The following software for data processing was used during work on this thesis (Tab. 3.1).

Table 3.1: List of software used in this thesis for data analysis.

	Fiji open source [106, 107]
	MATLAB MathWorks, USA [108]
	VGStudio MAX Volume Graphics, Germany [109]
	MAVI Fraunhofer Institute for Industrial Mathematics, Germany [110]
	Pore3D open source software for commercial IDL [111]

3.3. Image evaluation parameters

Several parameters for image evaluation are introduced in Fig. 3.3. Let I_{MAT} and I_{BCG} be the averaged grey value intensities from areas inside sample material and in the background, respectively. If a line profile is generated¹, I_{MAT} and I_{BCG} correspond to the intensities at the ends of the line². $I_{20\%}$ and $I_{80\%}$ correspond to 20% and 80% of the intensity difference between I_{MAT} and I_{BCG} . $x_{20\%}$ and $x_{80\%}$ correspond to the horizontal axis value of $I_{20\%}$ and $I_{80\%}$, respectively. I_{MAX} and I_{MIN} are the maximum and minimum values in the line profile, respectively.

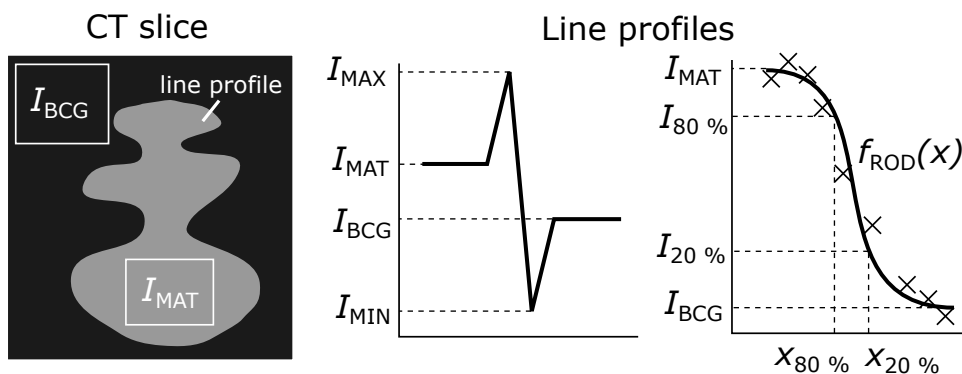


Figure 3.3: Variables used in image evaluation parameters.

¹Usually, several pixels above and below the line are averaged to reduce the noise.

²Usually, several utmost pixels are averaged to reduce the noise.

Parameters based on information from selected area

- Histogram. Graphical representation of grey values distribution in a given area (typically a CT slice).
- Signal to noise ratio SNR^3 .

$$\text{SNR} = \frac{I_{\text{MAT}}}{\text{std } I_{\text{BCG}}}$$

- Signal to noise ratio gain SNR_{gain}

$$\text{SNR} = \frac{\text{SNR}(\text{phase retrieved image})}{\text{SNR}(\text{original image})}$$

Parameters based on line profile

- Absorption contrast C_{ABS}

$$C_{\text{ABS}} = \frac{I_{\text{MAT}} - I_{\text{BCG}}}{(I_{\text{MAT}} - I_{\text{BCG}})/2}$$

- Absorption contrast gain $C_{\text{ABS, gain}}$

$$C_{\text{ABS, gain}} = \frac{C_{\text{ABS}}(\text{phase retrieved image})}{C_{\text{ABS}}(\text{original image})}$$

- Phase contrast C_{PHC}

$$C_{\text{PHC}} = \frac{I_{\text{MAX}} - I_{\text{MIN}} - (I_{\text{MAT}} - I_{\text{BCG}})}{I_{\text{MAX}} + I_{\text{MIN}}}$$

- Let f_{ROD} be the Rodbard function fitted to line profile with parameters a, b .

$$f_{\text{ROD}}(x) = I_{\text{BCG}} + \frac{I_{\text{MAT}} - I_{\text{BCG}}}{1 + (\frac{x}{b})^a}$$

- Edge resolution R_{E}

$$R_{\text{E}} = |x_{20\%} - x_{80\%}|$$

- Standard deviation of fitting of Rodbard function STD_{ROD}

$$\text{STD}_{\text{ROD}} = \sqrt{\frac{\sum_i^N [I(x_i) - f_{\text{ROD}}(x_i)]^2}{N}}$$

³std x means standard deviation of x .

3. METHODS

4. Propagation-based imaging

4.1. Characterization of lab-CT systems for PBI

With knowledge of parameters of a CT machine, it is possible to estimate suitability of the device for propagation-based imaging based on criteria explained in Sec. 1.2.1. In this thesis, two CT machines (RIGAKU nano3DX (Sec. 3.1) and Thermo Fisher Scientific HeliScan (Sec. 3.1)) are described and discussed in terms of PBI. Calculations are supplemented with measurements of polymeric samples.

4.1.1. PBI on nano3DX

The study was published by the author of the thesis in [37], titled “Characterization of a laboratory-based X-ray computed nanotomography system for propagation-based method of phase contrast imaging”. A copy of the original article is included in Appendix B.

Abstract

“Phase-contrast imaging (PCI) is used to extend X-ray computed nanotomography (nCT) technique for analyzing samples with a low X-ray contrast, such as polymeric structures or soft tissues. Although this technique is used in many variations at synchrotrons, along with the recent development of X-ray tubes and X-ray detectors, a phase contrast imaging becomes available also for laboratory systems.

This work is focused on determining the conditions for propagation-based PCI in laboratory nCT systems based on three criteria. It is mostly employed in near-field imaging regime, which is quantified via Fresnel number. X-rays must reach certain degree of coherence to form edge-enhancement. Finally, setup of every CT measurement has to avoid geometrical unsharpness due to the finite focal spot size. These conditions are evaluated and discussed in terms of different properties and settings of CT machine. Propagation-based PCI is tested on a sample of carbon fibres reinforced polyethylene and the implementation of Paganin phase retrieval algorithm on the CT data is shown.” [37]

4. PROPAGATION-BASED IMAGING

4.1.2. PBI on HeliScan

A study similar to the evaluation of PBI on RIGAKU nano3DX (Sec. 4.1.1) was also carried out with CT device Thermo Fisher HeliScan. The preliminary results were presented by the author of this thesis at the International Conference on Tomography of Materials and Structures in Cairns, Australia, on July 2019. Up to the date of submitting of this thesis, the experimental results are still under evaluation, and they are planned to be published in an impacted journal in autumn 2019 or winter 2020. Therefore here, only numerical evaluation is provided.

Theoretical estimation of PBI abilities of HeliScan includes evaluation of imaging regime represented by Fresnel number N_F , visibility of PBI effects related to a degree of X-ray coherence represented by $L_{\text{shear}}/L_{\text{lat}}$ ratio, and geometrical unsharpness due to finite focal spot size according to Sec. 1.2.1. In contrast to nano3DX, HeliScan offers more variability in terms of setting source–sample distance (denoted here as sample position y_S), source–detector distance (denoted here as y_D), X-ray tube voltage, and focal spot size. The calculations are made for two effective propagation distances, 5 mm and 10 mm. These two represent two measurement settings with different sample and detector positions and the same linear voxel size $2\ \mu\text{m}$ (Tab 4.1). As a wavelength, the mean energy of spectra with acceleration voltage 50 kV generated by SpekCalc software [2] was used, unless stated otherwise.

Table 4.1: Two possible geometrical settings of Thermo Fisher HeliScan to reach different effective propagation distances.

Source–sample distance y_S [mm]	Source–detector distance y_D [mm]	Effective propagation distance z_{eff} [mm]
5	300	5
11	718	11

Dependence of the Fresnel number on the structural component of size a according to Eq. 1.6 shows a quick increase to very high numbers ($\gg 1$) for both measurements (Fig. 4.1a). Thus, the imaging is in the near field regime for all recognizable features (considering the linear voxel size of $2\ \mu\text{m}$). The edge enhancement should be the most pronounced for small features of size about a few microns.

The imaging regime does not depend on focal spot size, but it can vary with the X-ray energy. The plot of N_F for different X-ray tube voltages (thus mean X-ray energy of the spectra) suggests that this parameter is not much significant for the imaging regime in the range of energies available for HeliScan (Fig. 4.1b).

Both sets of measurements have almost identical dependence of $L_{\text{shear}}/L_{\text{lat}}$ ratio on a (Fig. 4.2a according to Eq. 1.7). The differences are not visible on the displayed scale. However, the degree of coherence is influenced by the focal spot size (Fig. 4.2b). If the smaller spot size is used, the phase effects are better visible.

Distances of both the sample and the detector from the source can be varied. A user has to select them carefully to avoid geometrical unsharpness due to finite focal spot size. All possible pairs of y_S and y_D lay in the region restricted by lines in Fig. 4.3 calculated using Eq. 1.8.

4.1. CHARACTERIZATION OF LAB-CT SYSTEMS FOR PBI

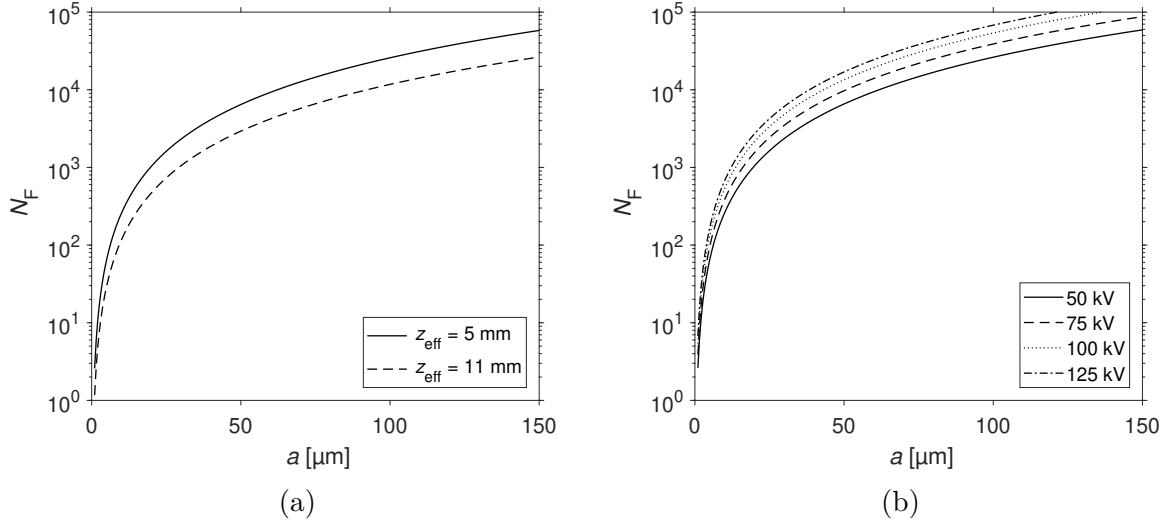


Figure 4.1: Fresnel number N_F dependence on structural component of size a according to Eq. 1.6. a) Plot for two sets of measurements with different effective propagation distances (Tab 4.1), b) plot for the spot size $0.8 \mu\text{m}$, geometrical settings $y_S = 5 \text{ mm}$, $y_D = 300 \text{ mm}$, and for different X-ray tube voltages.

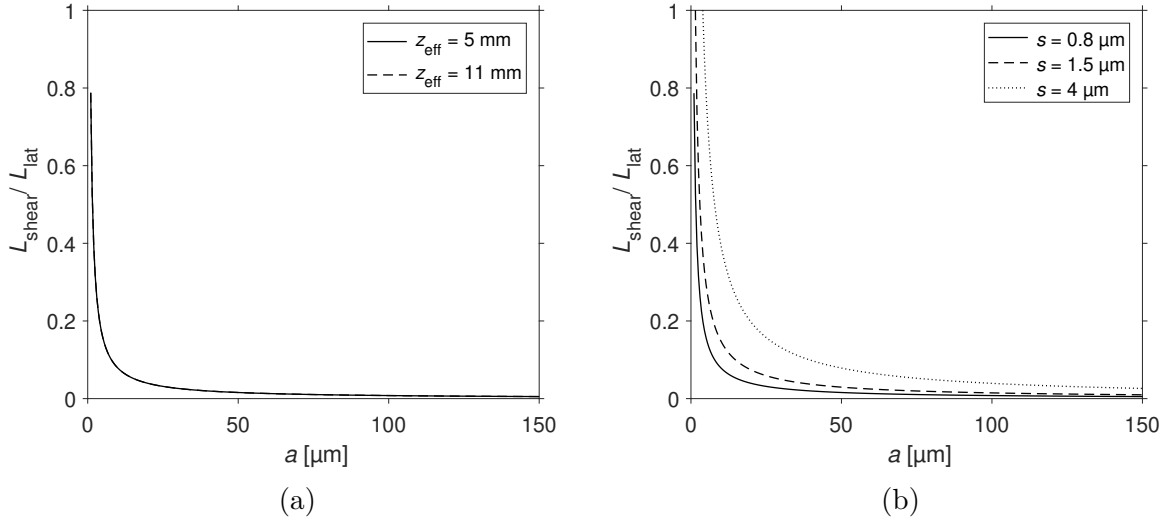


Figure 4.2: $L_{\text{shear}}/L_{\text{lat}}$ dependence on structural component of size a according to Eq. 1.7. a) Plot for two sets of measurements with different effective propagation distances (Tab 4.1), b) plot for the X-ray tube voltage 50 kV , geometrical settings $y_S = 5 \text{ mm}$ and $y_D = 300 \text{ mm}$ and for different spot sizes.

4. PROPAGATION-BASED IMAGING

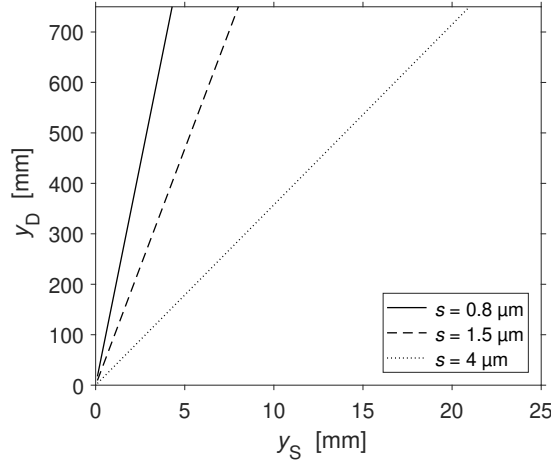


Figure 4.3: Maximum detector position y_D to avoid geometrical unsharpness for different spot sizes according to Eq. 1.8.

4.2. Phase retrieval implementation

4.2.1. Influence of phase retrieval on image quality

From the physics point of view, the phase retrieval in PBI is used to calculate the phase from intensity data. In practical use, it enhances data quality by removing edge enhancement, increases contrast and SNR, and often it is a necessary step to obtain data which can be segmented automatically. It is shown, for example, in [41] and in the author’s paper [37].

Example

The Paganin phase retrieval algorithm [75] implemented in the ANKPhase software [69] was used on the data of a light-element composite made of polyethylene matrix reinforced carbon fibres (CFRP) measured with nano3DX with CCD camera at SDD $1.5 \mu\text{m}$, bin 2, LPS $0.54 \mu\text{m}$, 800 projections and 9 s exposure time. The δ/β ratio of values in the index of refraction n was chosen as 780 for polyethylene. [37, 112]

“By an application of the phase retrieval on tomographic data (Fig. 4.4), the edge enhancement was reduced compared to the original data, as it is shown on the edge profile (Fig. 4.5). The absorption contrast increased ($C_{\text{ABS}} = 0.004$ for original data, $C_{\text{ABS}} = 0.366$ with phase retrieval) and the phase contrast decreased ($C_{\text{PHC}} = 0.152$ for original data, $C_{\text{PHC}} = 0.139$ with phase retrieval), which is very convenient for material segmentation.

The histogram after phase retrieval (Fig. 4.5) contains several peaks corresponding to different structures and allowing the segmentation of different parts (air, matrix and carbon fibres). Without the phase retrieval, the histogram of data has only one peak which makes segmentation very challenging. This is the reason why it is sometimes useful to apply the algorithm also on data without any strong visible edge enhancement, a further analysis is easier on these data from the image processing point of view.” [37]

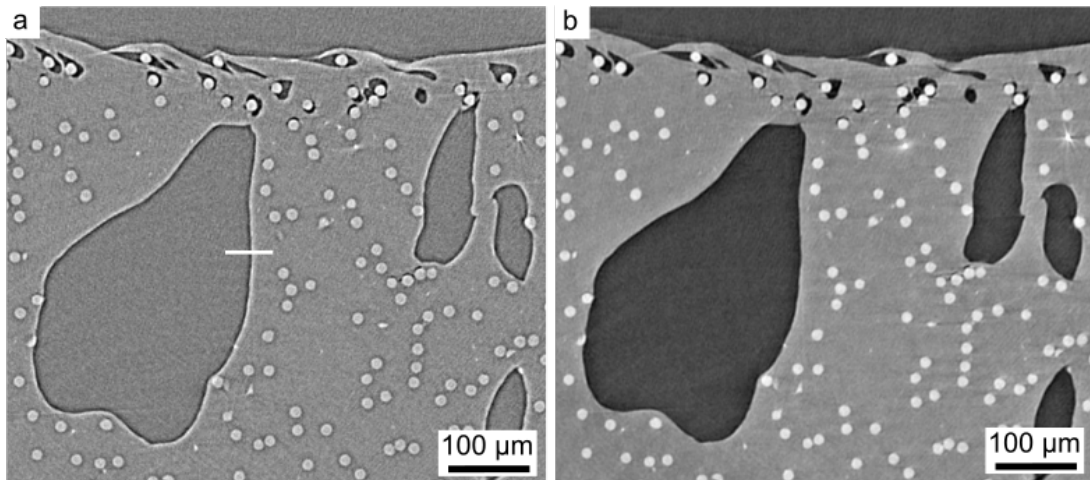


Figure 4.4: Tomographic slice of the CFRP sample. a) original reconstruction, b) phase retrieval. [37]

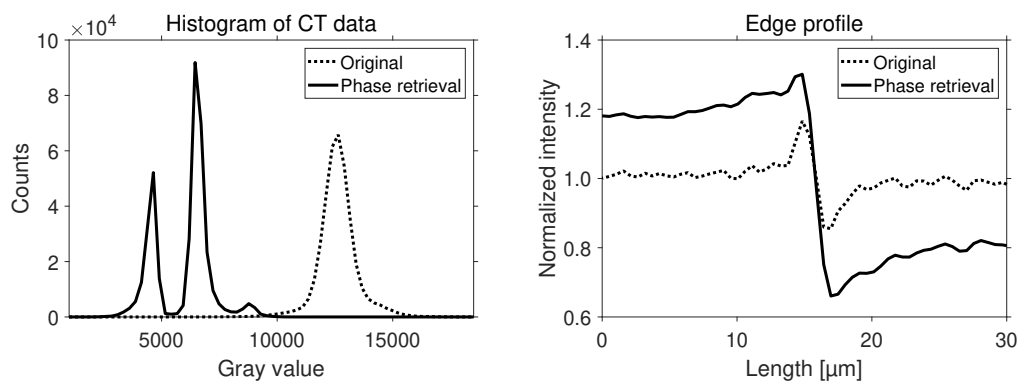


Figure 4.5: Image evaluation of tomographic slices of the CFRP sample from Fig. 4.4. Averaged edge profile and histogram are used to show the influence of phase retrieval on CT data. [37]

4.2.2. Matlab GUI

During her internship in RIGAKU company (Tokyo, Japan) in autumn 2018, the author of the thesis studied propagation-based phase contrast imaging with the nCT system RIGAKU nano3DX. She created a graphical user interface (GUI) in Matlab [108] for application of phase retrieval on data from nano3DX. The program includes several algorithms (PA – Eq. 1.10, MBA – Eq. 1.13, BAC – Eq. 1.14). In practice, a sample usually contains several materials, so it is difficult to determine the exact physical value of parameters for phase retrieval. Therefore a test mode for choosing optimal parameters is included. Up to the date of submitting of this thesis, this GUI is being implemented into official RIGAKU software, and it will be provided to customers in 2020.

In the main window of the GUI (Fig. 4.6a), in the panel *Input files*, the user selects a .raw file containing projections. Data from the measurement from the .ctm file with the same name are loaded to generate the input parameters for phase retrieval (dimensions of the file, wavelength, sample–detector distance, pixel size). It is possible to go through the projections by the horizontal slider and select a slice for testing by the vertical slider.

In the panel *Choose mode*, a mode for testing (on a slice or an projection) or execution is selected. This choice enables one of the two panels. The *Execution mode setting* panel (Fig. 4.6b) is used for performing phase retrieval on the whole .raw file with user-defined parameters optimised in the *Test mode*. Phase-retrieved files called *..._phase_algorithm_parameter.raw* and corresponding .ctm files are generated.

The panel *Test mode setting* is meant to find optimal algorithms and parameters for the phase retrieval in individual measurements. The software can save all combinations of interest as .tiff files or show them in another window (Fig. 4.6c). Phase retrievals are showed either on projections or slices, according to the choice in the *Test on* panel (if on slices, a user has to insert a correct centre of rotation). Before the window opens, a user is asked to select a line and a material and background area to evaluate image quality. The window contains two panels, with the original and phase-retrieved images. In the latter, it is possible to move the slider to change the algorithms and parameters. For each image, a histogram and a line profile are shown. Image evaluation parameters SNR, absorption contrast, phase contrast and edge resolution, as they are introduced in Sec. 3.3, are shown.

4.2. PHASE RETRIEVAL IMPLEMENTATION

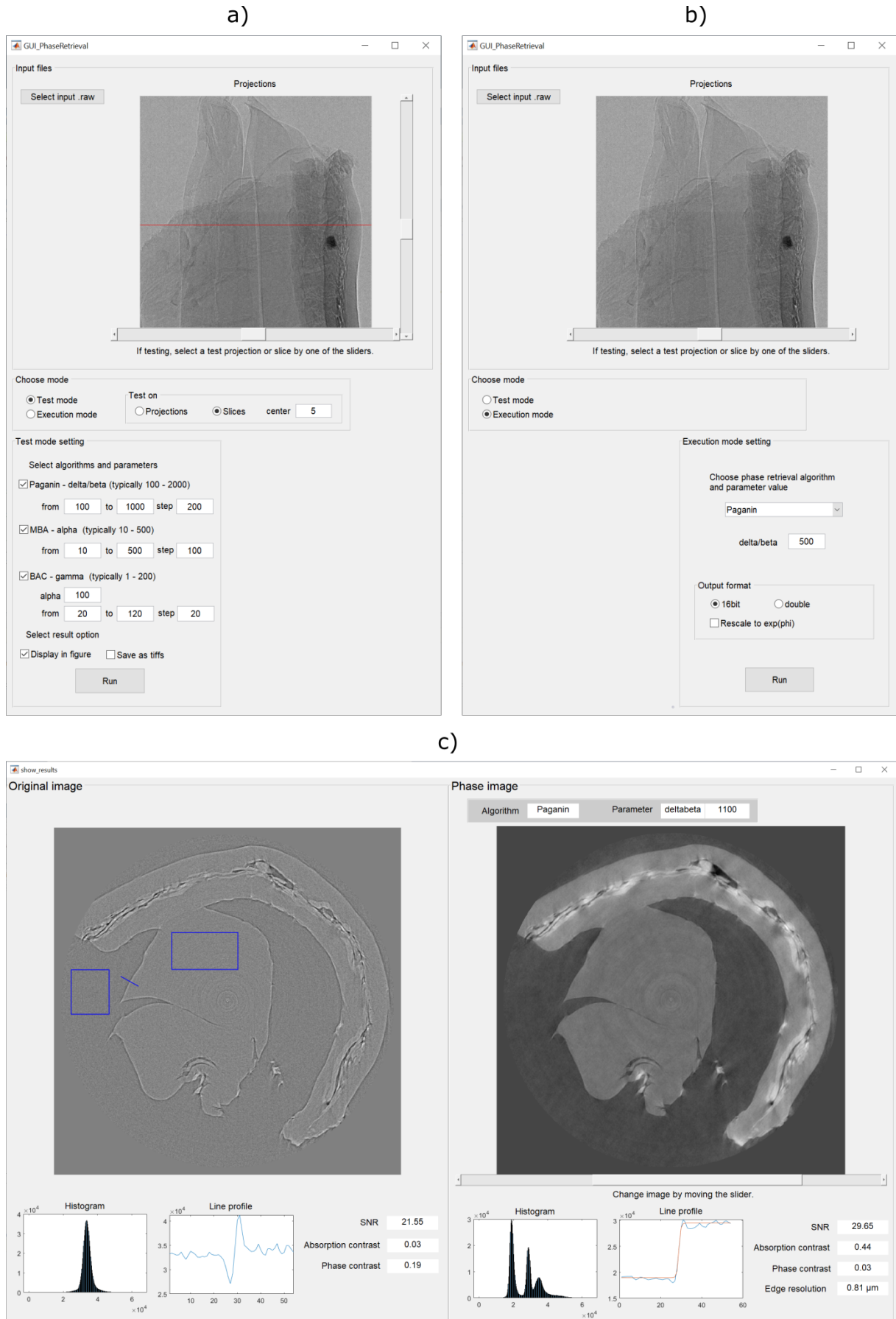


Figure 4.6: a)–c) graphical user interface in Matlab of a program, which implements phase retrieval on data from nano3DX.

4. PROPAGATION-BASED IMAGING

4.2.3. Optimisation of phase retrieval parameters

Methodology

The influence of phase retrieval parameter on resulting data is studied on a sample of polyethylene rod with double-sided tape (PEDT) measured on nano3DX with sCMOS camera in the Continuous scanning mode for 15 min with Cu target, SDD 1.5 mm, bin 2, linear voxel size $0.64\ \mu\text{m}$ and 600 projections. The sample consists of two polymers with slightly different density, which makes it a suitable sample for testing of PBI. The slice reconstructed without phase retrieval is in Fig. 4.7. Areas for image evaluation according to Sec. 3.3 are highlighted. The data were processed with phase retrieval, Paganin algorithm, for δ/β values from 100 to 2800.

Results

Slices and details of a selected area are presented in Fig. 4.9 together with corresponding histograms and line profiles. Several image evaluation parameters (Fig. 4.8) assess the influence of the choice of phase retrieval δ/β parameter to image quality.

When the δ/β value is set very low (close to 100 or lower), the image is very similar to the original image, as well as other characteristics. With increasing δ/β , the histogram becomes multi-modal, edge-enhancement disappears, SNR and C_{ABS} increase and C_{PHC} decreases. These improvements make the data look better, less noisy, and the segmentation of individual parts gets easier. On the other hand, the value of edge resolution R_{E} increases with increasing δ/β and some of the details in the structure can be lost. Overall blurring is visible in slices with δ/β above approximately 1500.

A closer look at the parameters can help to choose an optimal parameter for phase retrieval. SNR improvement is not linear with increasing δ/β and from some value, here about $\delta/\beta = 1000$, it starts to saturate. C_{PHC} does not decrease completely to 0, but there is a minimum about value $\delta/\beta = 1000$. This is related to the “sharpness” of the edge, which is described by STD_{ROD} . It has a minimum about the values 800–1000 as well.

Based on this thorough analysis, δ/β in the interval 800–1000 should be chosen to reach the optimal data quality with Paganin phase retrieval. It is slightly higher than the tabulated value for polyethylene, $\delta/\beta = 780$ [37, 112]. Using a similar analysis, it is possible to choose an optimal parameter for phase retrieval in the CT measurements.

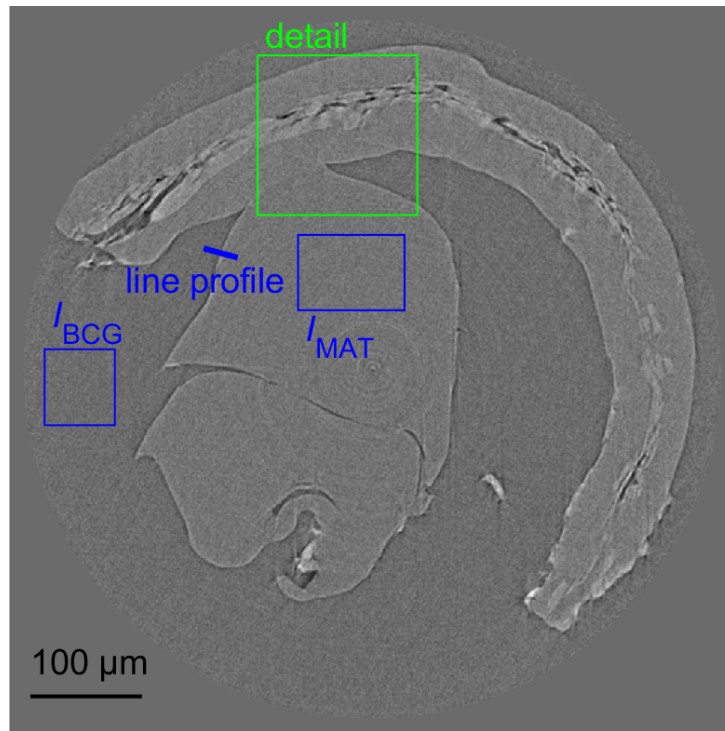


Figure 4.7: CT slice of the PEDT with highlighted areas for image evaluation.

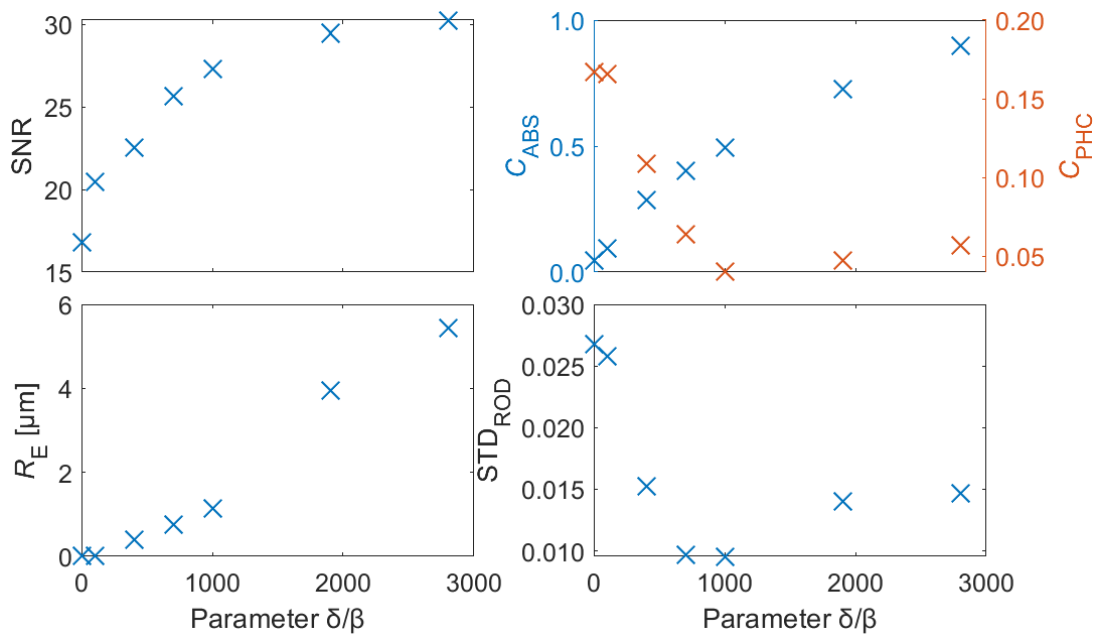


Figure 4.8: Dependence of various image evaluation parameters (Sec. 3.3) on δ/β value in phase retrieval (Paganin algorithm). The point $\delta/\beta = 0$ corresponds to data without phase retrieval. The data are shown in Fig. 4.9.

4. PROPAGATION-BASED IMAGING

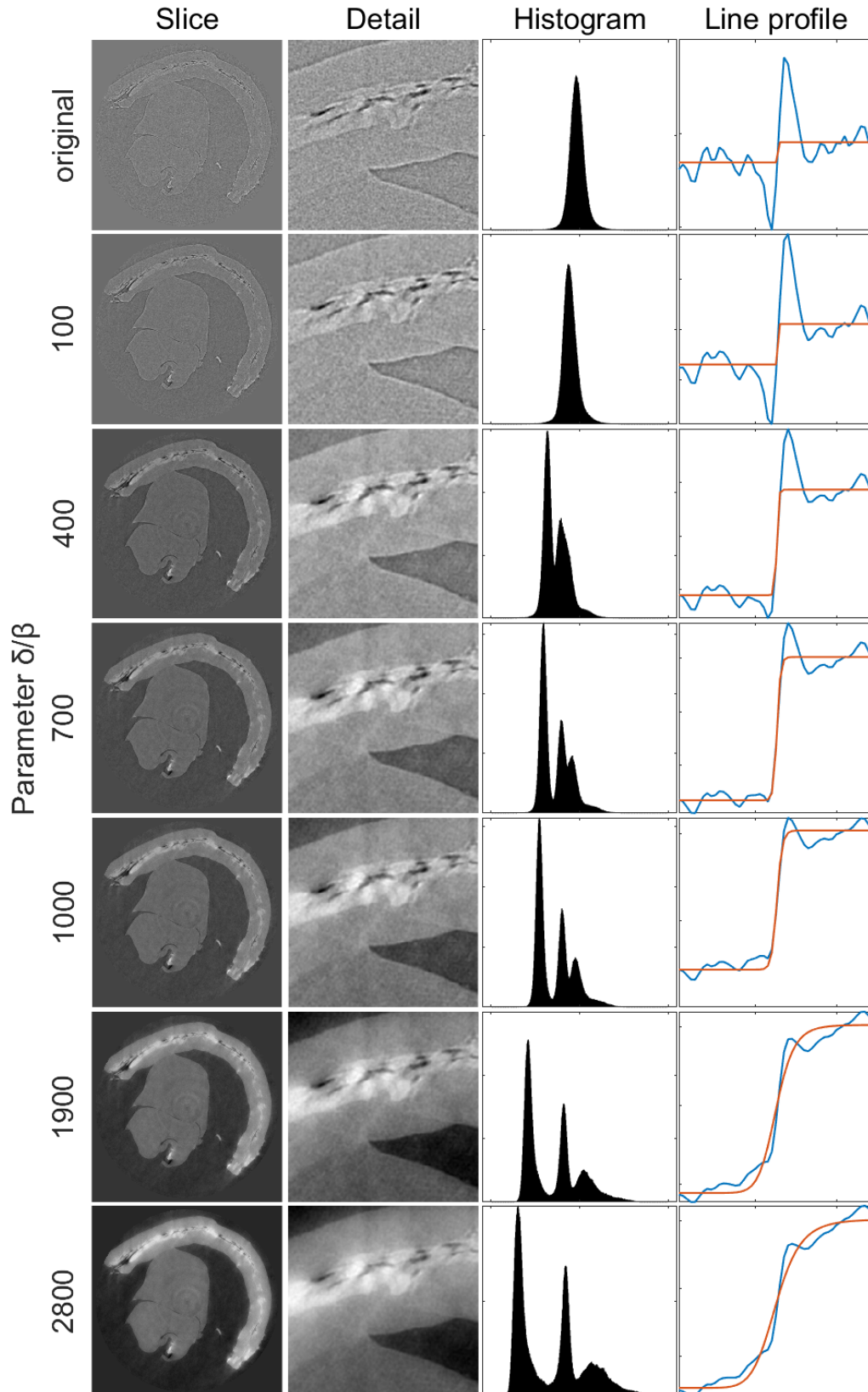


Figure 4.9: CT slices of the PEDT (first row). Paganin phase retrieval algorithm was applied with different δ/β values from 100 to 2800. For each image, a detail, a histogram and a line profile (blue) with fitted Rodbard function (orange) are shown in second, third and fourth column, respectively.

4.2.4. Comparison of phase retrieval algorithms

Methodology

The differences between four mostly used phase retrieval algorithms (Paganin algorithm – PA, Modified Bronnikov algorithm – MBA, Bronnikov aided correction – BAC) (Figs. 4.11, 4.12) are studied on a sample of polyethylene rod with double-sided tape (PEDT) measured on nano3DX with sCMOS camera in the Continuous scanning mode for 15 min with Cu target, SDD 1.5 mm, bin 2, linear voxel size $0.64\ \mu\text{m}$ and 600 projections. The sample consists of two polymers with slightly different density, which makes it a suitable sample for testing of PBI. The slice reconstructed without phase retrieval with highlighted areas for image evaluation according to Sec. 3.3 is in Fig. 4.10.

Results

Slices processed with different algorithms (Figs. 4.11, 4.12) are accompanied with corresponding histograms (Fig. 4.13) and line profiles (Fig. 4.14). Several image evaluation parameters are calculated (Tab. 4.2) to discuss the influence of the algorithms on data.

The PA and MBA strongly reduce edge enhancement (in comparison with the original image, they have low values of C_{PHC} , STD_{ROD} , high values of C_{ABS}) and increase SNR. At the same time, the edge resolution gets worse for them as they filter out high frequencies. Indeed, in the detailed images, the PA and especially MBA are the most blurred images with some loss of detail. The BAC, on the other hand, preserves the details of the original image and increases C_{ABS} as well. However, the histogram shape has only one peak, which makes the segmentation difficult. The SNR increase is not as significant as in the case of PA.

The relatively worst performance of the MBA can be explained by the invalid assumption of a pure phase object since there is some X-ray absorption in the sample. Assumption of a single-material object with the PA is reasonably valid (all parts of the sample are similar polymers), hence the results are good and artefact-free. However, the BAC achieves the smallest loss of resolution compared to original data. The authors in [74] compared these algorithms on a sample of a spider stained with iodine and came up with a similar conclusion. To sum up, when one needs to focus on resolving the details of the structure, the BAC is recommended. If an easy segmentation and further post-processing is the priority, the PA is a good choice.

Table 4.2: Image evaluation parameters of CT slices of PEDT with different phase retrieval algorithms.

Algorithm	SNR	C_{ABS}	C_{PHC}	$R_{\text{E}} [\mu\text{m}]$	STD_{ROD}
without	17	0.04	0.17	0.02	1754
Paganin algorithm	27	0.47	0.05	1.01	601
Modified Bronnikov alg.	30	0.27	0.08	0.73	775
Bronnikov aided correction	16	0.17	0.11	0.08	1083

4. PROPAGATION-BASED IMAGING

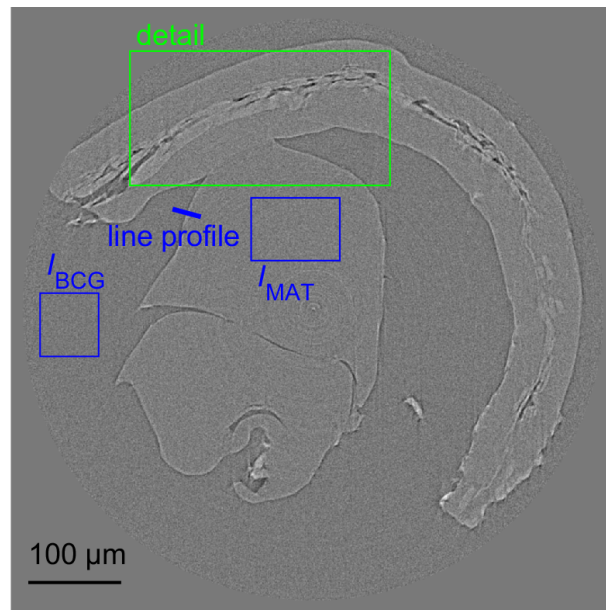


Figure 4.10: CT slice of the PEDT with highlighted areas for image evaluation.

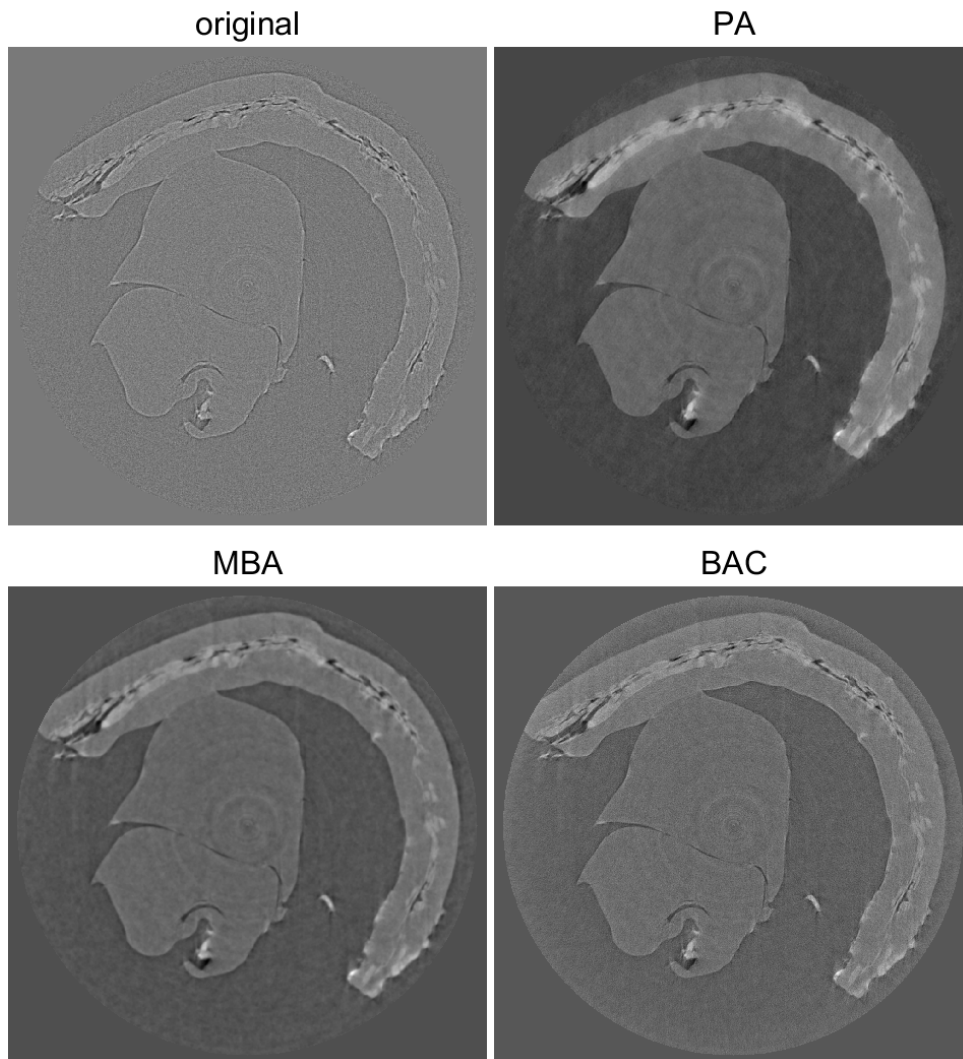


Figure 4.11: CT slices of PEDT with different phase retrieval algorithms (Paganin algorithm – PA, Modified Bronnikov algorithm – MBA, Bronnikov aided correction – BAC).

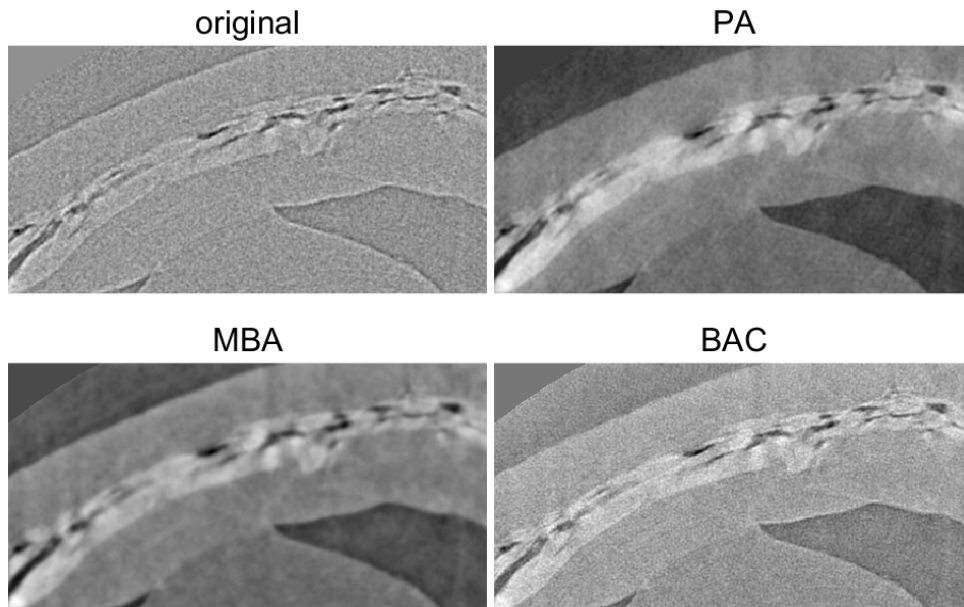


Figure 4.12: Details of CT slices of PEDT with different phase retrieval algorithms (Paganin algorithm – PA, Modified Bronnikov algorithm – MBA, Bronnikov aided correction – BAC).

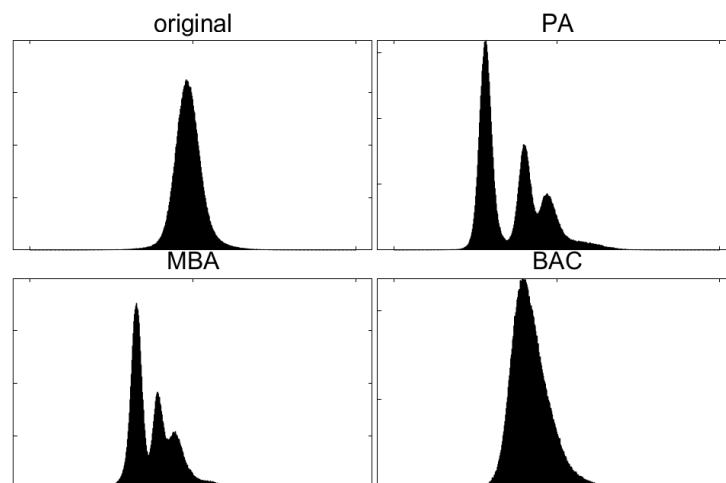


Figure 4.13: Histograms of CT slices of PEDT with different phase retrieval algorithms (Paganin algorithm – PA, Modified Bronnikov algorithm – MBA, Bronnikov aided correction – BAC).

4. PROPAGATION-BASED IMAGING

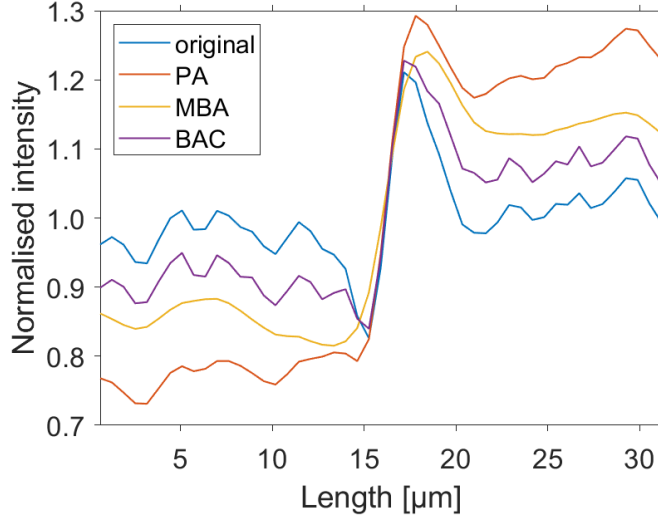


Figure 4.14: Line profiles in CT slices of PEDT with different phase retrieval algorithms (Paganin algorithm – PA, Modified Bronnikov algorithm – MBA, Bronnikov aided correction – BAC).

4.3. Optimisation of measurement parameters for PBI with nano3DX

When performing absorption CT with nano3DX, the setting is rather simple – a detector is placed close to a sample, a sample is centered so that the feature of interest is in the field of view for all angles, and the exposure time is set so there is enough signal on the detector. The minimal signal required for the data obtained with sufficient quality is defined by the manufacturer of the CT machine. However, an optimal signal needed for PBI is not defined. This study was designed to verify whether increasing exposure time or adjusting the sample–detector distance has a positive, if any, effect on quality of PBI data. Since PBI data are usually processed with phase retrieval, the main figures of merit are the SNR_{gain} and $C_{\text{ABS, gain}}$ (Sec. 3.3).

Methodology

The light-element composite made of polyethylene matrix reinforced with carbon fibres (CFRP) was used for the testing (the same sample as in Sec. 4.1.1). Two kinds of experiments with nano3DX with the CCD camera were performed. The CT scans were performed at two different SDDs (2 mm and 5 mm) with three exposure times each (9 s corresponding to the signal defined by manufacturer, 12 s and 15 s) (Tab. 4.3a). Shorter exposure times were avoided to exclude low signal data. Longer exposure times were not tested since they are used only sporadically resulting in long measurement times. All measurements were performed with bin 2, LPS $0.54\mu\text{m}$ and 800 projections. The SDD 2 mm corresponds to maximum SDD which is allowed to avoid geometrical unsharpness in this case [37]. The second SDD, 5 mm, was longer than this one, relying on the premise that advantages of bigger phase contrast outweigh or compensate the loss of resolution.

To further study limits of the machine’s settings, the second set of measurements was proposed with only projections taken at distances 2 mm, 5 mm and 8 mm and exposure

4.3. OPTIMISATION OF MEASUREMENT PARAMETERS FOR PBI WITH NANO3DX

times 6 s (lower signal then recommended), 9 s, 12 s, 15 s and 25 s (longer exposure time would result in saturation of the detector) (Tab. 4.3b). The measurements were performed with bin 2, LPS $0.54\ \mu\text{m}$.

The Paganin phase retrieval was applied with δ/β ratio 780, the value for polyethylene [37, 112]. All slices had been normalised before image evaluation unless stated otherwise. Applied image evaluation parameters are listed in Sec. 3.3. The evaluated areas are highlighted in corresponding CT slices and projections in Fig. 4.15.

		Exposure time [s]			Exposure time [s]			
		9	12	15	6	9	15	25
SDD [mm]	2	✓	✓	✓	✓	✓	✓	✓
	5	✓	✓	✓	✓	✓	✓	✓
	8	✓	✓	✓	✓	✓	✓	✓

(a) CT scans
(b) Projections

Table 4.3: Experiments designed to optimize PBI with nano3DX.

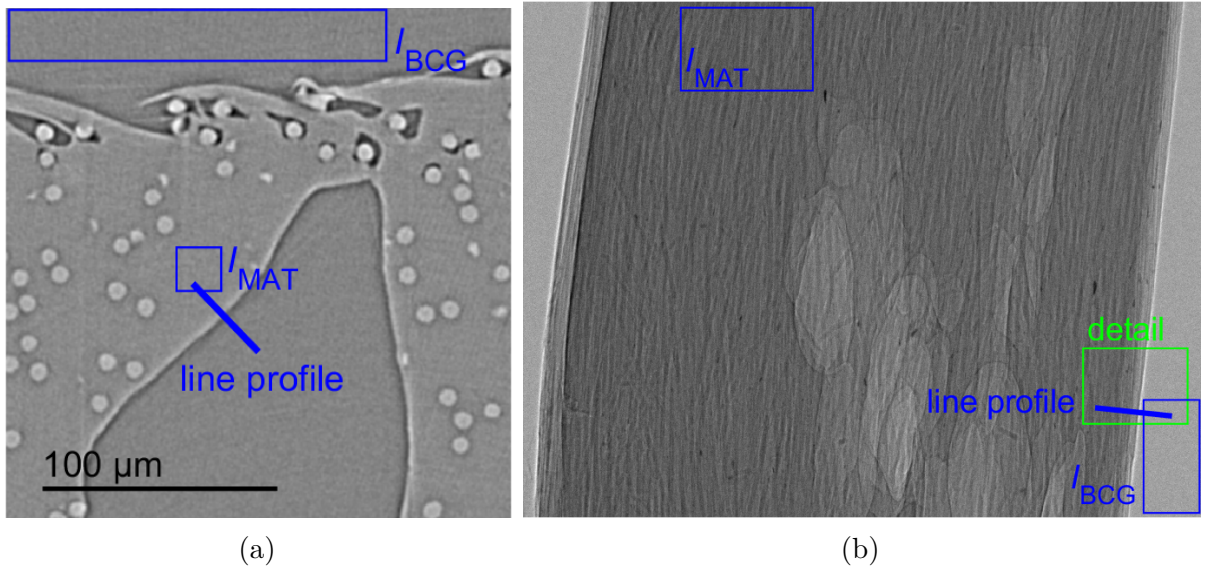


Figure 4.15: Image evaluation regions of measurements of CFRP, a) CT slice, b) projection.

Results

In the data from CT scans, which were obtained in a relatively small range of SDD and exposure times, there is no big visual difference either in original nor in phase retrieved slices (Figs. 4.16, Fig. 4.17). In projections data, a higher amount of edge enhancement is visibly present at higher SDDs, and the decreasing amount of noise with increasing exposure time is noticeable (Fig. 4.18 and Figs. A.1, A.2 in Appendix A). This results in SNR increasing with exposure time (Figs. 4.19a, 4.20a). However, SNR_{gain} is higher for lower exposure times (Figs. 4.19b, 4.20b), which suggests that with use of phase retrieval, it is not necessary to increase exposure time in PBI measurement to get better

4. PROPAGATION-BASED IMAGING

results. It may be possible to use a little bit lower exposure time than necessary in cases, where the radiation damage could be a problem.

C_{ABS} or $C_{\text{ABS, gain}}$ does not change significantly within a small range of exposure times (Figs. 4.21, 4.22). For higher exposure times like 25 s, the contrast significantly drops (Fig. 4.22a). It is understandable from the examination of histograms of individual projections. Peaks in histograms of non-normalised projections are shifted to the right with increasing exposure time (Fig. 4.23). From some point, the response of the detector to incoming X-rays is no longer linear, and the contrast between the sample and background decreases. It also means that peaks of a sample and background are closer to each other in histograms of normalised projections (Fig. 4.24).

SNR_{gain} is, in general, bigger for lower SDDs (Figs. 4.19b, 4.20b). It is the opposite trend than in CT slices (Fig. 4.19a). $C_{\text{ABS, gain}}$, on the other hand, is lower for lower SDDs (Figs. 4.21b, 4.22b). C_{ABS} does not depend on SDD very much. Nevertheless, with increasing SDD, the data are more blurred due to finite focal spot size, which is usually the more important issue.

Summary

The results of this study suggest that there is no substantial change in the quality of phase retrieved PBI data if a user varies the experimental conditions in a small range, which is reasonable for the actual measurement. It is possible to increase the exposure time to get data with higher SNR, but one has to avoid using non-linear part of the detector's sensitivity, and the contrast and SNR gain is not very significant. For nano3DX, this means keeping the exposure time as recommended by the manufacturer. It is acceptable to increase the maximum allowed SDD restricted by geometrical unsharpness to obtain more phase contrast, but only about a small amount (a few millimetres).

4.3. OPTIMISATION OF MEASUREMENT PARAMETERS FOR PBI
WITH NANO3DX

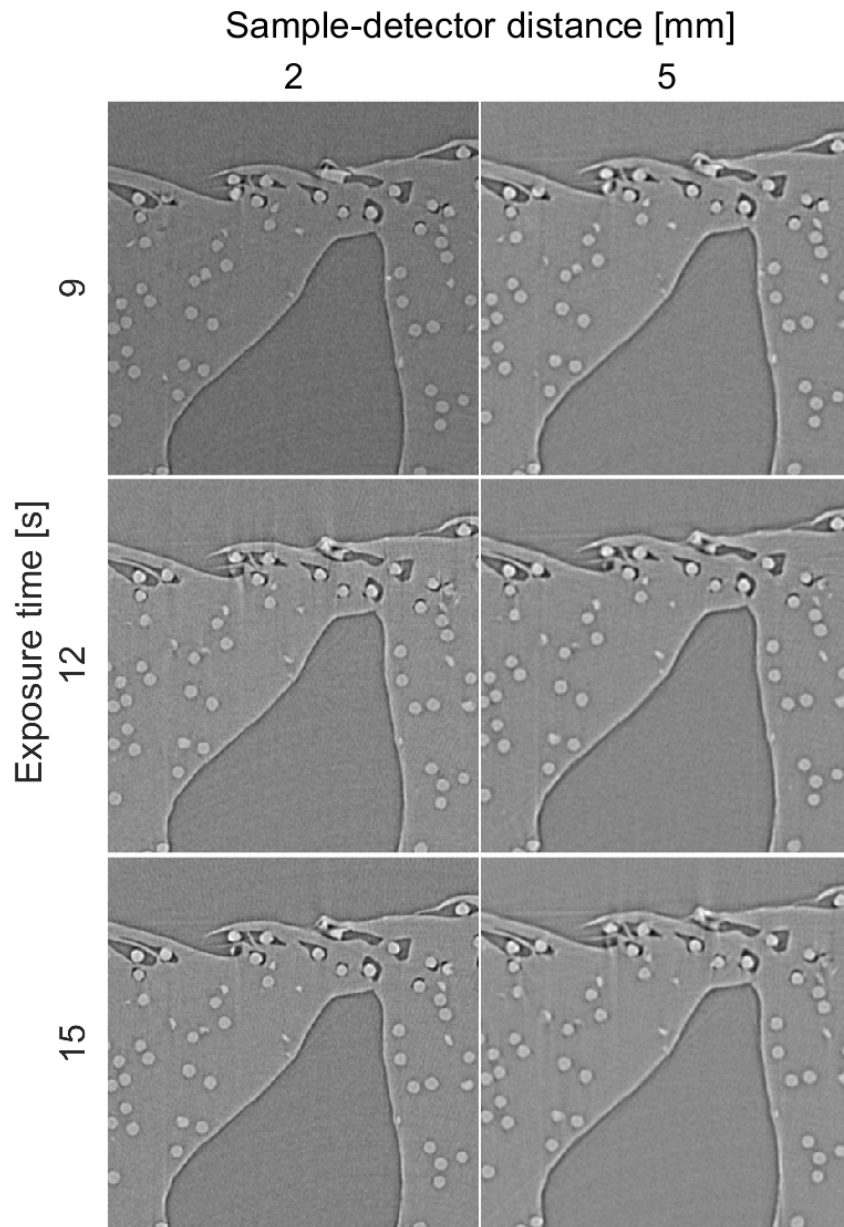


Figure 4.16: CT slices of CFRP measured with different sample–detector distances and exposure times.

4. PROPAGATION-BASED IMAGING

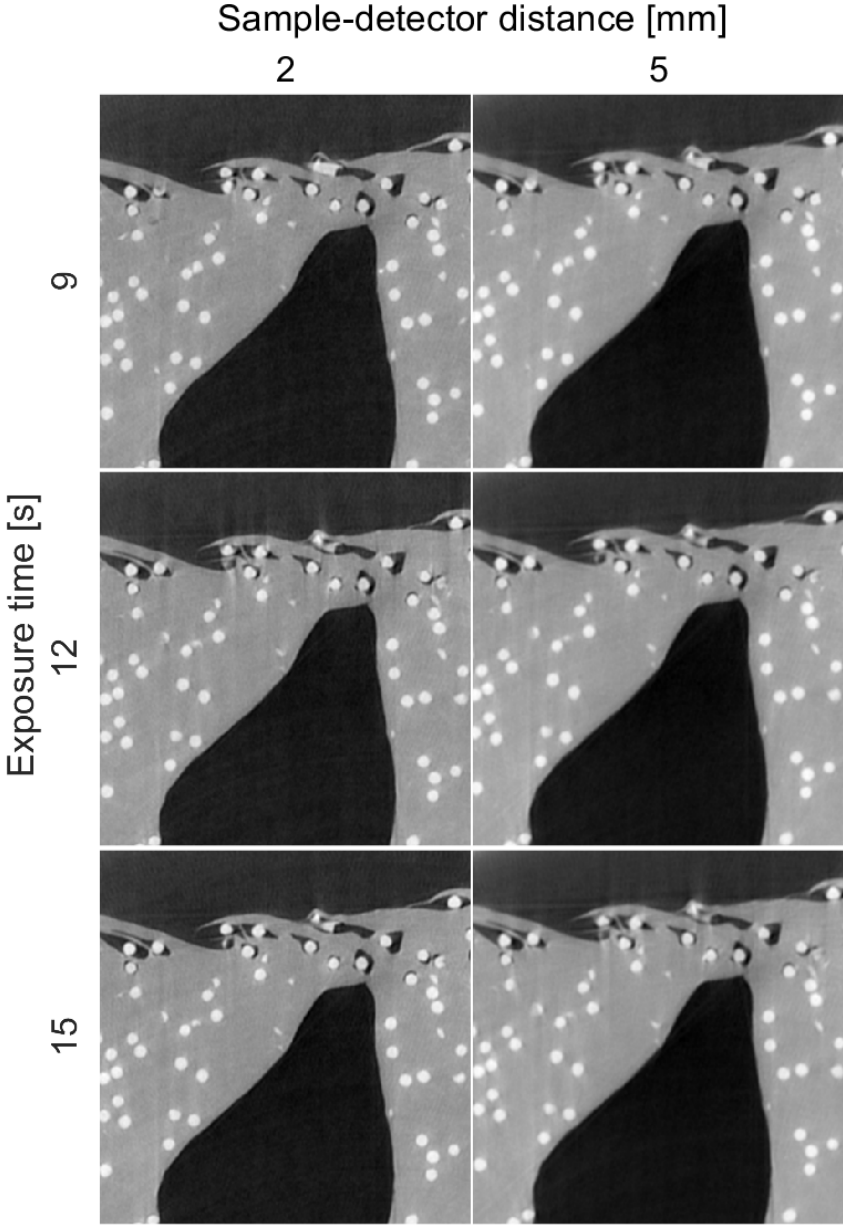


Figure 4.17: Phase retrieved CT slices of CFRP measured with different sample–detector distances and exposure times.

4.3. OPTIMISATION OF MEASUREMENT PARAMETERS FOR PBI
WITH NANO3DX

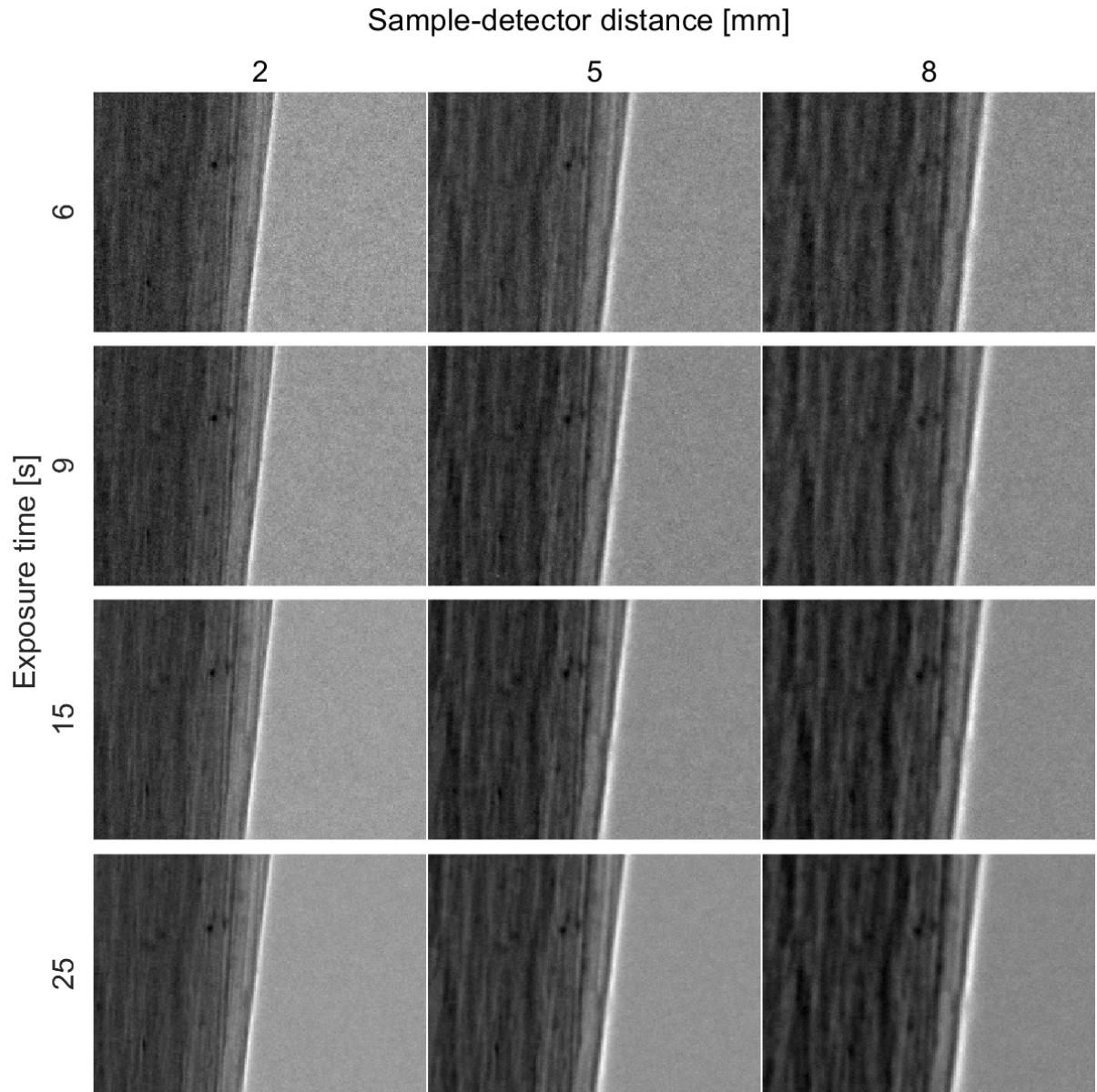


Figure 4.18: Details of projections of CFRP measured with different sample-detector distances and exposure times.

4. PROPAGATION-BASED IMAGING

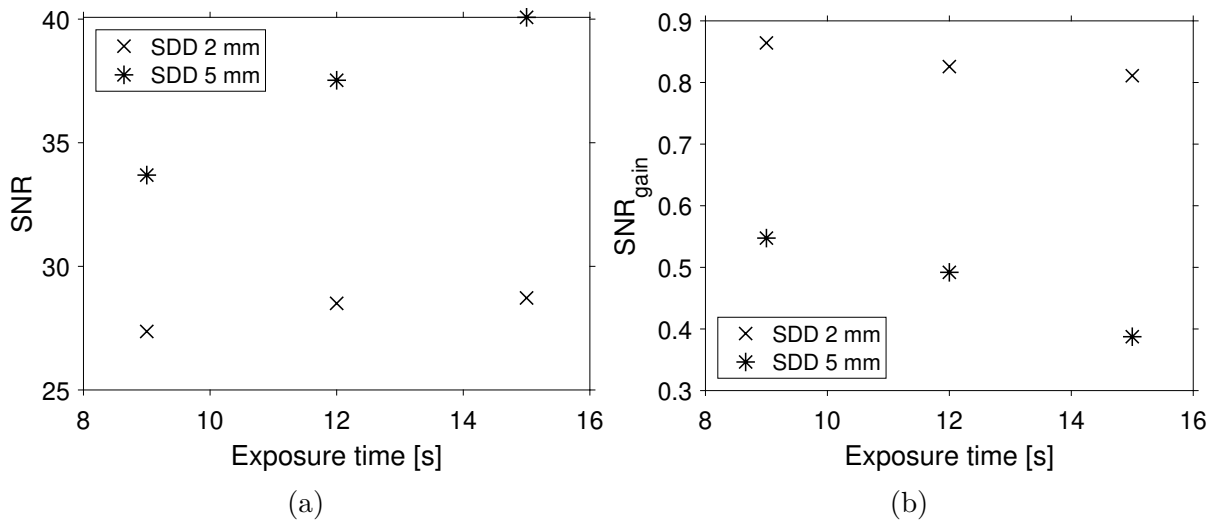


Figure 4.19: a) SNR and b) SNR_{gain} of CT slices of CFRP measured with different sample-detector distances and exposure times.

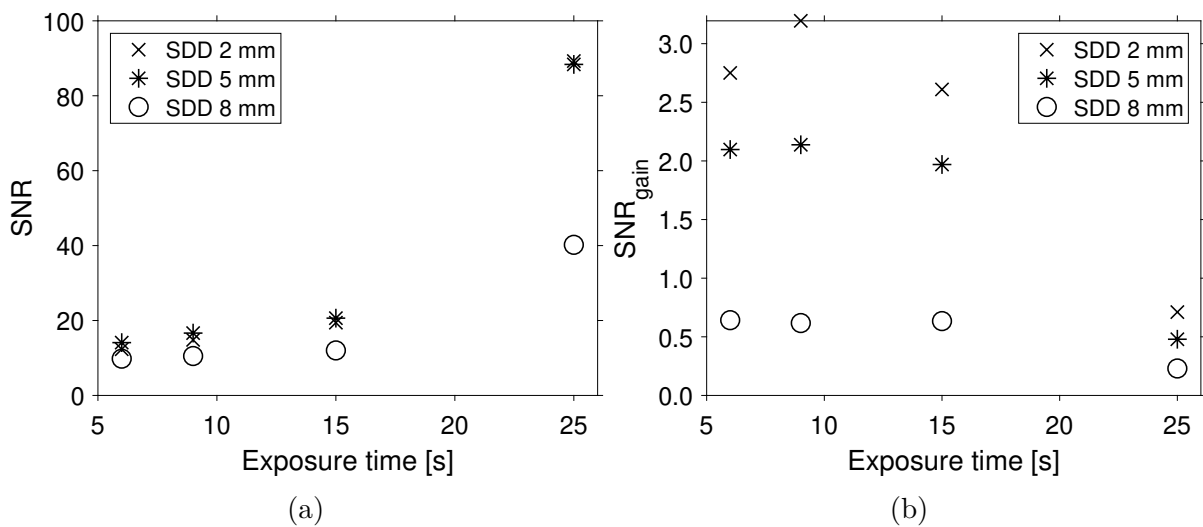


Figure 4.20: a) SNR and b) SNR_{gain} of projections of CFRP measured with different sample-detector distances and exposure times.

4.3. OPTIMISATION OF MEASUREMENT PARAMETERS FOR PBI WITH NANO3DX

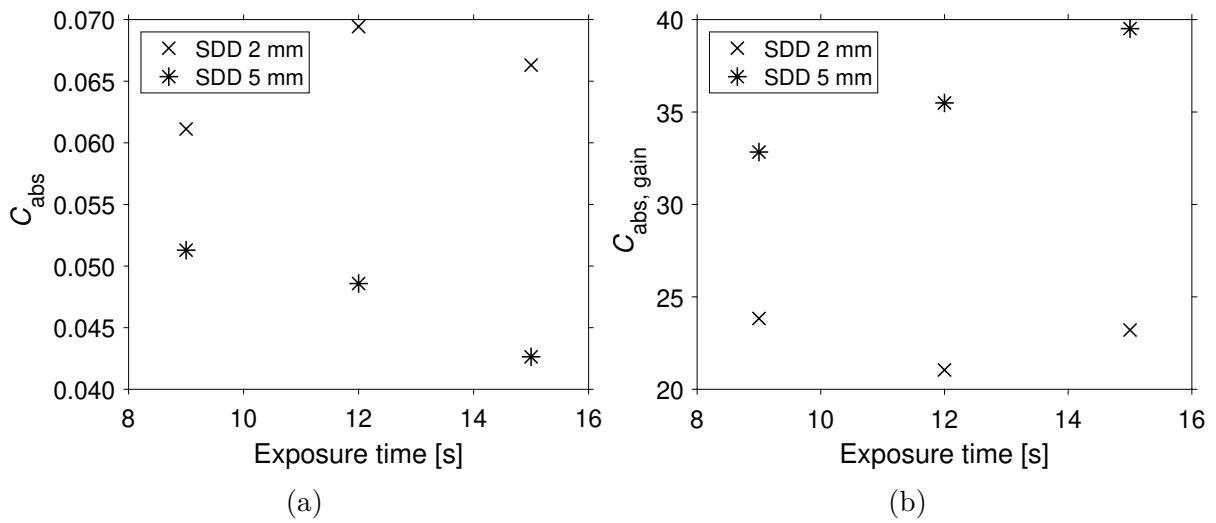


Figure 4.21: a) C_{ABS} and b) $C_{ABS, gain}$ of CT slices of CFRP measured with different sample-detector distances and exposure times.

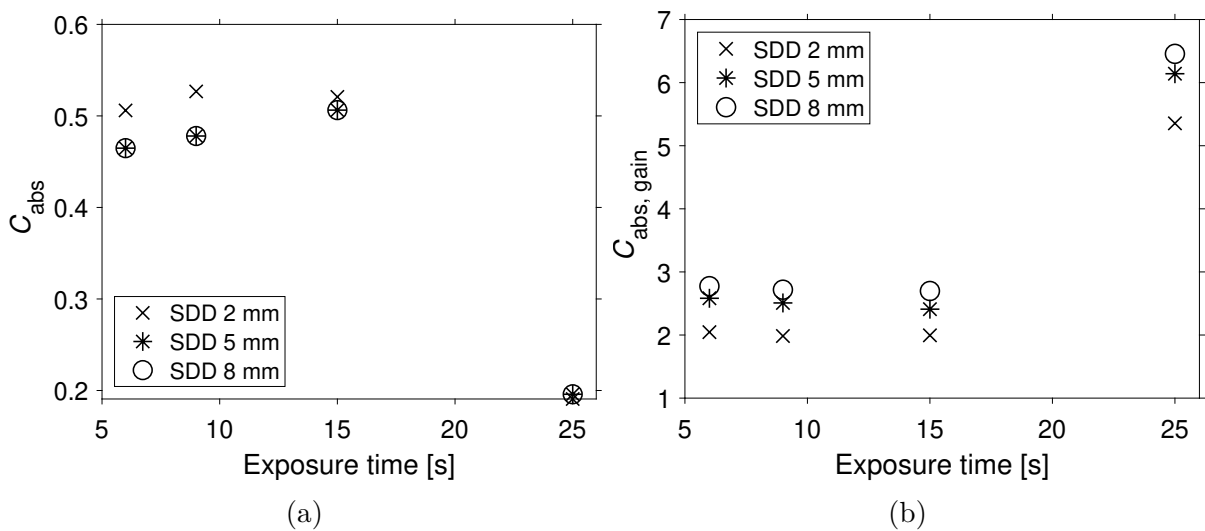


Figure 4.22: a) C_{ABS} and b) $C_{ABS, gain}$ of projections of CFRP measured with different sample-detector distances and exposure times.

4. PROPAGATION-BASED IMAGING

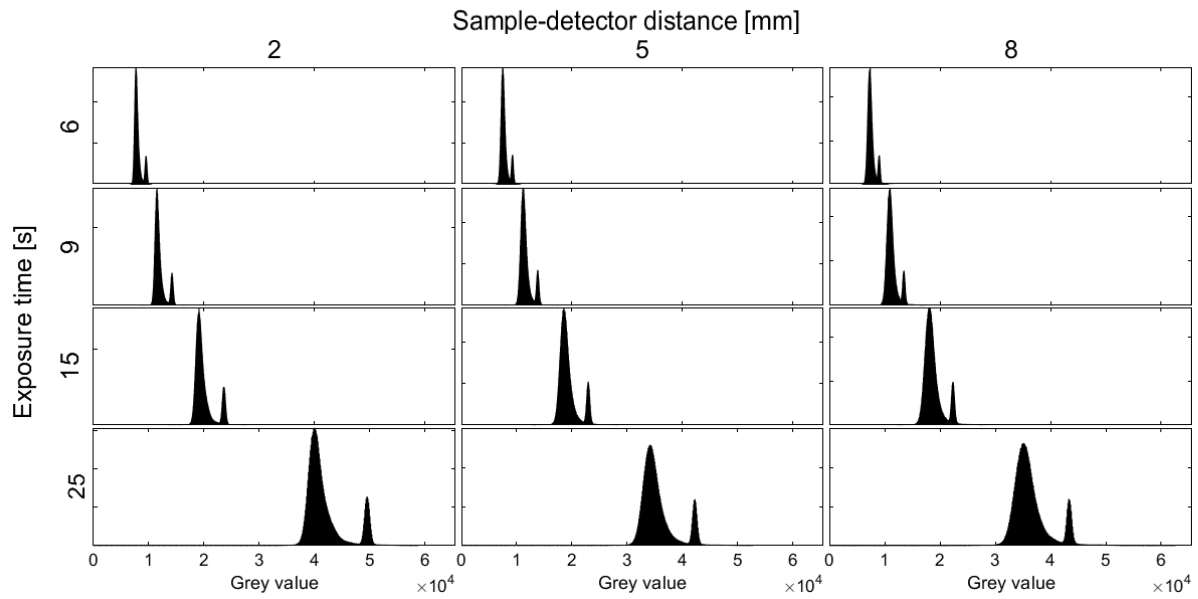


Figure 4.23: Non-normalised histograms of CT projections of CFRP measured with different sample–detector distances and exposure times.

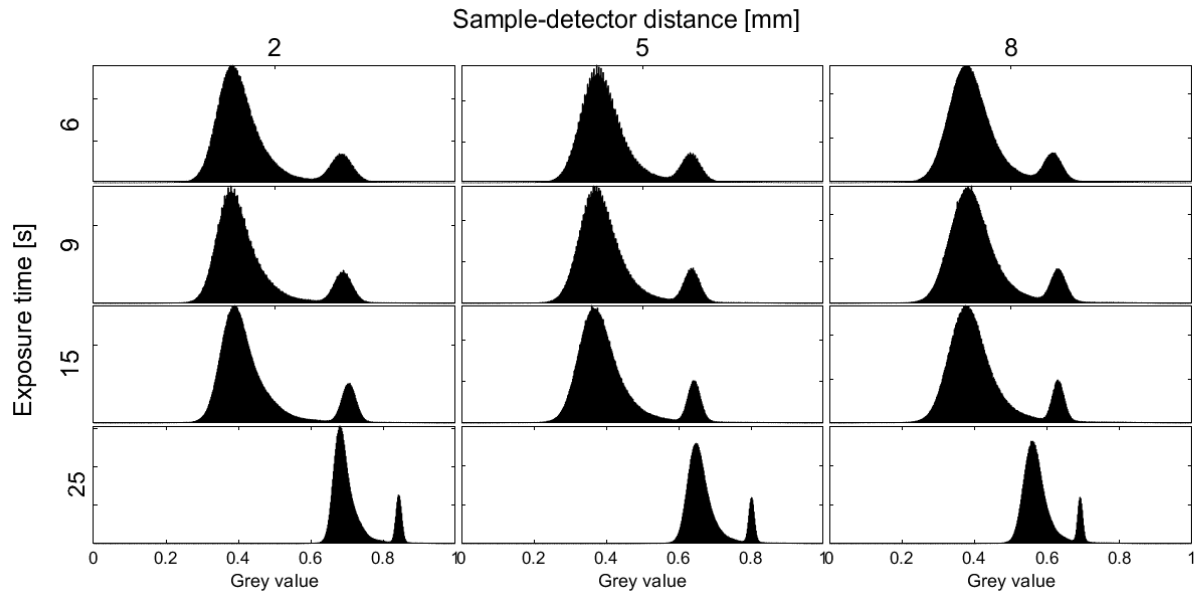


Figure 4.24: Normalised histograms of projections of CFRP measured with different sample–detector distances and exposure times.

5. Applications

In this chapter, selection of CT measurements of various kinds of biomaterials is reported. Specifications regarding applied CT methods and/or staining are emphasized.

5.1. Scaffolds with cells

In tissue engineering, scaffolds are used for healing of bone or cartilage defects. These porous, biodegradable structures are implanted into the damaged region. The surrounding tissue will grow through the scaffold, and it transforms into the tissue itself, serving as a reinforcement. This procedure is supposed to be less invasive for the patient since the number of surgical interventions should be reduced. Imaging of scaffolds by X-ray computed tomography brings 3D information about the success of creating scaffold structures and seeding them with cells. It can be used for verification of the scaffold's preparation and cell's behaviour within the scaffold, its adhesion and proliferation.

CT imaging of scaffolds with cells, distinguishing of cells from the scaffold and their characterization are still the unsolved issues. Many studies have been made in this field, both at synchrotrons ([113–120]) and with laboratory X-ray sources (Tab. 5.1). Several studies of cells in scaffolds imaging with different laboratory CT devices with different resolutions are presented in Tab. 5.1. There are various cases from both microCT and medCT categories. Some authors use staining for increased contrast of the cells and/or scaffold.

Here, two different types of CT studies are presented. Imaging of individual cells at very high resolution (Sec. 5.1.1) allows to study in detail the shape and contact area of a single cell. Using worse resolution, but a larger field of view (Sec. 5.1.2), one can observe 3D morphology of a region containing a lot of cells. It is possible to determine characteristics such as volume fraction, contact area, wall thickness, etc., which subsequently helps to understand behavior of the cells and their interaction with scaffold.

Publ.	CT device	LVS [μm]	Scaffold	Cell	Staining
[121]	Scanco micro-CT 40	6	hydroxyapatite	mouse cells	OsO ₄
[122]	Scanco micro-CT 40	8	polymer	murine osteoblast-like cells	OsO ₄
[123]	Scanco micro-CT 80	36	silk fibroin	mesenchymal stem cells	no
[124]	Caliper, Quantum FX	20	collagen	mesenchymal stem cells	no
[125]	not specified	16	PLDL polymer	stomal cells from rat	no
[126]	Skyscan 1072	not specified	gelatine	mesenchymal stem cells	no
[127]	Skyscan 1076	36	PGLC polymer	human mesenchymal stem cells (hDPSC)	no
[128]	Bruker Skyscan 1272	2.9	collagen	HT1080	barium sulphate
[129]	North Star Imaging, X-view X 50-CT	17	polydimethylsiloxane (PDMS)	fibroblasts	Os
[130]	Zeiss Xradia MicroXCT 400	0.91	poly(lactic acid) non-woven fiber mesh	mesenchymal stem cells	no
[131]	GE Phoenix NanoTom S	3.75	TiAl4V	human periosteum-derived cells (hPDCS)	PTA or Hexabrix
[132]	RIGAKU nano3DX	0.54	collagen	rabbit mesenchymal stem cells	OsO ₄
[133]	Zeiss Xradia Ultra-810	0.15	electrospun PLGA	human fibroblasts	no

Table 5.1: Overview of studies dealing with CT imaging of cells and scaffolds (LVS – linear voxel size).

5.1.1. High resolution: single cell

This feasibility study shows nCT imaging of an individual cell within a collagen scaffold. The measurement was made at the University of Jyväskylä at Erasmus stay in spring 2018. Phase retrieval is used to enhance the contrast of cell and its nucleus and scaffold.

Sample preparation and measurement

A collagen scaffold seeded with mesenchymal stem cells from human lipoaspirate cultivated for six days and stained with tannic acid and uranyl acetate (TaUA) was measured with Zeiss Xradia nanoXCT-100 described in Sec. 3.1. The sample was glued to a needle, and the very top of the sample was scanned. The CT machine was set in the absorption mode with a large field of view (LFoV). The binning 2 was used to reach the linear voxel size 130 nm. With 541 projections and exposure time of 10 s the scan lasted about 1.5 h. For larger scanning times (several days), the sample was damaged, probably due to a high X-ray dose. Paganin phase retrieval algorithm was applied to X-ray projections to enhance data quality.

Results

The TaUA staining was more selective for the scaffold than for the cell (Fig. 5.1a). However, the grey value distribution in the reconstructed data has Gaussian-like shape (Fig. 5.2), which makes segmentation of the scaffold and the cell difficult. As it was demonstrated before, application of the phase retrieval algorithm (Fig. 5.1b) led to data with increased contrast and different grey values distribution in histogram (Fig. 5.2). From phase-retrieved data, the cell and scaffold were segmented and visualised in 3D space (Fig. 5.3). Moreover, the nucleus of the cell is distinguishable in the CT slice (Fig. 5.1b).

Summary

This study shows the capability of the laboratory nCT device to image the cell within the scaffold. TaUA staining and phase contrast enhancement are used to create a visible contrast between both structures. Therefore it was possible to segment them and visualize in 3D. Such a procedure can be useful for imaging of soft materials, where structures with very similar X-ray absorption are to be imaged and analysed.

5. APPLICATIONS

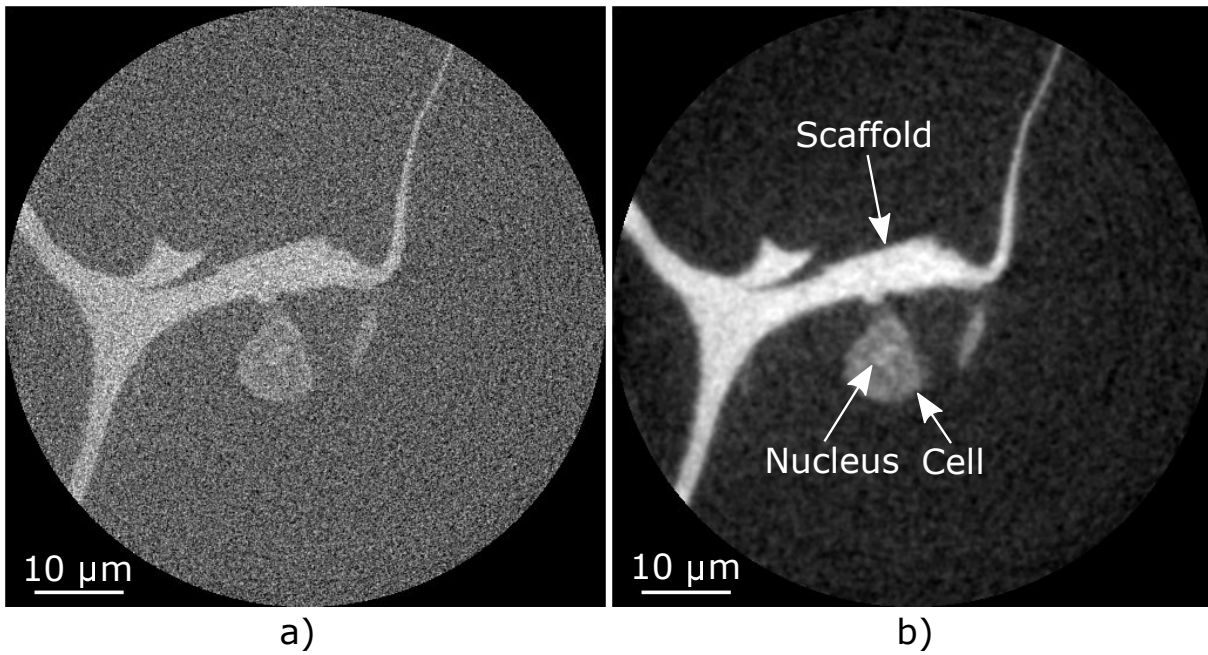


Figure 5.1: CT slice of the scaffold with a cell; a) original reconstruction (absorption contrast), b) phase retrieved CT slice (phase contrast).

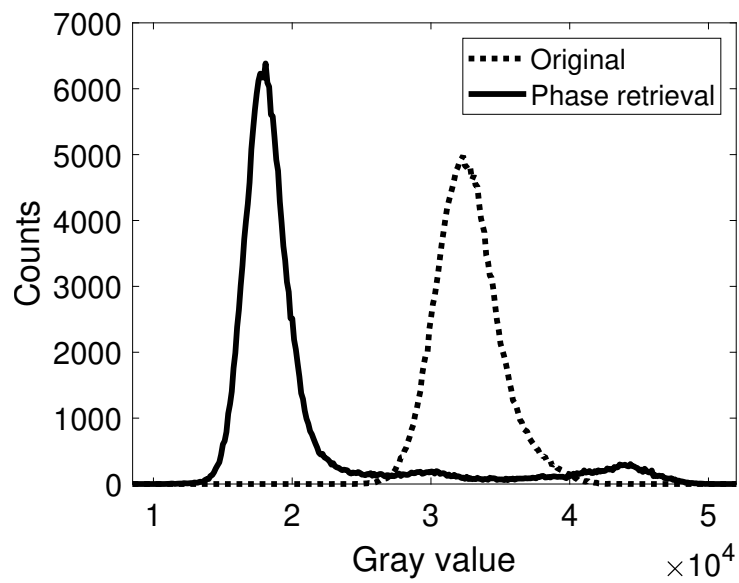


Figure 5.2: Histogram of CT slices of the scaffold with cell from Fig. 5.1.

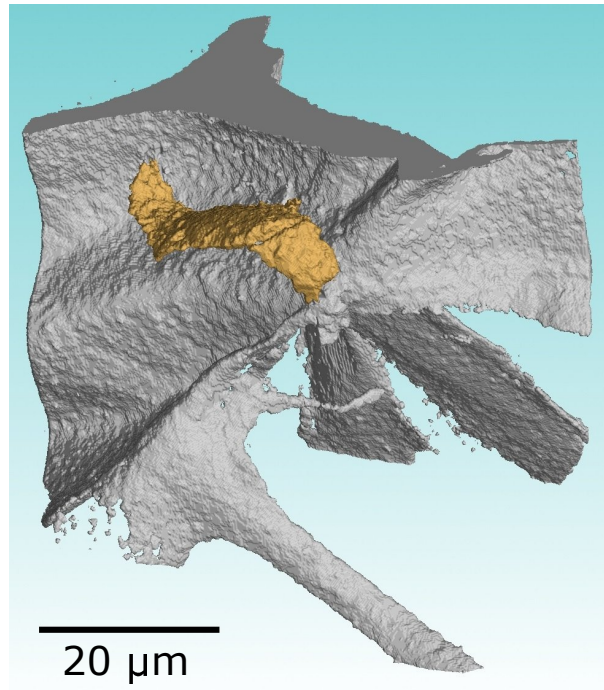


Figure 5.3: 3D render of the scaffold (grey) and cell (orange).

5.1.2. Large field of view: statistical evaluation

This study shows sub-micronCT analysis of scaffolds with cells with CT device nano3DX. In comparison to the previous study, the goal here is to evaluate a bigger region with higher amount of cells. The complete analysis of this sample was published in [132].

Sample preparation and measurement

Collagen porous scaffold seeded with rabbit mesenchymal stem cells (MSC) was stained with OsO_4 . The CT measurement was performed with the RIGAKU nano3DX device with a CCD camera with the following parameters: Cu target, field of view $0.7 \text{ mm} \times 0.9 \text{ mm}$, binning 2, linear voxel size $0.54 \mu\text{m}$, 800 projections, exposure time 10 s. The projections were filtered using nonlocal means denoising filter. Movement artefacts were reduced with a custom-developed movement correction technique based on the phase correlation. Paganin phase retrieval was used to enhance the contrast between cells and scaffold. More details in [132].

Results

Prior to the CT measurements, the scanning electron microscopy with an energy dispersive X-ray spectroscopy was used to verify the presence and positions of MSCs. Elemental distribution of osmium showed an increased concentration on the cell's surface. Phase retrieval further increased contrast between cells and scaffold in CT data, so it was possible to segment the cells based on different grey values.

The 3D render shows the distribution of cells throughout the scaffold (Fig. 5.4). By visual inspection, it is possible to observe the shape and distribution of cells. Knowledge of cell's proliferation is especially useful when samples with different cultivation

5. APPLICATIONS

times are compared. Wall thickness analysis gives information about overall the thickness of a scaffold (Fig. 5.5).

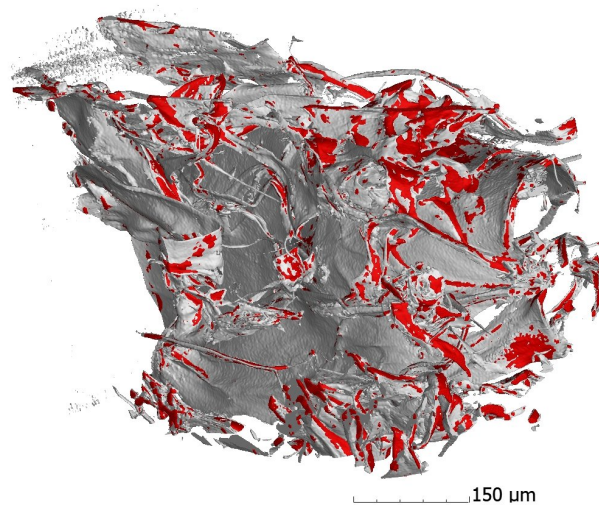


Figure 5.4: 3D rendering of a collagen scaffold with seeded MSC cells labeled in red colour.

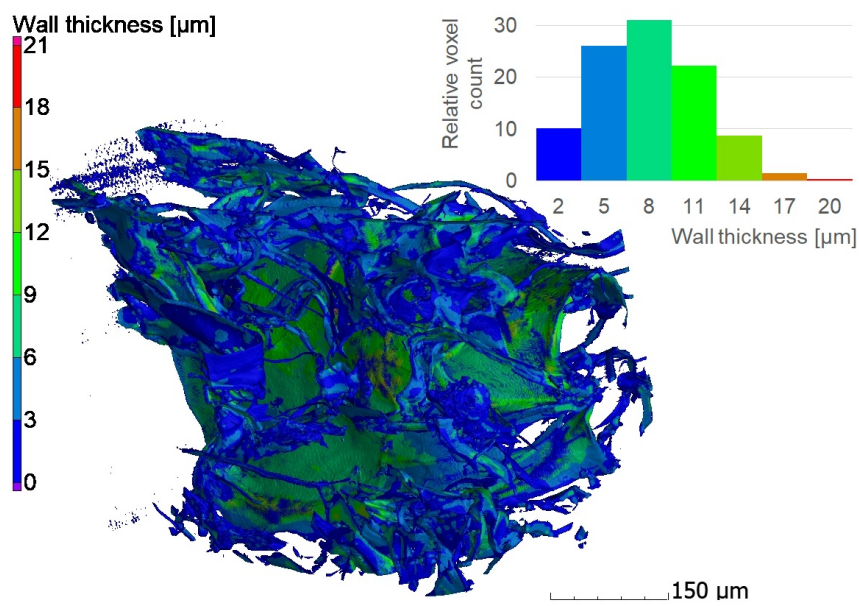


Figure 5.5: 3D rendering of a collagen scaffold with wall thickness analysis. The scaffold is colour-coded by the wall thickness.

5.2. Porosity of open foam structures

Porosity is one of the most significant properties when describing individual samples. It is defined as a ratio of air volume and total sample volume. There are many methods for the determination of porosity, either in 2D or 3D – Archimedes method, scanning electron microscopy, mercury porosimetry, gas pycnometry etc. [134] Among other techniques, X-ray computed tomography is nondestructive and 3D, but limited in resolution [135, 136]. The best method is individual for each application, and it is often advantageous to use more complementary techniques.

To obtain quantitative information of single, enclosed cavities (enclosed porosity, Fig. 5.6a) in CT data is a prevalent task in the industry. Each pore is a separate volume surrounded by the material. Information of interest includes a list of pores with their sizes, volumes and positions, and morphological information about their distribution within the bulk of the sample. In tissue engineering, the more common situation is when the pores are interconnected within the structure (open porosity, Fig. 5.6b). The structure itself is more like a network of thin walls rather than bulk filled with material. It is a case of many biomaterial applications like foams and scaffolds. In this case, the software first has to divide the pore space into single pores. Subsequently, additional information about pore space can be obtained such as distribution, quantification and statistics of the areas between the pores and the pore network.

To get quantitative information about open porosity in samples scanned with CT, different software offers various approaches. A comparison of different software for open porosity analysis of CT data was presented at the CEITEC PHD retreat II. conference [137], the poster is included in Appendix B. The analysis of this type of samples in VGStudio MAX was published in [138]. Both studies were performed on a sample of hydroxyapatite foam measured with GE phoenix v|tome|x L240 (Sec. 3.1).

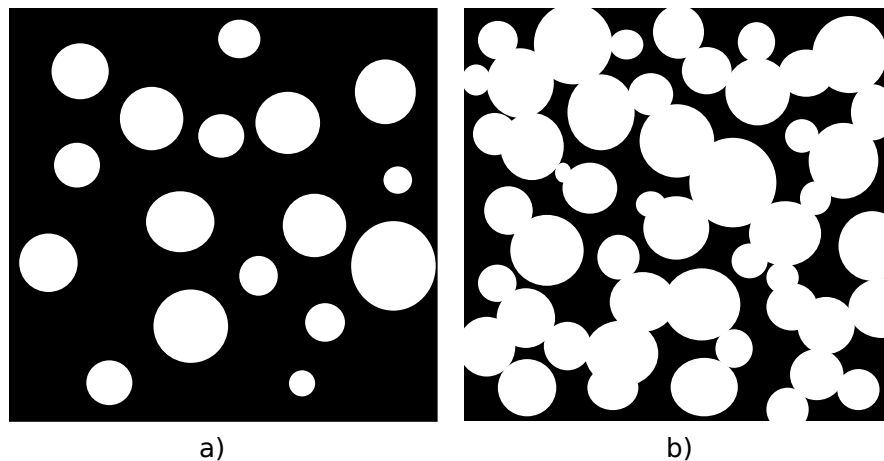


Figure 5.6: Schematic drawing of a) enclosed and b) open porosity. In enclosed porosity, each pore occurs separately. Open porosity is characterized by interconnected pores creating one pore network.

5.3. Correlation of CT data with 2D imaging techniques

All imaging methods have their advantages and disadvantages, and all offer examination from some point of view. For a complete description of a sample, it is often advantageous to combine them via some multi-disciplinary approach. For biological specimens, many authors combine CT measurements with optical microscopy images of histological sections [139, 140] or transmission electron microscopy [141]. In material science, and also tissue engineering, scanning electron microscopy is used [116].

CT can also be combined with other 3D methods. In medicine, CT is combined with positron emission tomography [142, 143], or with magnetic resonance imaging [144, 145] since those methods are more sensitive to different kinds of tissues and they may help with artefact removal. Serial sectioning by focused ion beam with elemental or chemical mapping by energy dispersive X-ray spectroscopy or electron backscatter diffraction is used to describe CT data qualitatively [94, 146, 147]. Large-scale CT images can be supplemented with CT images focused on some region of interest imaged with higher resolution [148].

In studies presented in this section, CT data do not give information about which grey values correspond to which element or material inside the sample. The contrast is based only on different properties of different parts of a sample in the X-ray region. 2D optical and electron microscopy are used as a reference for the interpretation of CT data. Moreover, in Sec. 5.3.1, a sample holder for easier correlation of SEM and CT data is presented.

5.3.1. nCT, SEM and LM of scaffolds

The collagen scaffold structure was observed using the nCT device RIGAKU nano3DX and the scanning electron microscope (SEM) Tescan MIRA3. As a supplementary method, light microscopy (LM) was used. Since all machines have different geometrical arrangements, a sample holder compatible with nCT and SEM was designed. To locate precisely the same regions of interest in all methods, a test of markers placed on the sample was performed.

The study was presented by the author of the thesis at XRM 2018 conference and published in [149], titled “Correlation of X-ray Computed Nanotomography and Scanning Electron Microscopy Imaging of Collagen Scaffolds”. A copy of the original article is included in Appendix B.

5.3.2. CT, 3D EDS analysis and LM of limestone

Although this experiment does not refer to a biomaterial, it is a good example of correlation of CT data with other methods. Combination of several methods on limestone sample helps with identification of materials within the sample. The study was published by the author of the thesis in [85], titled “Characterization of inner structure of limestone by X-ray computed sub-micron tomography”. A copy of the original article is included in Appendix B.

Abstract

“Limestones are fundamental industrial and building materials. Sparry calcite as a principal petrographic component of limestones can contain fluid inclusions. A certain amount of fluid inclusions directly influences decrepitation which plays an important role in decarbonisation processes.

In this paper, a limestone with a high content of fluid inclusions and carbon was investigated. Presence of chlorine and alcalic elements was confirmed with microthermometry, mineralogical and chemical analyses. X-ray computed tomography with sub-micron resolution (CT) was applied to obtain a 3D distribution of cavities. CT data were correlated with some light microscopy images and also with the same sample’s tomography data which were gathered using the 3D X-ray energy dispersive spectroscopy (3D EDS) by a scanning electron microscope equipped with a focused ion beam (FIB-SEM). The latter further determined dolomites and metals in the CT data of limestone.” [85]

5. APPLICATIONS

Conclusion

The topic of the thesis reflects the current need of scientists to have a 3D, nondestructive, high-resolution imaging method of investigation of soft samples to complement established 2D microscopy techniques. Although the CT was originally developed for clinical purpose, the straightforward application on smaller samples and with higher resolution does not reflect the small X-ray absorption of soft tissues and their inclination to movement. Therefore in many cases, special measurement protocols and methods or specific post-processing procedures have to be adapted to be able to fully exploit all advantages of X-ray computed tomography.

One of the challenges is that biomaterials often do not have enough contrast in X-ray region to be measured with sufficient quality by common absorption CT. In such cases, staining of samples or phase contrast imaging methods have to be used. The latter is the method widely studied and exploited in the thesis. Propagation-based method of phase contrast imaging with laboratory X-ray sources was studied on specific CT devices. A theoretical description of the machines helps to understand its capabilities of PBI and estimate its limitations. Several sets of experiments were performed to test various theoretical statements regarding phase contrast theory and geometrical arrangement. Application of phase retrieval on CT data was shown as a useful tool for enhancing data quality. A graphical user interface for implementing and testing of phase retrieval algorithms was designed.

To establish the CT technique as a standard examination tool, it has to be put within the framework of methods already commonly used in practice and the advantages have to be demonstrated on specific examples. Examples of image processing of CT data from various machines were shown, including morphology characteristics, volumetric analysis, and porosity analysis. Supporting 2D examination methods may be used as a qualitative methods to determine the sample's composition, whereas CT observes the whole sample quantitatively. To demonstrate that such a correlation is possible and advantageous, two case-studies presented a combination of CT, light microscopy, scanning electron microscopy and 3D energy dispersive X-ray spectroscopy. A sample holder which fits both into CT and SEM machines was designed to help with a mutual correlation of data.

The particular contribution of this work is the extension of expertise in phase contrast imaging within the Laboratory of X-ray micro and nano computed tomography at CEITEC BUT. Implementation of this method on specific topics from material research extends the possibilities of characterisation of materials, primarily in the field of soft materials. In general, this thesis contributes to the establishment of an X-ray computed tomography technique as a common tool for 3D imaging and analysis of biomaterials. The most important results presented in this work are published by the author in impacted journals [37, 85, 149] and international conferences [137, 150] so the scientific community can benefit from the findings.

CONCLUSION

References

- [1] KALASOVÁ, D. *Utilization of phase contrast in X-ray computed tomography*. 2016. Master's thesis. Brno University of Technology.
- [2] POLUDNIOWSKI, G., G. LANDRY, F. DEBLOIS, P. M. EVANS and F. VERHAEGEN. SpekCalc : a program to calculate photon spectra from tungsten anode x-ray tubes. *Physics in Medicine and Biology*. 2009, vol. 54, no. 19. ISSN 0031-9155. Available from: doi:10.1088/0031-9155/54/19/N01.
- [3] HSIEH, J. *Computed tomography: principles, design, artifacts, and recent advances*. 2nd ed. Wiley Interscience ; SPIE Press, 2015. ISBN 9781628418255. Available from: doi:10.1117/3.2197756.
- [4] BUSHBERG, J. T. *The essential physics of medical imaging*. Lippincott Williams and Wilkins, 2002. ISBN 978-0-683-30118-2.
- [5] JAMES, R. W. *The optical principles of the diffraction of X-rays*. 2nd ed. G. Bell and sons LTD, 1962.
- [6] WILLMOTT, P. *An Introduction to Synchrotron Radiation*. Chichester, UK: John Wiley and Sons, Ltd, 2011. ISBN 9781119970958. Available from: doi:10.1002/9781119970958.
- [7] X-ray tomography in material science. 2000, vol. 6, no. 6, pp. 1–209.
- [8] MAYO, S. C., P. R. MILLER, S. W. WILKINS, T. J. DAVIS, D. GAO, T. E. GUREYEV, D. PAGANIN, D. J. PARRY, A. POGANY and A. W. STEVENSON. Quantitative X-ray projection microscopy: phase-contrast and multi-spectral imaging. *Journal of Microscopy*. 2002, vol. 207, no. 2, pp. 79–96. ISSN 00222720. Available from: doi:10.1046/j.1365-2818.2002.01046.x.
- [9] GRANGEAT, P. *Tomography*. ISTE [u.a.], 2009. ISBN 978-1-84821-099-8.
- [10] KAK, A. C. and M. SLANEY. *Principles of computerized tomographic imaging*. IEEE Press, 1988. ISBN 978-0-87942-198-4.
- [11] POULARIKAS, A. D. *The handbook of formulas and tables for signal processing*. CRC Press ; Springer : IEEE Press, 1999. The electrical engineering handbook series. ISBN 978-0-8493-8579-7.
- [12] HENKE, B., E. GULLIKSON and J. DAVIS. X-Ray Interactions: Photoabsorption, Scattering, Transmission, and Reflection at $E = 50\text{-}30,000$ eV, $Z = 1\text{-}92$. *Atomic Data and Nuclear Data Tables* [online]. 1993, vol. 54, no. 2, pp. 181–342. ISSN 0092640X. Available from: doi:10.1006/adnd.1993.1013. Available from: http://henke.lbl.gov/optical_constants/.

REFERENCES

- [13] THOMPSON, A. and D. VAUGHAN. *X-ray data booklet* [online]. Center for X-ray optics and advanced light source, Lawrence Berkeley National Laboratory, 2009. Available from: <http://xdb.lbl.gov>.
- [14] CHANTLER, C. T., K. OLSEN, R. A. DRAGOSET, J. CHANG, A. R. KISHORE, S. A. KOTOCHIGOVA and D. S. ZUCKER. *Detailed Tabulation of Atomic Form Factors, Photoelectric Absorption and Scattering Cross Section, and Mass Attenuation Coefficients for $Z = 1-92$ from $E = 1-10$ eV to $E = 0.4-1.0$ MeV* [online]. 2005. Available from: doi:10.18434/T4HS32. Available from: <http://www.nist.gov/pml/data/ffast/index.cfm>.
- [15] HUBBEL, J. H. and S. M. SELTZER. *Tables of X-Ray Mass Attenuation Coefficients and Mass Energy-Absorption Coefficients from 1 keV to 20 MeV for Elements $Z = 1$ to 92 and 48 Additional Substances of Dosimetric Interest* [online]. 2004. Available from: doi:10.18434/T4D01F. Available from: <https://www.nist.gov/pml/x-ray-mass-attenuation-coefficients>.
- [16] MERRIT, E. A. *X-ray absorption edges* [online]. 2010. Available from: http://skuld.bmsc.washington.edu/scatter/AS_periodic.html.
- [17] BANDYOPADHYAY, P. and C. U. SEGRE. *Mucal Periodic Table* [online]. Available from: <http://www.csrri.iit.edu/periodic-table.html>.
- [18] SÁNCHEZ DEL RÍO, M. and R. J. DEJUS. XOP v2.4: recent developments of the x-ray optics software toolkit. In: 2011, pp. 814115. Available from: doi:10.1117/12.893911.
- [19] BALINT, R., T. LOWE and T. SHEARER. Optimal Contrast Agent Staining of Ligaments and Tendons for X-Ray Computed Tomography. *PLOS ONE*. 2016, vol. 11, no. 4. ISSN 1932-6203. Available from: doi:10.1371/journal.pone.0153552.
- [20] METSCHER, B. D. MicroCT for developmental biology: A versatile tool for high-contrast 3D imaging at histological resolutions. *Developmental Dynamics*. 2009, vol. 6, no. 6, pp. 632–640. ISSN 10588388. Available from: doi:10.1002/dvdy.21857.
- [21] SILVA, J. M. d. S. e., I. ZANETTE, P. B. NOËL, M. B. CARDOSO, M. A. KIMM and F. PFEIFFER. Three-dimensional non-destructive soft-tissue visualization with X-ray staining micro-tomography. *Scientific Reports*. 2015, vol. 5, no. 1, pp. 14088. ISSN 20452322. Available from: doi:10.1038/srep14088.
- [22] BRERETON, N. Sample Preparation for X-ray Micro-computed Tomography of Woody Plant Material and Associated Xylem Visualisation Techniques. *BIOPROTOCOL*. 2016, vol. 6, no. 6. ISSN 2331-8325. Available from: doi:10.21769/bioprotoc.1767.
- [23] GUTIÉRREZ, Y., D. OTT, M. TÖPPERWIEN, T. SALDITT and C. SCHERBER. X-ray computed tomography and its potential in ecological research: A review of studies and optimization of specimen preparation. *Ecology and Evolution*. 2018, vol. 8, no. 15, pp. 7717–7732. ISSN 20457758. Available from: doi:10.1002/ece3.4149.
- [24] LI, Z., J. A. CLARKE, R. A. KETCHAM, M. W. COLBERT and F. YAN. An investigation of the efficacy and mechanism of contrast-enhanced X-ray Computed Tomography utilizing iodine for large specimens through experimental and simulation approaches. *BMC Physiology*. 2015, vol. 6, no. 6. ISSN 14726793. Available from: doi:10.1186/s12899-015-0019-3.

- [25] METSCHER, B. D. Micro CT for comparative morphology: Simple staining methods allow high-contrast 3D imaging of diverse non-mineralized animal tissues. *BMC Physiology*. 2009, vol. 9, no. 1, pp. 11. ISSN 14726793. Available from: doi:10.1186/1472-6793-9-11.
- [26] ZHOU, S.-A. and A. BRAHME. Development of phase-contrast X-ray imaging techniques and potential medical applications. *Physica Medica*. 2008, vol. 24, no. 3, pp. 129–148. ISSN 11201797. Available from: doi:10.1016/j.ejmp.2008.05.006.
- [27] MOMOSE, A., T. TAKEDA, Y. ITAI, A. YONEYAMA and K. HIRANO. Phase-contrast tomographic imaging using an X-ray interferometer. *Journal of Synchrotron Radiation*. 1998, vol. 5, no. 3, pp. 309–314. ISSN 09090495. Available from: doi:10.1107/S0909049597014271.
- [28] YONEYAMA, A., A. MOMOSE, I. KOYAMA, E. SEYA, T. TAKEDA, Y. ITAI, K. HIRANO and K. HYODO. Large-area phase-contrast X-ray imaging using a two-crystal X-ray interferometer. *Journal of Synchrotron Radiation*. 2002, vol. 9, no. 5, pp. 277–281. ISSN 09090495. Available from: doi:10.1107/S090904950201350X.
- [29] CHAPMAN, D., W. THOMLINSON, R. E. JOHNSTON, D. WASHBURN, E. PISANO, N. GMÜR, Z. ZHONG, R. MENK, F. ARFELLI and D. SAYERS. Diffraction enhanced x-ray imaging. *Physics in Medicine and Biology*. 1997, vol. 42, no. 11, pp. 2015–2025. ISSN 0031-9155. Available from: doi:10.1088/0031-9155/42/11/001.
- [30] DAVIS, T. J., D. GAO, T. E. GUREYEV, A. W. STEVENSON and S. W. WILKINS. Phase-contrast imaging of weakly absorbing materials using hard X-rays. *Nature*. 1995, vol. 373, no. 6515, pp. 595–598. ISSN 00280836. Available from: doi:10.1038/373595a0.
- [31] PFEIFFER, F., M. BECH, O. BUNK, P. KRAFT, E. F. EIKENBERRY, C. BRÖNNIMANN, C. GRÜNZWEIG and C. DAVID. Hard-X-ray dark-field imaging using a grating interferometer. *Nature Materials*. 2008, vol. 7, no. 2, pp. 134–137. ISSN 14761122. Available from: doi:10.1038/nmat2096.
- [32] PFEIFFER, F., T. WEITKAMP, O. BUNK and C. DAVID. Phase retrieval and differential phase-contrast imaging with low-brilliance X-ray sources. *Nature Physics*. 2006, vol. 2, no. 4, pp. 258–261. ISSN 17452473. Available from: doi:10.1038/nphys265.
- [33] STUTMAN, D. and M. FINKENTHAL. Glancing angle Talbot-Lau grating interferometers for phase contrast imaging at high x-ray energy. *Applied Physics Letters*. 2012, vol. 101, no. 9, pp. 091108. ISSN 00036951. Available from: doi:10.1063/1.4748882.
- [34] TANAKA, J., M. NAGASHIMA, K. KIDO, Y. HOSHINO, J. KIYOHARA, C. MAKIFUCHI, S. NISHINO, S. NAGATSUKA and A. MOMOSE. Cadaveric and in vivo human joint imaging based on differential phase contrast by X-ray Talbot-Lau interferometry. *Zeitschrift für Medizinische Physik*. 2013, vol. 23, no. 3, pp. 222–227. ISSN 09393889. Available from: doi:10.1016/j.zemedi.2012.11.004.
- [35] WANG, Z., K. GAO, P. ZHU, Q. YUAN, W. HUANG, K. ZHANG, Y. HONG, X. GE and Z. WU. Grating-based X-ray phase contrast imaging using polychromatic laboratory sources. *Journal of Electron Spectroscopy and Related Phenomena*. 2011, vol. 184, no. 3-6, pp. 342–345. ISSN 03682048. Available from: doi:10.1016/j.elspec.2010.12.009.

REFERENCES

- [36] WANG, Z., P. ZHU, W. HUANG, Q. YUAN, X. LIU, K. ZHANG, Y. HONG, H. ZHANG, X. GE, K. GAO and Z. WU. Quantitative coherence analysis with an X-ray Talbot-Lau interferometer. *Analytical and Bioanalytical Chemistry*. 2010, vol. 397, no. 6, pp. 2091–2094. ISSN 16182642. Available from: doi:10.1007/s00216-010-3632-9.
- [37] KALASOVÁ, D., T. ZIKMUND, L. PÍNA, Y. TAKEDA, M. HORVÁTH, K. OMOTE and J. KAISER. Characterization of a laboratory-based X-ray computed nanotomography system for propagation-based method of phase contrast imaging. *IEEE Transactions on Instrumentation and Measurement*. 2019. Available from: doi:10.1109/TIM.2019.2910338.
- [38] KUMAR, A. S., P. MANDAL, Y. ZHANG and S. LITSTER. Image segmentation of nanoscale Zernike phase contrast X-ray computed tomography images. *Journal of Applied Physics*. 2015, vol. 117, no. 18, pp. 183102. ISSN 10897550. Available from: doi:10.1063/1.4919835.
- [39] TKACHUK, A., F. DUEWER, H. CUI, M. FESER, S. WANG and W. YUN. X-ray computed tomography in Zernike phase contrast mode at 8 keV with 50-nm resolution using Cu rotating anode X-ray source. *Zeitschrift für Kristallographie*. 2007, vol. 222, no. 11, pp. 650–655. ISSN 00442968. Available from: doi:10.1524/zkri.2007.222.11.650.
- [40] WU, X. and H. LIU. Clarification of aspects in in-line phase-sensitive x-ray imaging. *Medical Physics*. 2007, vol. 34, no. 2, pp. 737–743. ISSN 00942405. Available from: doi:10.1118/1.2431475.
- [41] MOHAMMADI, S., E. LARSSON, F. ALVES, S. DAL MONEGO, S. BIFFI, C. GARROVO, A. LORENZON, G. TROMBA and C. DULLIN. Quantitative evaluation of a single-distance phase-retrieval method applied on in-line phase-contrast images of a mouse lung. *Journal of Synchrotron Radiation*. 2014, vol. 21, no. 4, pp. 784–789. ISSN 16005775. Available from: doi:10.1107/S1600577514009333.
- [42] BETZ, O., U. WEGST, M. HEETHOFF, W.-K. LEE, P. CLOETENS, L. HELFEN and D. WEIDE. Imaging applications of synchrotron X-ray phase-contrast microtomography in biological morphology and biomaterials science. I. General aspects of the technique and its advantages in the analysis of millimetre-sized arthropod structure. *Journal of Microscopy*. 2007, vol. 227, no. 1, pp. 51–71. ISSN 0022-2720. Available from: doi:10.1111/j.1365-2818.2007.01785.x.
- [43] JI, Y., X. LIN, Z. WU, M. LI, G.-Y. YANG, P. MIAO and B. XIE. Synchrotron Radiation X-Ray Phase-Contrast Tomography Visualizes Microvasculature Changes in Mice Brains after Ischemic Injury. *Neural Plasticity*. 2016, vol. 2016, pp. 1–8. ISSN 2090-5904. Available from: doi:10.1155/2016/3258494.
- [44] SOCHA, J. J., M. W. WESTNEAT, J. F. HARRISON, J. S. WATERS and W. K. LEE. Real-time phase-contrast x-ray imaging: A new technique for the study of animal form and function. *BMC Biology*. 2007, vol. 5, no. 1, pp. 6. ISSN 17417007. Available from: doi:10.1186/1741-7007-5-6.
- [45] COSMI, F., A. BERNASCONI and N. SODINI. Phase contrast micro-tomography and morphological analysis of a short carbon fibre reinforced polyamide. *Composites Science and Technology*. 2011, vol. 71, no. 1, pp. 23–30. ISSN 02663538. Available from: doi:10.1016/j.compscitech.2010.09.016.

- [46] GARCEA, S., Y. WANG and P. WITHERS. X-ray computed tomography of polymer composites. *Composites Science and Technology*. 2018, vol. 156, no. 6, pp. 305–319. ISSN 02663538. Available from: doi:10.1016/j.compscitech.2017.10.023.
- [47] YU, B., R. S. BRADLEY, C. SOUTIS and P. J. WITHERS. A comparison of different approaches for imaging cracks in composites by X-ray microtomography. *Philosophical Transactions of the Royal Society A: Mathematical, Physical and Engineering Sciences*. 2016, vol. 374, no. 2071, pp. 20160037. ISSN 1364503X. Available from: doi:10.1098/rsta.2016.0037.
- [48] KASTNER, J., B. PLANK and G. REQUENA. Non-destructive characterisation of polymers and Al-alloys by polychromatic cone-beam phase contrast tomography. *Materials Characterization*. 2012, vol. 64, pp. 79–87. ISSN 10445803. Available from: doi:10.1016/j.matchar.2011.12.004.
- [49] MAYO, S. C., A. W. STEVENSON and S. W. WILKINS. In-Line Phase-Contrast X-ray Imaging and Tomography for Materials Science. *Materials*. 2012, vol. 5, no. 12, pp. 937–965. ISSN 19961944. Available from: doi:10.3390/ma5050937.
- [50] MAYO, S., A. STEVENSON, J. MARDEL, S. MOOKHOEK, S. WILKINS, S. MEURE, T. HUGHES and D. C. GAO. X-Ray Phase-Contrast Tomography for Quantitative Characterisation of Self-Healing Polymers. *Materials Science Forum*. 2010, vol. 654-656, pp. 2322–2325. ISSN 16629752. Available from: doi:10.4028/www.scientific.net/msf.654-656.2322.
- [51] KRENKEL, M., M. TÖPPERWIEN, C. DULLIN, F. ALVES and T. SALDITT. Propagation-based phase-contrast tomography for high-resolution lung imaging with laboratory sources. *AIP Advances*. 2016, vol. 6, no. 3, pp. 35007. ISSN 21583226. Available from: doi:10.1063/1.4943898.
- [52] LAPERLE, C. M., T. J. HAMILTON, P. WINTERMEYER, E. J. WALKER, D. SHI, M. A. ANASTASIO, Z. DERDAK, J. R. WANDS, G. DIEBOLD and C. ROSE-PETRUCK. Low density contrast agents for x-ray phase contrast imaging: The use of ambient air for x-ray angiography of excised murine liver tissue. *Physics in Medicine and Biology*. 2008, vol. 53, no. 23, pp. 6911–6923. ISSN 00319155. Available from: doi:10.1088/0031-9155/53/23/017.
- [53] BARTELS, M., V. H. HERNANDEZ, M. KRENKEL, T. MOSER and T. SALDITT. Phase contrast tomography of the mouse cochlea at microfocus x-ray sources. *Applied Physics Letters*. 2013, vol. 103, no. 8, pp. 83703. ISSN 00036951. Available from: doi:10.1063/1.4818737.
- [54] KASHYAP, Y. S., P. S. YADAV, T. ROY, P. S. SARKAR, M. SHUKLA and A. SINHA. Laboratory-based X-ray phase-contrast imaging technique for material and medical science applications. *Applied Radiation and Isotopes*. 2008, vol. 66, no. 8, pp. 1083–1090. ISSN 09698043. Available from: doi:10.1016/j.apradiso.2007.12.008.
- [55] ARHATARI, B. D. and A. G. PEELE. Optimisation of phase imaging geometry. *Optics Express*. 2010, vol. 18, no. 23, pp. 23727. ISSN 10944087. Available from: doi:10.1364/oe.18.023727.
- [56] BALLE, A., S. ZABLER, T. EBENSPERGER, C. FELLA and R. HANKE. Propagator based formalism for optimizing in-line phase contrast imaging in laboratory X-ray setups. *Review of Scientific Instruments*. 2016, vol. 87, no. 9, pp. 093707. ISSN 0034-6748. Available from: doi:10.1063/1.4962713.

REFERENCES

- [57] BIDOLA, P. M., I. ZANETTE, K. ACHTERHOLD, C. HOLZNER and F. PFEIFFER. Optimization of propagation-based phase-contrast imaging at a laboratory setup. *Optics Express*. 2015, vol. 23, no. 23, pp. 30000. ISSN 1094-4087. Available from: doi:10.1364/OE.23.030000.
- [58] GUREYEV, T. E., Y. I. NESTERETS, A. W. STEVENSON, P. R. MILLER, A. POGANY and S. W. WILKINS. Some simple rules for contrast, signal-to-noise and resolution in in-line x-ray phase-contrast imaging. *Optics Express*. 2008, vol. 16, no. 5, pp. 3223. ISSN 1094-4087. Available from: doi:10.1364/OE.16.003223.
- [59] NESTERETS, Y. I., S. W. WILKINS, T. E. GUREYEV, A. POGANY and A. W. STEVENSON. On the optimization of experimental parameters for x-ray in-line phase-contrast imaging. *Review of Scientific Instruments*. 2005, vol. 76, no. 9. Available from: doi:10.1063/1.2038107.
- [60] NESTERETS, Y. I., T. E. GUREYEV and M. R. DIMMOCK. Optimisation of a propagation-based x-ray phase-contrast micro-CT system. *Journal of Physics D: Applied Physics*. 2018, vol. 51, no. 11, pp. 115402. ISSN 00223727. Available from: doi:10.1088/1361-6463/aaacee.
- [61] WILKINS, S. W., T. E. GUREYEV, D. GAO, A. POGANY and A. W. STEVENSON. Phase-contrast imaging using polychromatic hard X-rays. *Nature*. 1996, vol. 384.
- [62] PAGANIN, D. *Coherent X-Ray Optics*. Oxford University Press, 2006. Available from: doi:10.1093/acprof:oso/9780198567288.001.0001.
- [63] MAYO, S., T. DAVIS, T. GUREYEV, P. MILLER, D. PAGANIN, A. POGANY, A. STEVENSON and S. WILKINS. X-ray phase-contrast microscopy and microtomography. *Optics Express*. 2003, vol. 11, no. 19. ISSN 1094-4087. Available from: doi:10.1364/OE.11.002289.
- [64] POGANY, A., D. GAO and S. W. WILKINS. Contrast and resolution in imaging with a microfocus x-ray source. *Review of Scientific Instruments*. 1997, vol. 68, no. 7. ISSN 00346748. Available from: doi:10.1063/1.1148194.
- [65] WU, X., H. LIU and A. YAN. Phase-contrast X-ray tomography: Contrast mechanism and roles of phase retrieval. *European Journal of Radiology*. 2008, vol. 68, no. 3 SUPPL. Pp. S8–S12. ISSN 0720048X. Available from: doi:10.1016/j.ejrad.2008.04.027.
- [66] OUANDJI, F., E. POTTER, W. R. CHEN and H. LIU. Impact of focal spot size on the spatial resolution of a digital x-ray imaging system for small-animal studies. In: *Biomedical Diagnostic, Guidance, and Surgical-Assist Systems IV*. 2002, pp. 109–116. Available from: doi:10.1117/12.466639.
- [67] MENG, F., H. LIU and X. WU. An iterative phase retrieval algorithm for in-line x-ray phase imaging. *Optics Express*. 2007, vol. 15, no. 13, pp. 8383. ISSN 10944087. Available from: doi:10.1364/OE.15.008383.
- [68] YAN, A., X. WU and H. LIU. An attenuation-partition based iterative phase retrieval algorithm for in-line phase-contrast imaging. *Optics Express*. 2008, vol. 16, no. 17, pp. 13330. ISSN 10944087. Available from: doi:10.1364/OE.16.013330.
- [69] WEITKAMP, T., D. HAAS, D. WEGRZYNEK and A. RACK. ANKPhase : software for single-distance phase retrieval from inline X-ray phase-contrast radiographs. *Journal of Synchrotron Radiation*. 2011, vol. 18, no. 4, pp. 617–629. ISSN 09090495. Available from: doi:10.1107/S0909049511002895.

- [70] BURVALL, A., U. LUNDSTRÖM, P. A. C. TAKMAN, D. H. LARSSON and H. M. HERTZ. Phase retrieval in X-ray phase-contrast imaging suitable for tomography. *Optics Express*. 2011, vol. 19, no. 11, pp. 10359. ISSN 10944087. Available from: doi:10.1364/OE.19.010359.
- [71] CHEN, R. C., L. RIGON and R. LONGO. Comparison of single distance phase retrieval algorithms by considering different object composition and the effect of statistical and structural noise. *Optics Express*. 2013, vol. 21, no. 6, pp. 7384. ISSN 1094-4087. Available from: doi:10.1364/oe.21.007384.
- [72] LANGER, M., P. CLOETENS, J. P. GUIGAY and F. PEYRIN. Quantitative comparison of direct phase retrieval algorithms in in-line phase tomography. *Medical Physics*. 2008, vol. 35, no. 10, pp. 4556–4566. ISSN 00942405. Available from: doi:10.1118/1.2975224.
- [73] BRADLEY, R. S., A. MCNEIL and P. J. WITHERS. An examination of phase retrieval algorithms as applied to phase contrast tomography using laboratory sources. *Developments in X-Ray Tomography VII*. 2010, vol. 7804, no. 6, pp. 780404. Available from: doi:10.1117/12.860536.
- [74] TÖPPERWIEN, M., M. KRENKEL, F. QUADE and T. SALDITT. Laboratory-based x-ray phase-contrast tomography enables 3D virtual histology. In: *Advances in Laboratory-based X-Ray Sources, Optics, and Applications V*. 2016. Available from: doi:10.1117/12.2246460.
- [75] PAGANIN, D., S. C. MAYO, T. E. GUREYEV, P. R. MILLER and S. W. WILKINS. Simultaneous phase and amplitude extraction from a single defocused image of a homogeneous object. *Journal of Microscopy*. 2002, vol. 206, no. 1, pp. 33–40. ISSN 00222720. Available from: doi:10.1046/j.1365-2818.2002.01010.x.
- [76] GROSO, A., R. ABELA and M. STAMPANONI. Implementation of a fast method for high resolution phase contrast tomography. *Optics Express*. 2006, vol. 14, no. 18, pp. 8103. Available from: doi:10.1364/oe.14.008103.
- [77] DIERICK, M., M. BOONE, Y. DE WITTE, L. VAN HOOREBEKE and J. VLASSEN BROECK. Bronnikov-aided correction for x-ray computed tomography. *Journal of the Optical Society of America A*. 2009, vol. 26, no. 4, pp. 890. ISSN 1084-7529. Available from: doi:10.1364/josaa.26.000890.
- [78] DE CHIFFRE, L., S. CARMIGNATO, J.-P. KRUTH, R. SCHMITT and A. WECKENMANN. Industrial applications of computed tomography. *CIRP Annals*. 2014, vol. 63, no. 2, pp. 655–677. ISSN 00078506. Available from: doi:10.1016/j.cirp.2014.05.011.
- [79] *Industrial X-Ray Computed Tomography*. Cham: Springer International Publishing, 2018. ISBN 978-3-319-59571-9. Available from: doi:10.1007/978-3-319-59573-3.
- [80] The Nobel Prize in Physiology or Medicine 1979. *Nobel Media AB 2019* [online]. Available from: <https://www.nobelprize.org/prizes/medicine/1979/summary/>.
- [81] KALENDER, W. *Computed tomography: fundamentals, system technology, image quality, applications*. Publicis MCD Verl, 2011. ISBN 978-3-89578-081-3.
- [82] SUN, W., S. B. BROWN and R. K. LEACH. An Overview of Industrial X-ray computed tomography. *Advances in Management*. 2011, vol. 4, no. 3, pp. 64–65. ISSN 09742611.

REFERENCES

- [83] WANG, M. *Industrial Tomography Systems and Applications*. Woodhead Publishing, 2015. ISBN 978-1-78242-123-8.
- [84] HAMPL, A., A. HELLANDER, D. GYLLBORG, E. COEN, L. S. WEINSTEIN, I. ADAMEYKO, K. FRIED, A. ERICKSON, Y. MISHINA, J. D. CURRIE, E. ARENAS, P. SOUTHAM, M. TESAROVA, A. DUDLEY, T. ZIKMUND, J. JAROS, A.-S. JOHANSSON, M. KAUCKA, E. M. TANAKA, L. LI, H. QIAN, M. CHEN, B. SZAROWSKA, H. BRISMAR, J. KAISER, P. T. NEWTON, V. DYACHUK, J. PETERSEN and A. S. CHAGIN. Oriented clonal cell dynamics enables accurate growth and shaping of vertebrate cartilage. *eLife*. 2017, vol. 6, no. 6. ISSN 2050084X. Available from: doi:10.7554/elife.25902.
- [85] KALASOVÁ, D., K. DVOŘÁK, M. SLOBODNÍK, D. VŠIANSKÝ, T. ZIKMUND, J. DLUHOŠ, R. VÁŇA, J. BUREŠ and J. KAISER. Characterization of inner structure of limestone by X-ray computed sub-micron tomography. *Construction and Building Materials*. 2018, vol. 6, no. 6, pp. 693–700. ISSN 09500618. Available from: doi:10.1016/j.conbuildmat.2018.04.142.
- [86] CNUUDE, V. and M. N. BOONE. High-resolution X-ray computed tomography in geosciences: A review of the current technology and applications. *Earth-Science Reviews*. 2013, vol. 6, no. 6, pp. 1–17. ISSN 00128252. Available from: doi:10.1016/j.earscirev.2013.04.003.
- [87] HANNA, R. D. and R. A. KETCHAM. X-ray computed tomography of planetary materials: A primer and review of recent studies. *Chemie der Erde - Geochemistry*. 2017, vol. 6, no. 6, pp. 547–572. ISSN 00092819. Available from: doi:10.1016/j.chemer.2017.01.006.
- [88] KAISER, J., J. FRIML, T. ZIKMUND, G. MELNYK and K. PROCHÁZKOVÁ. Investigation of Cheb relief intarsia and the study of the technological process of its production by micro computed tomography. *Journal of Cultural Heritage*. 2014, vol. 15, no. 6, pp. 609–613. ISSN 12962074. Available from: doi:10.1016/j.culher.2013.12.006.
- [89] SCHOEMAN, L., P. WILLIAMS, A. du PLESSIS and M. MANLEY. X-ray micro-computed tomography for non-destructive characterisation of food microstructure. *Trends in Food Science and Technology*. 2016, vol. 47, pp. 10–24. ISSN 09242244. Available from: doi:10.1016/j.tifs.2015.10.016.
- [90] KAMPSCHULTE, M., A. LANGHEINIRCH, J. SENDER, H. LITZLBAUER, U. ALTHÖHN, J. SCHWAB, E. ALEJANDRE-LAFONT, G. MARTELS and G. KROMBACH. Nano-Computed Tomography: Technique and Applications. *RöFo - Fortschritte auf dem Gebiet der Röntgenstrahlen und der bildgebenden Verfahren*. 2016, vol. 188, no. 02, pp. 146–154. ISSN 1438-9029. Available from: doi:10.1055/s-0041-106541.
- [91] CZABAJ, M. W., M. L. RICCIO and W. W. WHITACRE. Numerical reconstruction of graphite/epoxy composite microstructure based on sub-micron resolution X-ray computed tomography. *Composites Science and Technology*. 2014, vol. 105, pp. 174–182. ISSN 02663538. Available from: doi:10.1016/j.compscitech.2014.10.017.

- [92] GELB, J., M. FESER, A. TKACHUK, G. HSU, S. CHEN, H. CHANG, T. FONG, L. HUNTER, I. GOLDBERGER, S.-H. LAU and W. YUN. Sub-micron X-ray Computed Tomography for Non-Destructive 3D Visualization and Analysis. *Microscopy and Microanalysis*. 2009, vol. 15, no. S2, pp. 618–619. ISSN 1431-9276. Available from: doi:10.1017/S1431927609093623.
- [93] HANECA, K., K. DEFORCE, M. N. BOONE, D. VAN LOO, M. DIERICK, J. VAN ACKER and J. VAN DEN BULCKE. X-ray sub-micron tomography as a tool for the study of archaeological wood preserved through the corrosion of metal objects. *Archaeometry*. 2012, vol. 54, no. 5, pp. 893–905. ISSN 0003813X. Available from: doi:10.1111/j.1475-4754.2011.00640.x.
- [94] ASAIZUMI, M., T. KATO, T. KUGA, N. OODE, T. ODA, T. SAKURADA, K. THOMSON, T. TABARA and R. I. KARLINSEY. Submicron X-Ray Computed Tomography of Human Dentin Treated with Topical Fluoride Modalities. *EC Dental Science*. 2016, no. 5.2, pp. 992–1017.
- [95] RITMAN, E. L. Micro-Computed Tomography -Current Status and Developments. *Annual Review of Biomedical Engineering*. 2004, vol. 6, no. 1, pp. 185–208. Available from: doi:10.1146/annurev.bioeng.6.040803.140130.
- [96] *phoenix nanotom m*. [online]. Available from: <https://www.industrial.ai/inspection-technologies/radiography-ct/x-ray-computed-tomography/phoenix-nanotom-m>.
- [97] REICHARDT, M., T. SALDITT, M. TOEPFERWIEN, J. FROHN, F. ALVES, A. MARKUS and J.-D. NICOLAS. Nanoscale holographic tomography of heart tissue with x-ray waveguide optics. In: *Developments in X-Ray Tomography XI*. SPIE, 2017. ISBN 9781510612396. Available from: doi:10.1117/12.2276648.
- [98] TÖPPERWIEN, M., M. KRENKEL, D. VINCENZ, F. STÖBER, A. M. OELSCHLE-GEL, J. GOLDSCHMIDT and T. SALDITT. Three-dimensional mouse brain cytoarchitecture revealed by laboratory-based x-ray phase-contrast tomography. *Scientific Reports*. 2017, vol. 7. ISSN 20452322. Available from: doi:10.1038/srep42847.
- [99] *X-Ray Microscope*. [online]. Available from: <https://www.rigaku.com/en/products/xrm/nano3dx>.
- [100] ZEISS X-ray Tomography Solutions. [online]. Available from: <https://www.zeiss.com/microscopy/int/products/x-ray-microscopy.html>.
- [101] *3D X-ray Microscopy*. [online]. Available from: <https://www.bruker.com/products/microtomography.html>.
- [102] *Excillum*. [online]. Available from: <http://www.excillum.com/>.
- [103] HEMBERG, O., M. OTENDAL and H. M. HERTZ. Liquid-metal-jet anode electron-impact x-ray source. *Applied Physics Letters*. 2003, vol. 6, no. 6, pp. 1483–1485. ISSN 0003-6951. Available from: doi:10.1063/1.1602157.
- [104] TÖPPERWIEN, M., R. GRADL, D. KEPPELER, M. VASSHOLZ, A. MEYER, R. HESSLER, K. ACHTERHOLD, B. GLEICH, M. DIEROLF, F. PFEIFFER, T. MOSER and T. SALDITT. Propagation-based phase-contrast x-ray tomography of cochlea using a compact synchrotron source. *Scientific Reports*. 2018, vol. 8, no. 1, pp. 4922. ISSN 20452322. Available from: doi:10.1038/s41598-018-23144-5.

REFERENCES

- [105] TUOHIMAA, T., M. OTENDAL and H. M. HERTZ. Phase-contrast x-ray imaging with a liquid-metal-jet-anode microfocus source. *Applied Physics Letters*. 2007, vol. 6, no. 6, pp. 74104. ISSN 00036951. Available from: doi:10.1063/1.2769760.
- [106] RUEDEN, C. T., J. SCHINDELIN, M. C. HINER, B. E. DEZONIA, A. E. WALTER, E. T. ARENA and K. W. ELICEIRI. ImageJ2: ImageJ for the next generation of scientific image data. *BMC Bioinformatics*. 2017, vol. 18, no. 1, pp. 529. ISSN 14712105. Available from: doi:10.1186/s12859-017-1934-z.
- [107] SCHINDELIN, J., I. ARGANDA-CARRERAS, E. FRISE, V. KAYNIG, M. LONGAIR, T. PIETZSCH, S. PREIBISCH, C. RUEDEN, S. SAALFELD, B. SCHMID, J.-Y. TINEVEZ, D. J. WHITE, V. HARTENSTEIN, K. ELICEIRI, P. TOMANCAK and A. CARDONA. Fiji: an open-source platform for biological-image analysis. *Nature Methods*. 2012, vol. 9, no. 7, pp. 676–682. ISSN 15487091. Available from: doi:10.1038/nmeth.2019.
- [108] *MATLAB*. [online]. USA: The MathWorks, Inc. Available from: <https://se.mathworks.com/products/matlab.html>.
- [109] *VGStudio MAX*. [online]. Germany: Volume Graphics GmbH. Available from: <https://www.volumegraphics.com/en/products/vgstudio-max.html>.
- [110] *MAVI - Modular Algorithms for Volume Images*. [online]. Germany: Fraunhofer Institute fo Industrial Mathematics. Available from: <https://www.itwm.fraunhofer.de/en/departments/bv/products-and-services/mavi.html>.
- [111] BRUN, F., L. MANCINI, P. KASAE, S. FAVRETTO, D. DREOSSI and G. TROMBA. Pore3D: A software library for quantitative analysis of porous media. *Nuclear Instruments and Methods in Physics Research, Section A: Accelerators, Spectrometers, Detectors and Associated Equipment*. 2010, vol. 615, no. 3, pp. 326–332. ISSN 01689002. Available from: doi:10.1016/j.nima.2010.02.063.
- [112] *X-ray complex refraction coefficient*. [online]. [Visited on 2016-1-7]. Available from: <http://ts-imaging.net/Services/Simple/ICUtilXdata.aspx>.
- [113] ALBERTINI, G., A. GIULIANI, V. KOMLEV, F. MORONCINI, A. PUGNALONI, G. PENNESI, M. BELICCHI, C. RUBINI, F. RUSTICHELLI, R. TASSO and Y. TORRENTE. Organization of Extracellular Matrix Fibers Within Polyglycolic Acid–Polylactic Acid Scaffolds Analyzed Using X-Ray Synchrotron-Radiation Phase-Contrast Micro Computed Tomography. *Tissue Engineering Part C: Methods*. 2009, vol. 15, no. 3, pp. 403–411. ISSN 1937-3384. Available from: doi:10.1089/ten.tec.2008.0270.
- [114] CEDOLA, A., G. CAMPI, D. PELLICCIA, I. BUKREEVA, M. FRATINI, M. BURGHAMMER, L. RIGON, F. ARFELLI, R. CHANG CHEN, D. DREOSSI, N. SODINI, S. MOHAMMADI, G. TROMBA, R. CANCEDDA and M. MASTROGIACOMO. Three dimensional visualization of engineered bone and soft tissue by combined x-ray micro-diffraction and phase contrast tomography. *Physics in Medicine and Biology*. 2014, vol. 59, no. 1, pp. 189–201. ISSN 0031-9155. Available from: doi:10.1088/0031-9155/59/1/189.

- [115] GIULIANI, A., F. MORONCINI, S. MAZZONI, M. L. C. BELICCHI, C. VILLA, S. ERRATICO, E. COLOMBO, F. CALCATERRA, L. BRAMBILLA, Y. TORRENTE, G. ALBERTINI and S. DELLA BELLA. Polyglycolic Acid–Polylactic Acid Scaffold Response to Different Progenitor Cell In Vitro Cultures: A Demonstrative and Comparative X-Ray Synchrotron Radiation Phase-Contrast Microtomography Study. *Tissue Engineering Part C: Methods*. 2014, vol. 20, no. 4, pp. 308–316. ISSN 1937-3384. Available from: doi:10.1089/ten.tec.2013.0213.
- [116] THIMM, B. W., S. HOFMANN, P. SCHNEIDER, R. CARRETTA and R. MÜLLER. Imaging of Cellular Spread on a Three-Dimensional Scaffold by Means of a Novel Cell-Labeling Technique for High-Resolution Computed Tomography. *Tissue Engineering Part C: Methods*. 2012, vol. 18, no. 3, pp. 167–175. ISSN 1937-3384. Available from: doi:10.1089/ten.tec.2011.0262.
- [117] THURNER, P., B. MÜLLER, U. SENNHAUSER, J. HUBBELL and R. MÜLLER. Tomography studies of biological cells on polymer scaffolds. *Journal of Physics: Condensed Matter*. 2004, vol. 16, no. 33, pp. S3499–S3510. ISSN 0953-8984. Available from: doi:10.1088/0953-8984/16/33/011.
- [118] THURNER, P., B. MÜLLER, F. BECKMANN, T. WEITKAMP, C. RAU, R. MÜLLER, J. A. HUBBELL and U. SENNHAUSER. Tomography studies of human foreskin fibroblasts on polymer yarns. *Nuclear Instruments and Methods in Physics Research Section B: Beam Interactions with Materials and Atoms*. 2003, vol. 200, pp. 397–405. ISSN 0168583X. Available from: doi:10.1016/S0168-583X(02)01729-9.
- [119] TORRENTE, Y., M. GAVINA, M. BELICCHI, F. FIORI, V. KOMLEV, N. BRESOLIN and F. RUSTICHELLI. High-resolution X-ray microtomography for three-dimensional visualization of human stem cell muscle homing. *FEBS Letters*. 2006, vol. 580, no. 24, pp. 5759–5764. ISSN 00145793. Available from: doi:10.1016/j.febslet.2006.09.031.
- [120] ZEHBE, R., J. GOEBBELS, Y. IBOLD, U. GROSS and H. SCHUBERT. Three-dimensional visualization of in vitro cultivated chondrocytes inside porous gelatine scaffolds: A tomographic approach. *Acta Biomaterialia*. 2010, vol. 6, no. 6, pp. 2097–2107. ISSN 17427061. Available from: doi:10.1016/j.actbio.2009.11.020.
- [121] HILLDORE, A., A. WOJTOWICZ and A. W. JOHNSON. Micro-CT based quantification of non-mineralized tissue on cultured hydroxyapatite scaffolds. *Journal of Biomedical Materials Research Part A*. 2007, vol. 82A, no. 4, pp. 1012–1021. ISSN 15493296. Available from: doi:10.1002/jbm.a.31264.
- [122] DORSEY, S. M., S. LIN-GIBSON and C. G. SIMON. X-ray microcomputed tomography for the measurement of cell adhesion and proliferation in polymer scaffolds. *Biomaterials*. 2009, vol. 30, no. 16, pp. 2967–2974. ISSN 01429612. Available from: doi:10.1016/j.biomaterials.2009.02.032.
- [123] SOMMER, M. R., J. R. VETSCH, J. LEEMANN, R. MÜLLER, A. R. STUDART and S. HOFMANN. Silk fibroin scaffolds with inverse opal structure for bone tissue engineering. *Journal of Biomedical Materials Research Part B: Applied Biomaterials*. 2017, vol. 105, no. 7, pp. 2074–2084. ISSN 15524973. Available from: doi:10.1002/jbm.b.33737.

REFERENCES

- [124] CHAMIEH, F., A.-M. COLLIGNON, B. R. COYAC, J. LESIEUR, S. RIBES, J. SADOINE, A. LLORENS, A. NICOLETTI, D. LETOURNEUR, M.-L. COLOMBIER, S. N. NAZHAT, P. BOUCHARD, C. CHAUSSAIN and G. Y. ROCHEFORT. Accelerated craniofacial bone regeneration through dense collagen gel scaffolds seeded with dental pulp stem cells. *Scientific Reports*. 2016, vol. 6, no. 1, pp. 38814. Available from: doi:10.1038/srep38814.
- [125] CARTMELL, S., K. HUYNH, A. LIN, S. NAGARAJA and R. GULDBERG. Quantitative microcomputed tomography analysis of mineralization within three dimensional scaffolds in vitro. *Journal of Biomedical Materials Research*. 2004, vol. 69A, no. 1, pp. 97–104. ISSN 0021-9304. Available from: doi:10.1002/jbm.a.20118.
- [126] FASSINA, L., E. SAINO, L. VISAI, J. SCHELFHOUT, M. DIERICK, L. VAN HOOREBEKE, P. DUBRUEL, F. BENAZZO, G. MAGENES and S. VAN VLLERBERGHE. Electromagnetic Stimulation to Optimize the Bone Regeneration Capacity of Gelatin-Based Cryogels. *International Journal of Immunopathology and Pharmacology*. 2012, vol. 25, no. 1, pp. 165–174. ISSN 0394-6320. Available from: doi:10.1177/039463201202500119.
- [127] YEON KWON, D., J. SEON KWON, S. HUN PARK, J. HUN PARK, S. HEE JANG, X. YUN YIN, J.-H. YUN, J. HO KIM, B. HYUN MIN, J. HEE LEE, W.-D. KIM and M. SUK KIM. A computer-designed scaffold for bone regeneration within cranial defect using human dental pulp stem cells. *Scientific Reports*. 2015, vol. 5, no. 1, pp. 12721. ISSN 2045-2322. Available from: doi:10.1038/srep12721.
- [128] SHEPHERD, D. V., J. H. SHEPHERD, S. M. BEST and R. E. CAMERON. 3D imaging of cells in scaffolds: direct labelling for micro CT. *Journal of Materials Science: Materials in Medicine*. 2018, vol. 29, no. 6, pp. 86. ISSN 0957-4530. Available from: doi:10.1007/s10856-018-6089-6.
- [129] THIBEAUX, R., E. PERRIN, B. SMANIOTTO, H. DUVAL, E. VENNAT, D. NERON and B. DAVID. Using X-ray computed tomography for quantification of cell proliferation within a perfusion bioreactor. *Computer Methods in Biomechanics and Biomedical Engineering*. 2015, vol. 18, no. sup1, pp. 2072–2073. ISSN 1025-5842. Available from: doi:10.1080/10255842.2015.1069568.
- [130] VORONOV, R. S., S. B. VANGORDON, R. L. SHAMBAUGH, D. V. PAPAVALASSIOLIOU and V. I. SIKAVITSAS. 3D Tissue-Engineered Construct Analysis via Conventional High-Resolution Microcomputed Tomography Without X-Ray Contrast. *Tissue Engineering Part C: Methods*. 2013, vol. 19, no. 5, pp. 327–335. ISSN 1937-3384. Available from: doi:10.1089/ten.tec.2011.0612.
- [131] PAPANTONIOU, I., M. SONNAERT, L. GERIS, F. P. LUYTEN, J. SCHROOTEN and G. KERCKHOFS. Three-Dimensional Characterization of Tissue-Engineered Constructs by Contrast-Enhanced Nanofocus Computed Tomography. *Tissue Engineering Part C: Methods*. 2014, vol. 20, no. 3, pp. 177–187. ISSN 1937-3384. Available from: doi:10.1089/ten.tec.2013.0041.
- [132] VOJTOVÁ, L., T. ZIKMUND, V. PAVLIŇÁKOVÁ, J. ŠALPLACHTA, D. KALASOVÁ, E. PROSECKÁ, J. BRTNÍKOVÁ, J. ŽÍDEK, D. PAVLIŇÁK and J. KAISER. The 3D imaging of mesenchymal stem cells on porous scaffolds using high-contrasted x-ray computed nanotomography. *Journal of Microscopy*. 2019, vol. 273, no. 3, pp. 169–177. ISSN 00222720. Available from: doi:10.1111/jmi.12771.

- [133] BRADLEY, R. S., I. K. ROBINSON and M. YUSUF. 3D X-Ray Nanotomography of Cells Grown on Electrospun Scaffolds. *Macromolecular Bioscience*. 2017, vol. 17, no. 2, pp. 1600236. ISSN 16165187. Available from: doi:10.1002/mabi.201600236.
- [134] ANOVITZ, L. M. and D. R. COLE. Characterization and Analysis of Porosity and Pore Structures. *Reviews in Mineralogy and Geochemistry*. 2015, vol. 80, no. 1, pp. 61–164. ISSN 1529-6466. Available from: doi:10.2138/rmg.2015.80.04.
- [135] HO, S. T. and D. W. HUTMACHER. A comparison of micro CT with other techniques used in the characterization of scaffolds. *Biomaterials*. 2006, vol. 27, no. 8. ISSN 01429612. Available from: doi:10.1016/j.biomaterials.2005.08.035.
- [136] ZOU, Y. and J. MALZBENDER. Development and optimization of porosity measurement techniques. *Ceramics International*. 2016, vol. 42, no. 2, pp. 2861–2870. ISSN 02728842. Available from: doi:10.1016/j.ceramint.2015.11.015.
- [137] KALASOVÁ, D., T. ZIKMUND and J. KAISER. Computed Tomography for Inspection of Inner Structure of Materials. In: *CEITEC PhD Retreat II, Telč 20-21 April 2017 - Book of Abstracts*. Masaryk University, 2017. ISBN 978-80-210-8550-3.
- [138] STASTNY, P., Z. CHLUP, D. KALASOVA, T. ZIKMUND, J. KAISER and M. TRUNEC. Epoxy-based gelcasting of machinable hydroxyapatite foams for medical applications. *Journal of the American Ceramic Society*. 2018, vol. 101, no. 8, pp. 3317–3327. ISSN 00027820. Available from: doi:10.1111/jace.15523.
- [139] PALLUA, J. D., V. KUHN, R. PÖDER, A. F. PALLUA, K. PFALLER, W. RECHEIS and A. K. PALLUA. Application of micro-computed tomography to microstructure studies of the medicinal fungus *Herichium coralloides*. *Mycologia*. 2015, vol. 107, no. 1, pp. 227–238. ISSN 0027-5514. Available from: doi:10.3852/14-188.
- [140] WALTON, L. A., R. S. BRADLEY, P. J. WITHERS, V. L. NEWTON, R. E. WATSON, C. AUSTIN and M. J. SHERRATT. Morphological characterisation of unstained and intact tissue micro-architecture by X-ray computed micro- and nanotomography. *Scientific Reports*. 2015, vol. 6, no. 6. ISSN 20452322. Available from: doi:10.1038/srep10074.
- [141] PARLANTI, P., V. CAPPELLO, F. BRUN, G. TROMBA, R. RIGOLIO, I. TONAZZINI, M. CECCHINI, V. PIAZZA and M. GEMMI. Size and specimen-dependent strategy for x-ray micro-ct and tem correlative analysis of nervous system samples. *Scientific Reports*. 2017, vol. 7, no. 1. ISSN 20452322. Available from: doi:10.1038/s41598-017-02998-1.
- [142] BEYER, T., D. TOWNSEND, T. BRUN, P. KINAHAN, M. CHARRON, R. RODDY, J. JERIN, J. YOUNG, L. BYARS and R. NUTT. A combined PET/CT scanner for clinical oncology. *Journal of nuclear medicine : official publication, Society of Nuclear Medicine*. 2000, vol. 41, no. 8, pp. 1369–1379. ISSN 0161-5505.
- [143] ERGONUL, A. G., T. I. AKCAM, A. ÖZDIL, K. TURHAN, A. CAKAN and U. CAGIRICI. Diagnostic value of 18F-FDG-PET/CT in benign lung diseases. *Kardiocirurgia i Torakochirurgia Polska*. 2018, vol. 6, no. 6, pp. 1–4. ISSN 17315530. Available from: doi:10.5114/kitp.2018.74667.

REFERENCES

- [144] BASHA, M. A. A., A. F. AHMED, S. M. SHEHATA, D. A. E. A. EL SAMMAK, E. H. ABDELBAR, A. A. OBAYA, T. FATHY, H. Y. YOUSEF and M. Z. ALAZZAZY. Does a combined CT and MRI protocol enhance the diagnostic efficacy of LI-RADS in the categorization of hepatic observations? A prospective comparative study. *European Radiology*. 2018, vol. 6, no. 6, pp. 2592–2603. ISSN 0938-7994. Available from: doi:10.1007/s00330-017-5232-y.
- [145] LEE, Y. S., J. K. SEON, V. I. SHIN, G. H. KIM and M. JEON. Anatomical evaluation of CT-MRI combined femoral model. *BioMedical Engineering Online*. 2008, vol. 6, no. 6, pp. 6. ISSN 1475925X. Available from: doi:10.1186/1475-925X-7-6.
- [146] BURNETT, T. L., S. A. MCDONALD, A. GHOLINIA, R. GEURTS, M. JANUS, T. SLATER, S. J. HAIGH, C. ORNEK, F. ALMUAILI, D. L. ENGELBERG, G. E. THOMPSON and P. J. WITHERS. Correlative tomography. *Scientific Reports*. 2014, vol. 6, no. 6. ISSN 20452322. Available from: doi:10.1038/srep04711.
- [147] DE BOEVER, W., H. DERLUYN, D. VAN LOO, L. VAN HOOREBEKE and V. CNUUDE. Data-fusion of high resolution X-ray CT, SEM and EDS for 3D and pseudo-3D chemical and structural characterization of sandstone. *Micron*. 2015, vol. 74, pp. 15–21. ISSN 09684328. Available from: doi:10.1016/j.micron.2015.04.003.
- [148] CHAURAND, P., W. LIU, D. BORSCHNECK, C. LEVARD, M. AUFFAN, E. PAUL, B. COLLIN, I. KIEFFER, S. LANONE, J. ROSE and J. PERRIN. Multi-scale X-ray computed tomography to detect and localize metal-based nanomaterials in lung tissues of in vivo exposed mice. *Scientific Reports*. 2018, vol. 8, no. 1. ISSN 20452322. Available from: doi:10.1038/s41598-018-21862-4.
- [149] KALASOVÁ, D., V. PAVLIŇÁKOVÁ, T. ZIKMUND, L. VOJTOVÁ and J. KAISER. Correlation of X-ray Computed Nanotomography and Scanning Electron Microscopy Imaging of Collagen Scaffolds. *Microscopy and Microanalysis*. 2018, vol. 24, no. S2, pp. 104–105. ISSN 1431-9276. Available from: doi:10.1017/S1431927618012904.
- [150] KALASOVÁ, D., J. MAŠEK, T. ZIKMUND, P. SPURNÝ, J. HALODA, R. BURGET and J. KAISER. Segmentation of Multi-Phase Object Applying Trainable Segmentation. *e-Journal of Nondestructive Testing*. 2017, vol. 2017. ISSN 1435-4934.

List of symbols and shortcuts

a	typical dimension
BAC	Bronnikov aided correction
BUT	Brno University of Technology
C_{ABS}	absorption contrast
$C_{\text{ABS, gain}}$	absorption contrast gain
C_{PHC}	phase contrast
CCD	charge-coupled device
CEITEC	Central European Institute of Technology
CFRP	carbon fibre reinforced polymer
CT	X-ray computed tomography
CTF	contrast transfer function
E	energy
EDS	X-ray energy dispersive spectroscopy
f	atomic form factor, or general function
f_1, f_2, f^0, f'	components of atomic form factor
$\mathcal{F}\{f(x)\}$	Fourier transform of a function $f(x)$
$\mathcal{F}^{-1}\{f(x)\}$	inverse Fourier transform of a function $f(x)$
$F(u, v)$	Fourier transform of the function representing the object
$f(x, y)$	function representing the object
f_{ROD}	Rodbard function
$\mathcal{F}\{f(x)\}$	Fourier transform of function $f(x)$
FIB	focused ion beam
FOV	field of view

LIST OF SYMBOLS AND SHORTCUTS

\hbar	reduced Planck constant
HRes	high resolution
I	intensity of radiation after passing through the sample
I_0	intensity of radiation = $[\text{W}\cdot\text{m}^{-2}]$
I_F	intensity of radiation in Fourier space
I_z	intensity of radiation at z position
I_{BCG}	intensity of background
I_{MAT}	intensity of material
I_{MAX}	maximum intensity
I_{MIN}	minimal intensity
$I_{20\%}$	20 % of intensity difference between I_{MAT} and I_{BCG}
$I_{80\%}$	80 % of intensity difference between I_{MAT} and I_{BCG}
j_0	spectral density of intensity
k, \vec{k}	wave number, wave vector
L_{lat}	lateral coherence length
L_{shear}	shearing coherence length
LFoV	large field of view
LM	light microscopy
LPS	linear pixel size
LVS	linear voxel size
M	magnification
m_a	absorbance
MBA	Modified Bronnikov algorithm
microCT	X-ray computed microtomography
medCT	medical X-ray computed tomography
n	index of refraction
N	number, number density
N_F	Fresnel number
nCT	X-ray computed nanotomography

p	pixel size, or projection of an object on a detector
P	Fourier transform of a projection
PA	Paganin algorithm
PBI	propagation-based imaging
PEDT	polyethylene rod with double-sided tape
PCI	phase contrast imaging
\vec{Q}	scattering vector
r_0	classical radius of electron ($r_0 = 2.8$ fm)
R_E	edge resolution
$s, s(x, y)$	focal spot size, or source intensity distribution
sCMOS	scientific complementary metal–oxide–semiconductor
SEM	scanning electron microscopy
SDD	sample–detector distance
SNR	signal to noise ratio
SNR_{gain}	signal to noise ratio gain
SSD	source–sample distance
STD_{ROD}	standard deviation of fitting of Rodbard function
sub- μ CT	X-ray computed sub-micron tomography
t	thickness of an object
T	transmission function
TIE	transport of intensity equation
u, v	reciprocal coordinates in plane perpendicular to the optical axis
U	unsharpness
x, y	spatial coordinates in plane perpendicular to the optical axis
$x_{20\%}$	horizontal axis value of $I_{20\%}$
$x_{80\%}$	horizontal axis value of $I_{80\%}$
y_D	source–detector distance
y_S	source–sample distance
z	spatial coordinate along the optical axis

LIST OF SYMBOLS AND SHORTCUTS

Z	atomic number
z_{eff}	effective propagation distance
z_u	distance of the first phase CTF maximum
α	regularization parameter in MBA and BAC algorithms
β	imaginary part of index of refraction
γ	regularization parameter in BAC algorithm
δ	real part of index of refraction (index refraction decrement), or δ -distribution
ζ	filter applied on projections
θ	angle from x -axis in x, y plane, angle from u -axis in u, v plane
ϑ	scattering angle
λ	wavelength
μ	linear attenuation coefficient
μ_{mass}	mass attenuation coefficient
μCT	X-ray computed microtomography
ϱ	density, or distance from the origin of the coordinate system in plane x, y (spatial domain)
ϱ_e	number density of electrons per unit volume
σ	attenuation cross-section
φ	phase
φ_{MBA}	phase calculated by MBA algorithm
Φ	line, curve
ξ	argument of contrast transfer function
$\psi(x, y)$	wave function
ω	angular frequency
Ω	distance from the origin of the coordinate system in plane u, v (frequency domain)

A. Supplementary data

This section contains supplementary data to Sec. 4.3.

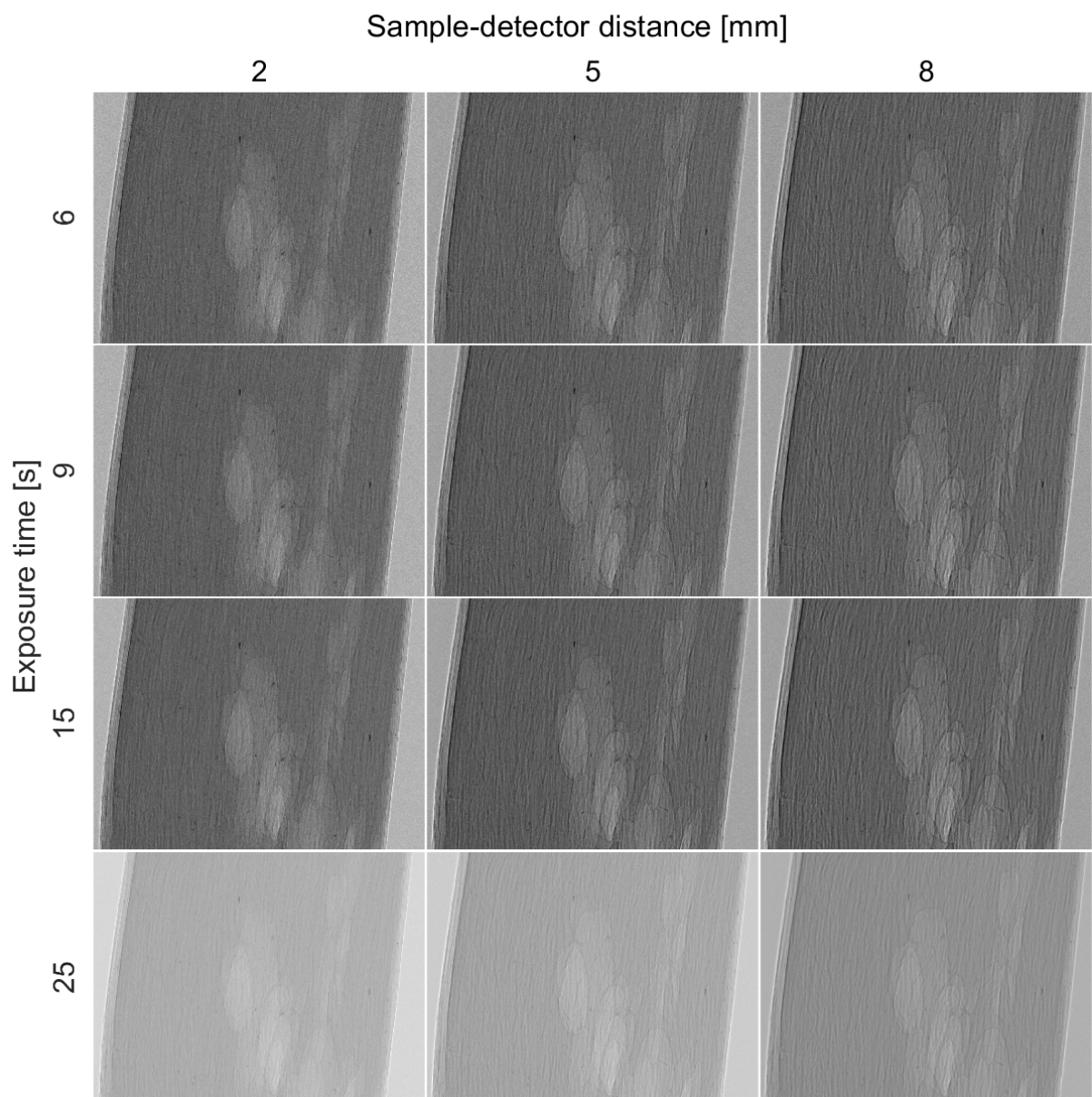


Figure A.1: Projections of CFRP measured with different sample–detector distances and exposure times.

A. SUPPLEMENTARY DATA

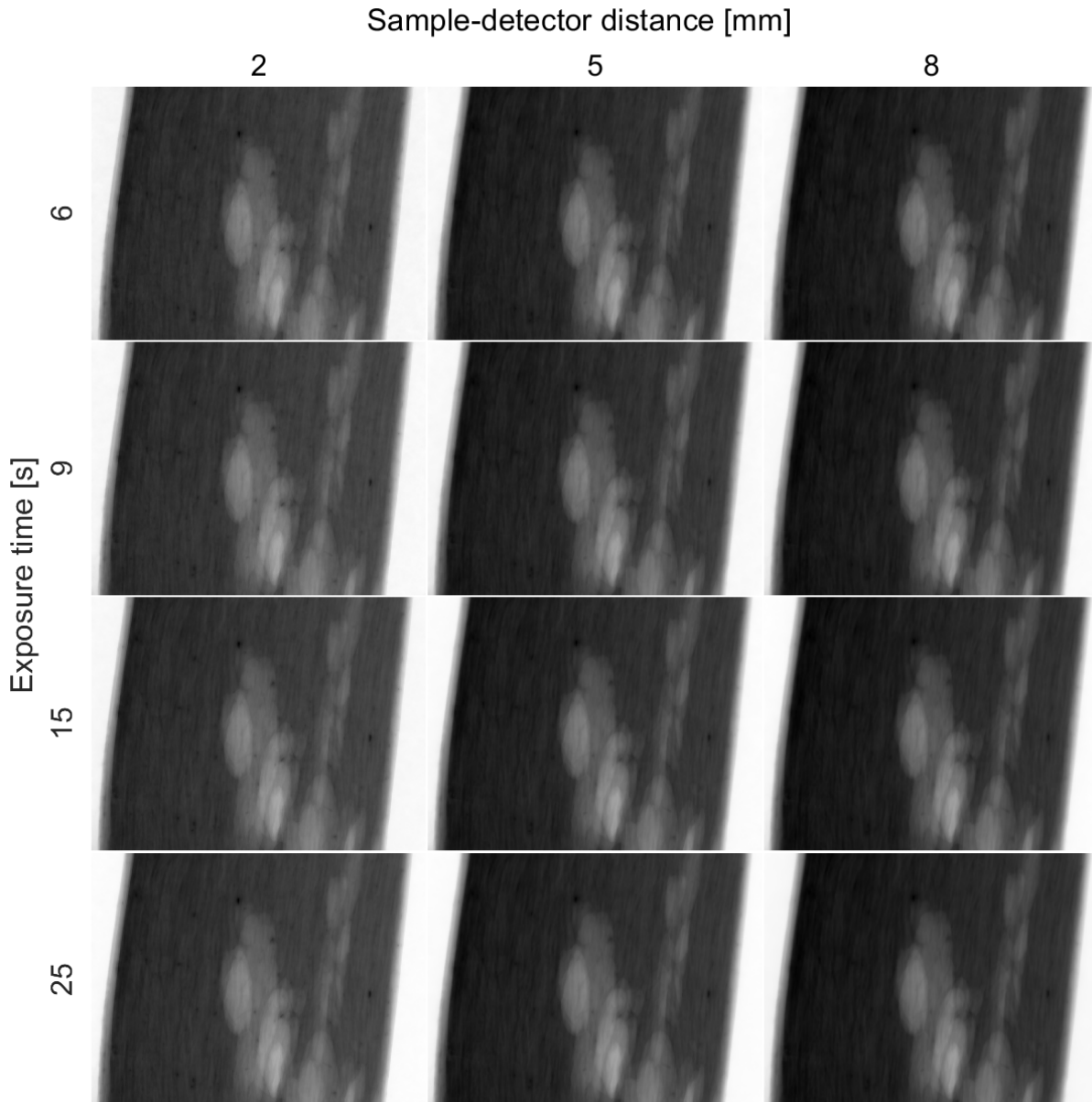


Figure A.2: Phase retrieved projections of CFRP measured with different sample–detector distances and exposure times.

B. Publications

Full texts of first-author publications of the author and one poster [137] are listed here. [37, 85] are full papers in impacted journals, [149] is a 2-page conference abstract published as supplementary material to an impacted journal, [150] is a full paper in a journal without impact factor.

Characterization of a laboratory-based X-ray computed nanotomography system for propagation-based method of phase contrast imaging

Dominika Kalasová, Tomáš Zikmund, Ladislav Pína, Yoshihiro Takeda, Martin Horváth, Kazuhiko Omote, and Jozef Kaiser

Abstract—Phase contrast imaging (PCI) is used to extend X-ray computed nanotomography (nCT) technique for analyzing samples with a low X-ray contrast, such as polymeric structures or soft tissues. Although this technique is used in many variations at synchrotrons, along with the development of X-ray tubes and X-ray detectors, a phase contrast imaging becomes available also for laboratory systems.

This work is focused on determining the conditions for propagation-based PCI in laboratory nCT systems based on three criteria. It is mostly employed in near-field imaging regime, which is quantified via Fresnel number. X-rays must reach certain degree of coherence to form edge-enhancement. Finally, setup of every CT measurement has to avoid geometrical unsharpness due to the finite focal spot size. These conditions are evaluated and discussed in terms of different properties and settings of CT machine. Propagation-based PCI is tested on a sample of carbon fibres reinforced polyethylene and the implementation of Paganin phase retrieval algorithm on the CT data is shown.

Index Terms—X-ray computed nanotomography, laboratory-based X-ray computed nanotomography, phase contrast imaging, propagation based imaging, characterization of CT system.

I. INTRODUCTION

X-RAY computed nanotomography (nCT) is a nondestructive, 3D imaging method used for analyses of inner structure of materials. This term is used for devices that reach spatial resolution below $1\ \mu\text{m}$ [1], [2]. Unlike X-ray computed microtomography, these devices often have highly precise mechanical parts, advanced X-ray detectors with additional optical units after scintillator and chips based on CCD (Charge-Coupled Device) or sCMOS (Scientific Complementary Metal-Oxide-Semiconductor) technology. Consequently, they are able to process special examination protocols while maintaining a high resolution [3].

This research was carried out under the project CEITEC 2020 (LQ1601) with financial support from the Ministry of Education, Youth and Sports of the Czech Republic under the National Sustainability Programme II. Part of the work was carried out with the support of CEITEC Nano Research Infrastructure (MEYS CR, 2016–2019).

Dominika Kalasová, Tomáš Zikmund and Jozef Kaiser are with CEITEC – Central European Institute of Technology, Brno University of Technology, Purkyňova 123, 612 00 Brno, Czech Republic, emails: dominika.kalasova@ceitec.vutbr.cz, tomas.zikmund@ceitec.vutbr.cz, jozef.kaiser@ceitec.vutbr.cz.

Ladislav Pína and Martin Horváth are with Rigaku Innovative Technologies Europe s.r.o., Novodvorská 994, 14221 Prague 4, Czech Republic, emails: ladislav.pina@rigaku.com, martin.horvath@rigaku.com.

Yoshihiro Takeda and Kazuhiko Omote are with Rigaku Corporation, 3-9-12, Matsubara-cho, Akishima-shi, Tokyo 196-8666, Japan, emails: y-takeda@rigaku.co.jp, omote@rigaku.co.jp.

Phase contrast X-ray computed tomography imaging methods (PCI) make possible the imaging of samples with a low X-ray contrast, such as e.g. polymers, biological soft tissues or scaffolds [4]. PCI is utilized in various fields in biology and medicine for imaging of small animals and soft tissues [5]–[8] and in material science as well, for example in imaging of material discontinuities in polymer composites composed of light materials with similar attenuation coefficient [9]–[11].

The phase of an X-ray beam transmitted through material is shifted due to its interaction with the electron shells of atoms [12]. There are several ways of recording this phase shift and obtaining phase contrast. X-ray interferometry technique is based on the interference of a reference beam with a beam transmitted through the sample [13], [14]. Analyser-based methods involve the reflection on Bragg crystals, which filter different X-rays based on their angle [15], [16]. Talbot-Lau grating interferometry uses the self-imaging property of gratings to make the phase changes visible [17]–[19]. Phase contrast can be also achieved by using X-ray optics in X-ray microscopes [20]–[22].

When X-rays diffracted on inner structures of material propagate through a certain distance, their wavefronts interfere and form an inline phase contrast [23]. If a tomographic setup is modified just by increasing the distance between the sample and the detector, this phase contrast becomes visible in form of edge enhancement [24]. This approach is called propagation based imaging (PBI). For large sample–detector distances, multiple interference fringes appear, which shifts the imaging towards the holographic regime. The imaging regime is described via Fresnel number, as is discussed in the section 2.1.

In PBI, phase changes caused by radiation passing through the object are transformed to variations of measured intensity. The task of retrieving information about the phase change is solved by phase retrieval algorithms [25]–[27]. In [28], phase retrieval approaches taking into account polychromaticity of laboratory-based X-ray source are shown. Nevertheless, also techniques developed for monochromatic radiation would still be appropriate if an average X-ray energy or the main characteristic peak was considered [28], [29]. From an image processing point of view, the application of phase retrieval algorithm is necessary to obtain data with less noise and multimodal histogram, which would be easier to segment [24], [30].

PBI requires a high degree of coherence of X-ray beam, therefore the method is used a lot with the synchrotron radi-

tion [31], but also with laboratory polychromatic sources [32]. Development of materials, precise mechanics, and electron focusing systems in laboratory X-ray sources made the propagation-based imaging available on many CT devices. Examples of edge enhancement via PBI with a laboratory, polychromatic X-ray source have been reported on various examples of fibres in the polymer matrix [33]–[35], mouse lungs [36], liver tissue [37] or cochlea [38] or leaves and insects [39].

Tomographic setup in laboratory-based PBI requires certain conditions to be fulfilled [40]–[43]. Tomographic PBI is usually done in a near-field regime to avoid formation of multiple fringes in larger sample–detector distances (SDD), where the direct morphology information is lost (this is referred to as a holographic or far field regime). This condition on SDD is quantified via Fresnel number [36], [44]. To observe edge-enhancement on structures of certain dimensions, an X-ray beam must reach a sufficient degree of coherence. The coherence requirements on the X-ray beam can be evaluated by the ratio of shearing and lateral coherence length [23] (these terms are explained in section IIB). Laboratory-based X-ray tubes produce an X-ray cone-beam with a finite focal spot size. When a proper geometrical arrangement of components is not set, the unsharpness from the finite focal spot size causes blurring of edges of the sample [45].

Laboratory-based X-ray computed tomography (CT) devices without additional X-ray optics mostly employ geometrical magnification by cone-beam shape of X-rays: the sample is placed close to the X-ray tube and projected to the large-area detector placed at a longer distance (Fig. 1a) [46]. The small voxel size is restricted by focal spot size, therefore for small voxel sizes, small focal spot sizes are necessary. In another approach, so-called inverse geometry [47]–[49], the sample is not placed directly in front of the X-ray tube but the source–sample distance is fixed at a relatively large distance compared to the sample size. The detector is placed close to the sample, so only a small part of the cone-beam at the sample position is used, therefore it is considered semi-parallel (Fig. 1b). The image is magnified by an optical system after scintillator. The small voxel size is achieved by small pixels at the detector, therefore, in this case, a high power source with a large focal spot size is acceptable.

In this work, PBI with a laboratory-based nCT system is studied. Theoretical conditions for PBI are stated. Based on these theoretical assumptions, limits of the nCT machine for PBI are discussed and tested on several measurements of carbon fibres reinforced polyethylene (CFRP) sample. Moreover, application of phase retrieval algorithm is shown as a suitable post-processing method for data acquired by PBI.

II. THEORY

X-ray wavefronts passing through the sample are distorted on samples structures proportionally to the phase shift imposed by the sample. After propagating through a given distance, they interfere to form Fresnel diffraction fringes [32], [34]. In the image, this is visible in form of edge enhancement. The interference is influenced by the sample to detector distance (e.g. imaging regime) and the degree of X-ray coherence.

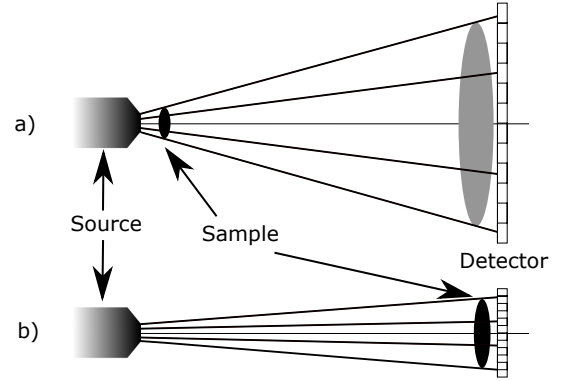


Fig. 1. Different approaches in nCT systems: a) geometrical magnification is reached by use of cone-beam X-ray, b) long source–sample distance is used to achieve semi-parallel X-ray beam at sample position and the image is magnified by optical system after scintillator.

These factors, together with limitations following from finite focal spot size, are discussed in this section.

A. Imaging in near-field regime

For propagation-based phase-contrast imaging in paraxial approximation, the imaging regime is characterized by Fresnel number N_F

$$N_F = \frac{a^2}{\lambda z_{\text{eff}}}, \quad (1)$$

where a is the size of a feature of interest, λ is the wavelength, and $z_{\text{eff}} = \text{SSD} \times \text{SDD} / (\text{SSD} + \text{SDD})$, where SSD is the source–sample distance and SDD is the sample–detector distance (Fig. 2), is the effective propagation distance. The edge enhancement for the given feature size is pronounced when $N_F \approx 1$ [36], [44], and from the obtained images, it is possible to directly extract the morphological information about the sample. For $N_F \ll 1$, not only edge enhancement but also multiple fringes appear, and the real structure is no longer recognizable. This is a so-called holographic, or for very low N_F far-field, regime.

To have the structures of the sample directly recognizable, the holographic regime, e.g. large sample–detector distances, should be avoided. In such case, in order to stay in the near-field regime, $N_F > 1$ should be fulfilled for every structure visible in the image. At the same time, the Fresnel number should not be too large ($N_F \gg 1$) since for small SDDs, the propagation effects are negligible and the results are only absorption images.

B. Degree of X-ray coherence

The superposition of wavefronts for the formation of edge enhancement occurs only if waves are coherent. In case of X-rays emitted from the finite focal spot size, the spatial coherence is given by lateral coherence length $L_{\text{lat}} = \lambda \times \text{SSD} / s$, where s is the focal spot size. Phase contrast is formed between interfering waves from positions separated by a shearing length $L_{\text{shear}} = \lambda \times \text{SDD} / (Ma)$, where $M = (\text{SSD} + \text{SDD}) / \text{SSD}$ stands for magnification. The wave has to have sufficiently high degree of coherence over this length to make phase

contrast visible. Visibility of phase contrast is therefore characterized by ratio $L_{\text{shear}}/L_{\text{lat}}$ [23], [29].

The X-ray beam is almost fully coherent if the ratio $L_{\text{shear}}/L_{\text{lat}} \ll 1$. In practice, the phase contrast fringes occur also when the X-rays are partially coherent and their visibility is improved with an increasing degree of coherence. The criterion for partial coherence can be therefore stated as

$$\frac{L_{\text{shear}}}{L_{\text{lat}}} = \frac{s \times \text{SDD}}{a(\text{SSD} + \text{SDD})} < 1. \quad (2)$$

C. Geometrical unsharpness due to focal spot size

In X-ray tubes, X-rays are always emitted from a finite area called focal spot. The resolution is restricted by the focal spot size because at a given sample–detector distance, the X-rays from the whole area of the focal spot start to form an unsharpened spot of size U on the detector larger than pixel size p (Fig. 2). To avoid this unsharpness, the condition $U < p$ must be fulfilled. From the geometry of the system, this means

$$\frac{\text{SDD}}{\text{SSD}} \times s < p. \quad (3)$$

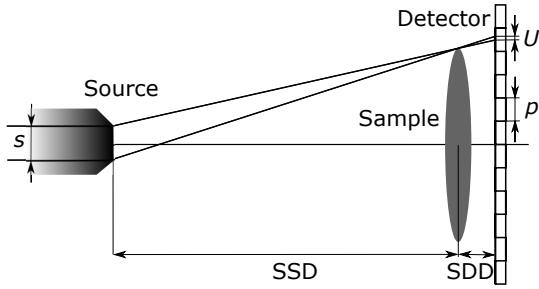


Fig. 2. Formation of geometrical unsharpness U at the detector with linear pixel size p due to finite focal spot size s . SSD stands for source–sample distance, SDD stands for sample–detector distance.

III. MATERIALS AND METHODS

A. CT equipment

PBI was studied on a laboratory-based nCT system RIGAKU Nano3DX (Japan). The machine employs a geometrical arrangement based on a long SSD (Fig. 1b): the SSD is fixed at 260 mm, the SDD can be varied between 0 mm and 50 mm. In this study, two materials of rotating anode were used: Cu and Mo, working at acceleration voltage 40 kV and 50 kV, respectively, with the focal spot size $73 \mu\text{m}$ and $150 \mu\text{m}$, respectively, measured according to EN 12543-5 norm. For further calculations, such as an X-ray wavelength, the corresponding Cu $K\alpha$ line 8 keV or Mo $K\alpha$ line 17 keV were taken. The machine is equipped with an XSight Micron X-ray CCD camera with dimensions of $3300 \text{ px} \times 2500 \text{ px}$ and $0.27 \mu\text{m}$ pixel size. To achieve a larger pixel size, a binning parameter b of value 1, 2, 3, 4, or 8 can be used (signal from $(b \times b)$ px^2 is summed, thus the effective pixel size is larger).

B. CT measurement

A light-element composite made of polyethylene matrix reinforced with 15%–20% of carbon fibres (CFRP) was chosen to demonstrate PBI.

To show the varying amount of edge enhancement, the sample was measured at four different SDDs (Tab. I). For larger distances, bigger pixel sizes were used to avoid geometrical unsharpness. In this way, images for larger SDD are less sharp, but allow to decrease the exposure time and storage place. For each pixel size, 80% (determined to reflect possible variations of real instrument conditions) of the maximum allowed SDD calculated by Eq. 3 was used. Other acquisition parameters (number of projections, exposure time) were adapted according to specified CT machine rules to achieve optimum transmission and to avoid low signal and undersampling. A measurement with linear pixel size (LPS) $0.54 \mu\text{m}$ was also performed at 400% of maximum allowed SDD in order to show the geometrical unsharpness effect. For comparison of different X-ray wavelengths, therefore different degrees of coherence, the sample was also measured with Mo target under same conditions as with Cu target for SDD 1.5 mm. Projections were reconstructed using VGStudio MAX 3.1 reconstruction module.

TABLE I
SUMMARY OF EXPERIMENTAL CONDITIONS OF CFRP MEASUREMENT FOR A DEMONSTRATION OF PBI EFFECT AND VERIFICATION OF GEOMETRICAL UNSHARPNESS RULE DESCRIBED BY EQ. 3. SDD STANDS FOR SAMPLE–DETECTOR DISTANCE, LPS STANDS FOR LINEAR PIXEL SIZE.

Target material	SDD [mm]	Bin	LPS [μm]	Projections	Exposure time [s]
Cu	0.8	1	0.27	1600	25
Cu	1.5	2	0.54	800	9
Cu	3.1	4	1.08	600	2
Cu	6.2	8	2.16	400	0.5
Cu	7.7	2	0.54	800	9
Mo	1.5	2	0.54	800	9

C. Data processing

The Paganin phase retrieval algorithm [50] implemented in the ANKAphase software [51] was used on the data measured with Cu target at the SDD 1.5 mm. The δ/β ratio of values in the index of refraction n ($n = 1 - \delta + i\beta$) was chosen as 780 for polyethylene [52].

The edge enhancement was evaluated on an averaged line profile (pixels in $8 \mu\text{m}$ area above and below the line were averaged to reduce noise). It was specifically evaluated on the edge of air and polymer matrix by calculating absorption contrast value C_{ABS} and phase contrast value C_{PHC} according to [33]:

$$C_{\text{ABS}} = \frac{I_{\text{mat}} - I_{\text{bcg}}}{(I_{\text{mat}} + I_{\text{bcg}})/2},$$

$$C_{\text{PHC}} = \frac{I_{\text{max}} - I_{\text{min}} - (I_{\text{mat}} - I_{\text{bcg}})}{(I_{\text{max}} + I_{\text{min}})},$$

where I_{mat} , I_{bcg} , I_{max} , I_{min} are mean gray values of material and background and maximum and minimum gray values in the line profile, respectively.

IV. RESULTS AND DISCUSSION

A. Theoretical evaluation of conditions for PBI

When performing tomographic experiments in laboratory conditions, change of values of s , λ , p usually requires altering a hardware setup, whereas positions of the source, the sample and the detector can be adjusted more easily. In the case of Nano3DX, it is possible to change the target material. SSD is fixed and only the SDD value can be changed. Therefore, in following paragraphs, the results of calculations are given for different SDDs and target materials.

For identification of the imaging regime, the graph plotting N_F dependence on a feature of interest of size a (Fig. 3) gives information about the approximate size of the structure at which edge effect is pronounced at a given sample–detector distance.

By substituting Eq. 1 into $N_F > 1$ and modifying the equation, we obtain $SDD(a^2 - \lambda SSD) > -a^2 SSD$. From here, for $a > (\lambda SSD)^{1/2}$, the condition is always fulfilled since the right side of the equation is negative. Value of $(\lambda SSD)^{1/2}$ is $6 \mu\text{m}$ for Cu and $4 \mu\text{m}$ for Mo target. The smallest features that can be distinguished must have a minimum size of two pixels, which is $0.54 \mu\text{m}$ for the smallest pixel size, or larger. Therefore, the imaging can be considered almost always in the near-field regime, except the very small details measured with the highest possible resolution. For large structures, where $N_F \gg 1$, the effect of X-ray propagation becomes insignificant and the resulting images reflect only the absorption of the sample.

The ratio L_{shear}/L_{lat} determining the coherence degree of X-ray is plotted in Fig. 4. The coherence requirements have a high restriction on PBI since Eq. 2 is strictly fulfilled only for structures larger than about $5 \mu\text{m}$ for Cu and $10 \mu\text{m}$ for Mo target, depending on SDD. For rather small structures, the degree of coherency is decreased and phase effects will be less pronounced.

The maximum values of SDD to avoid the unsharpness according to Eq. 3 are shown in Tab. II for different linear pixel sizes (LPS). For example, in case of measuring with LPS $0.27 \mu\text{m}$, SDD should not exceed 1.0 mm for Cu and 0.4 mm for Mo. This condition must be verified before the beginning of every measurement. To improve contrast between materials, it is possible to increase the SDD to get a more pronounced phase contrast effect even at the cost of the reduced resolution.

Using Eq. 1–3, it is always possible to determine the highest possible SDD and estimate, which structure sizes will have edge enhancement fringes visible.

B. Imaging of CFRP samples

In general, tomographic slices of CFRP (Fig. 7) show a strong edge enhancement at borders between the sample and the air. It might also be observed at carbon fibres to a much lesser extent. When the SDD increases, the edge enhancement

TABLE II
CALCULATION OF MAXIMUM SAMPLE–DETECTOR DISTANCES (SDDs, IN MM) WHICH ARE ALLOWED TO AVOID GEOMETRICAL UNSHARPNESS FOR DIFFERENT LINEAR PIXEL SIZES (LPSs) ACCORDING TO EQ. 3.

Target \ LPS [μm]	0.27	0.54	1.08	2.16
Cu	1.0	1.9	3.8	7.7
Mo	0.4	0.9	1.8	3.6

becomes stronger and phase contrast increases, while absorption contrast does not change so rapidly (Fig. 9). Since an increase of SDD is possible only with an increase of the pixel size to fulfil the condition on geometrical unsharpness given by Eq. 3, the resolution becomes lower and some small details of the sample are no longer visible. Therefore, the calculated increase of phase contrast is slightly underestimated.

For all SDDs, the imaging is in near-field regime according to Fig. 3. The fibres have $6\text{--}8 \mu\text{m}$ in diameter. The lateral dimension of the whole sample is about $600 \mu\text{m}$ and the size of air voids in the sample is in range of $50\text{--}200 \mu\text{m}$. For all these intervals $N_F > 1$, so none of those features is in a holographic regime.

When SDD is set too big and therefore it does not fulfil the condition of geometrical unsharpness (Eq. 3), the image is blurred. For example, CFRP measured with LPS $0.54 \mu\text{m}$ at 400% of the maximum allowed SDD (Fig. 8b) is more blurred than the same sample at 80% of the maximum SDD (Fig. 8a). This confirms that the geometrical unsharpness must be taken into account whenever a laboratory cone-beam X-ray source is used.

Measurement of CFRP with a different target material, and therefore the characteristic wavelength, was made with Mo target (Fig. 5). In the applied setup, Mo target has a larger spot size than Cu target, therefore the maximum allowed distances due to geometrical unsharpness are, in general, lower. Although in this case, the SDD exceeds this distance, it was used for the experiment to have the comparison with Cu target under the same conditions (Fig. 7b).

The histograms of both data have a similar shape (Figs. 10 and 11) exhibiting only one peak. The contrast between structures with similar density (PE matrix and C fibres) is worse for Mo target. Naturally, this is an expected result since higher energy was used resulting in lower contrast for such light materials. Edge enhancement at matrix/air interface is still present, but to a lesser extent (edge profiles at Fig. 10 compared to Fig. 11). This is evident also from values of calculated phase contrast: $C_{PHC} = 0.152$ for Cu target and $C_{PHC} = 0.071$ for Mo target. It can be explained by the lower degree of partial coherence of X-rays emitted from Mo target than from Cu target.

By an application of the phase retrieval on tomographic data (Fig. 6), the edge enhancement was reduced compared to the original data (Fig. 7b) as it is shown on the edge profile (Fig. 11). The absorption contrast increased ($C_{ABS} = 0.004$ for original data, $C_{ABS} = 0.366$ with phase retrieval) and the phase contrast decreased ($C_{PHC} = 0.152$ for original data, $C_{PHC} = 0.139$ with phase retrieval), which is very convenient for material segmentation.

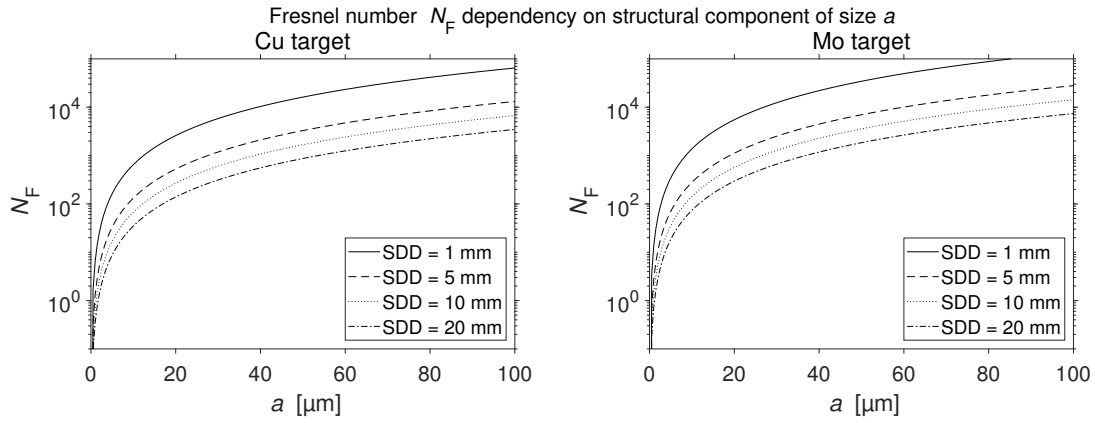


Fig. 3. Analysis of conditions for near-field imaging for different sample–detector distances (SDD) according to the Eq. 1. The imaging is not in near-field regime for $N_F \ll 1$.

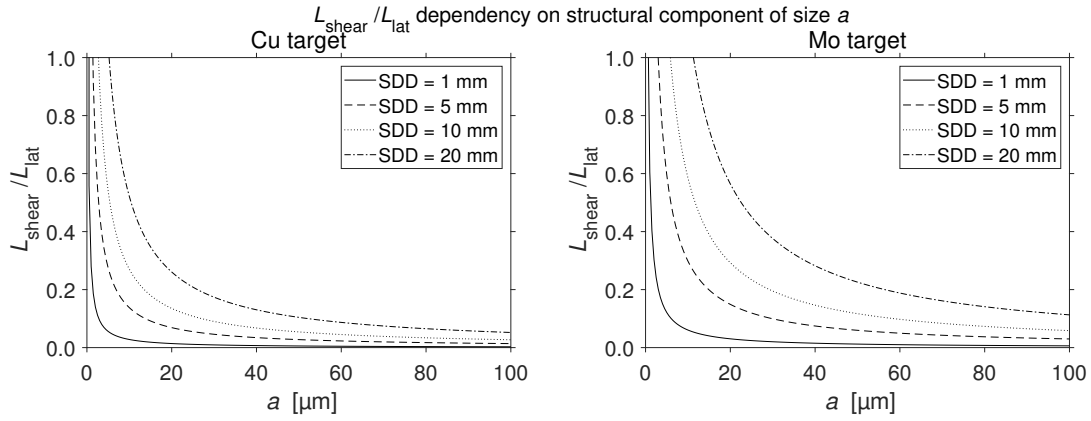


Fig. 4. Analysis of coherence requirements and for different sample–detector distances (SDDs) according to the Eq. 2. The degree of X-ray coherence is high enough to observe phase effects at structures of given size a for $L_{\text{shear}}/L_{\text{lat}} < 1$.

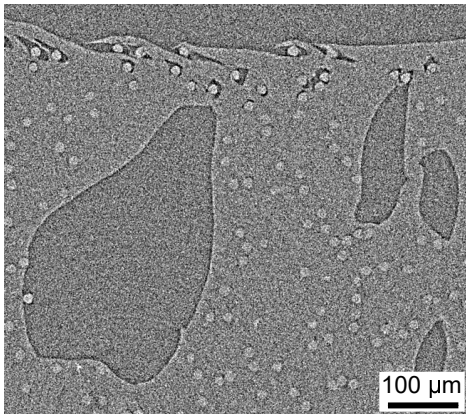


Fig. 5. Tomographic slice of CFRP sample measured with linear pixel size (LPS 0.54 μm) at source–detector distance 1.5 mm with Mo target.

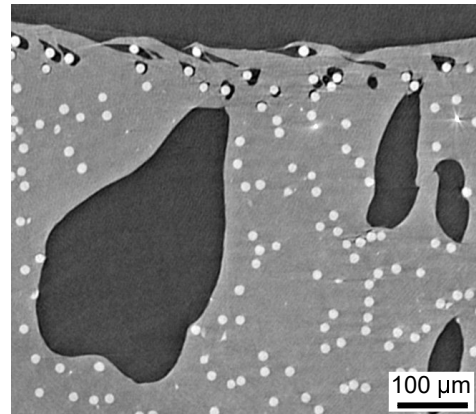


Fig. 6. Tomographic slice of the CFRP sample. Phase retrieval is applied on the data measured with Cu target at the SDD 1.5 mm (reconstruction without phase retrieval is in Fig. 7b).

The histogram (Fig. 11) contains several peaks corresponding to different structures and allowing the segmentation of different parts (air, matrix and carbon fibres). Without the phase retrieval, the histogram of data has only one peak which makes segmentation very challenging. This is the reason

why it is sometimes useful to apply the algorithm also on data without any strong visible edge enhancement, a further analysis is easier on these data from the image processing point of view.

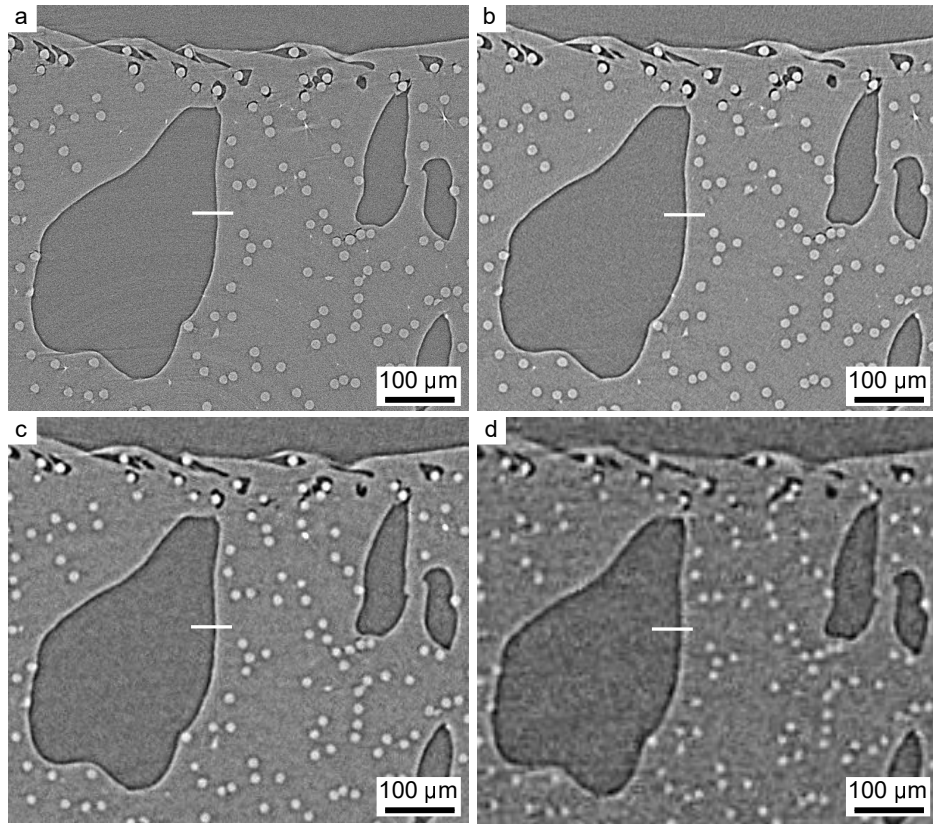


Fig. 7. Tomographic slice of CFRP sample measured at different sample–detector distances (SDD) with different linear pixel sizes (LPS) according to Tab. I: a) SDD 0.8 mm, LPS 0.27 μm , b) SDD 1.5 mm, LPS 0.54 μm , c) SDD 3.1 mm, LPS 1.08 μm , d) SDD 6.2 mm, LPS 2.16 μm . The line was used for generation of edge profiles in Fig. 9.

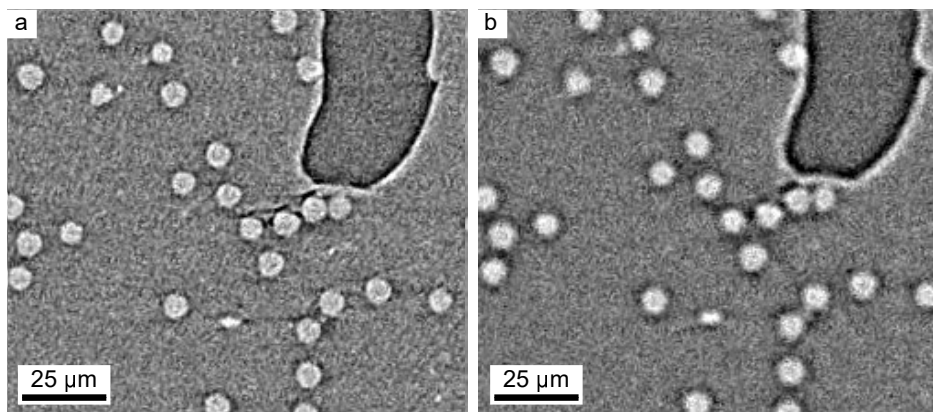


Fig. 8. Tomographic slice of CFRP sample measured with linear pixel size (LPS 0.54 μm) at source–detector distances (SDD) a) 1.5 mm, b) 7.7 mm. For this LPS, SDD 7.7 mm does not fulfil Eq. 3 and in contrast with SDD 1.5 mm, the structures are blurred.

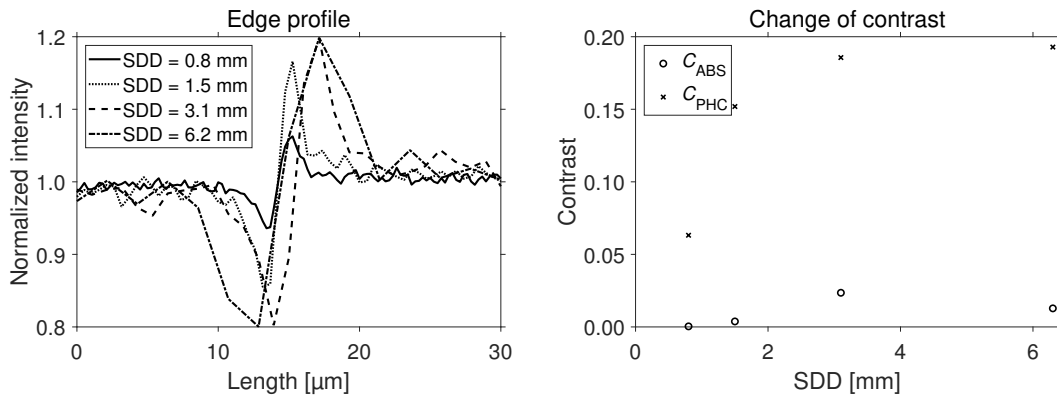


Fig. 9. Averaged line profiles normalized by mean value over air-polymer edge marked in Fig. 7 and absorption (C_{ABS}) and phase contrast (C_{PHC}) for different sample-detector distances (SDD).

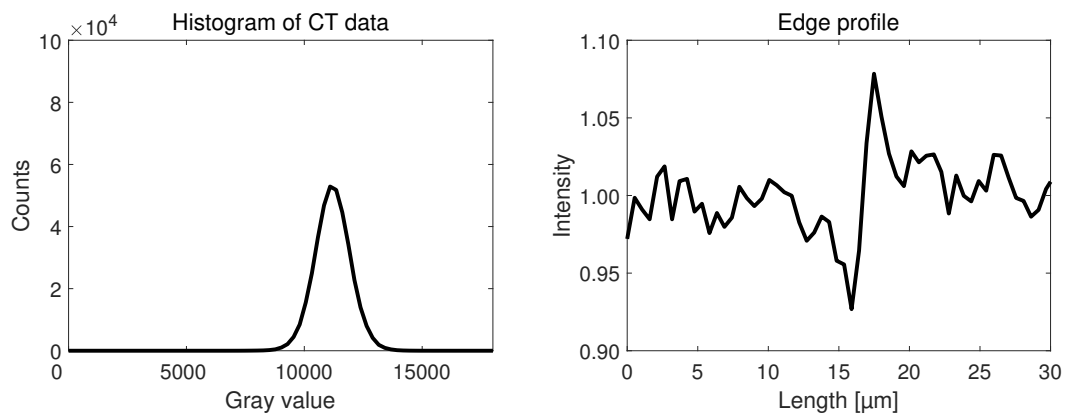


Fig. 10. Image evaluation of a tomographic slice of the CFRP sample from Fig. 5: averaged edge profile and histogram.

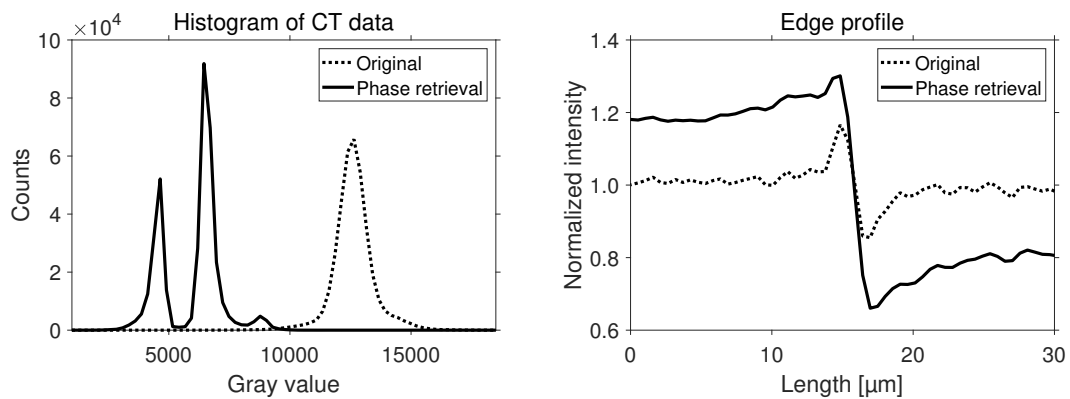


Fig. 11. Image evaluation of tomographic slices of the CFRP sample from Fig. 7b and Fig. 6. Averaged edge profile and histogram are used to show the influence of phase retrieval on CT data.

V. CONCLUSION

Phase contrast imaging extends possibilities of X-ray computed nanotomography to imaging of materials consisting of light elements with low X-ray absorption, such as biological or polymeric samples. The propagation-based imaging is a very popular method of PCI because it does not demand any extra hardware setup and it is easily available on laboratory-based CT systems.

In this paper, a method for evaluation of the capability of a laboratory-based CT system of PBI is summarized. It is based on a combination of three criteria - an imaging regime, a degree of coherency and geometrical unsharpness. By using these principles, it is possible to determine specific settings of the CT system where PBI regime is available.

The method is demonstrated on measurements of carbon fibre reinforced polymer by the nCT system. A capability of the system for PBI was tested at various critical settings. The quality of results is evaluated based on edge enhancement analysis. A phase retrieval was applied to the measured data to emphasize the advantages of the propagation-based imaging for image quality improvement.

This evaluation method proved capable of estimating the suitability of a CT device for PBI using knowledge of machine parameters. It is a useful tool for researchers developing X-ray phase contrast imaging techniques with a laboratory-based CT system.

REFERENCES

- [1] P. J. Withers, "X-ray nanotomography," *Materials Today*, vol. 10, no. 12, pp. 26–34, 2007.
- [2] L. De Chiffre, S. Carmignato, J. P. Kruth, R. Schmitt, and A. Weckenmann, "Industrial applications of computed tomography," *CIRP Annals - Manufacturing Technology*, vol. 63, no. 2, pp. 655–677, 2014.
- [3] M. Kampschulte, A. Langheinrich, J. Sender, H. Litzlbauer, U. Althöhn, J. Schwab, E. Alexandre-Lafont, G. Martels, and G. Krombach, "Nano-Computed Tomography: Technique and Applications," *RöFo - Fortschritte auf dem Gebiet der Röntgenstrahlen und der bildgebenden Verfahren*, vol. 188, no. 02, pp. 146–154, 2016.
- [4] S.-A. Zhou and A. Brahme, "Development of phase-contrast X-ray imaging techniques and potential medical applications," *Physica Medica*, vol. 24, no. 3, pp. 129–148, 2008.
- [5] O. Betz, U. Wegst, D. Weide, M. Heethoff, L. Helfen, W.-K. Lee, and P. Cloetens, "Imaging applications of synchrotron X-ray phase-contrast microtomography in biological morphology and biomaterials science. I. General aspects of the technique and its advantages in the analysis of millimetre-sized arthropod structure," *Journal of Microscopy*, vol. 227, no. 1, pp. 51–71, 2007.
- [6] P. Miao, Z. Wu, M. Li, Y. Ji, B. Xie, X. Lin, and G.-Y. Yang, "Synchrotron Radiation X-Ray Phase-Contrast Tomography Visualizes Microvasculature Changes in Mice Brains after Ischemic Injury," *Neural Plasticity*, vol. 2016, pp. 1–8, 2016.
- [7] J. J. Socha, M. W. Westneat, J. F. Harrison, J. S. Waters, and W.-K. Lee, "Real-time phase-contrast x-ray imaging: a new technique for the study of animal form and function," *BMC Biology*, vol. 5, no. 1, p. 6, 2007.
- [8] J. Kaiser, M. Holá, M. Galiová, K. Novotný, V. Kanický, P. Martinec, J. Ščučka, F. Brun, N. Sodini, G. Tromba, L. Mancini, and T. Kořistková, "Investigation of the microstructure and mineralogical composition of urinary calculi fragments by synchrotron radiation X-ray microtomography: a feasibility study," *Urological Research*, vol. 39, no. 4, pp. 259–267, 2011.
- [9] F. Cosmi, A. Bernasconi, and N. Sodini, "Phase contrast microtomography and morphological analysis of a short carbon fibre reinforced polyamide," *Composites Science and Technology*, vol. 71, no. 1, pp. 23–30, 2011.
- [10] B. Yu, R. S. Bradley, C. Soutis, and P. J. Withers, "A comparison of different approaches for imaging cracks in composites by X-ray microtomography," *Philosophical Transactions of the Royal Society A: Mathematical, Physical and Engineering Sciences*, vol. 374, no. 2071, p. 20160037, 2016.
- [11] S. Garcea, Y. Wang, and P. Withers, "X-ray computed tomography of polymer composites," *Composites Science and Technology*, vol. 156, pp. 305–319, 2018.
- [12] J. Baruchel, Ed., *X-Ray Tomography in Material Science*. Herms Science, 2000.
- [13] A. Yoneyama, A. Momose, I. Koyama, E. Seya, T. Takeda, Y. Itai, K. Hirano, and K. Hyodo, "Large-area phase-contrast X-ray imaging using a two-crystal X-ray interferometer," *Journal of Synchrotron Radiation*, vol. 9, no. 5, pp. 277–281, 2002.
- [14] A. Momose, T. Takeda, Y. Itai, A. Yoneyama, and K. Hirano, "Phase-Contrast Tomographic Imaging Using an X-ray Interferometer," *Journal of Synchrotron Radiation*, vol. 5, no. 3, pp. 309–314, 1998.
- [15] T. J. Davis, D. Gao, T. E. Gureyev, A. W. Stevenson, and S. W. Wilkins, "Phase-contrast imaging of weakly absorbing materials using hard X-rays," *Nature*, vol. 373, no. 6515, pp. 595–598, 1995.
- [16] D. Chapman, W. Thomlinson, R. E. Johnston, D. Washburn, E. Pisano, N. Gmür, Z. Zhong, R. Menk, F. Arfelli, and D. Sayers, "Diffraction enhanced x-ray imaging," *Physics in Medicine and Biology*, vol. 42, no. 11, pp. 2015–2025, 1997.
- [17] Z. Wang, P. Zhu, W. Huang, Q. Yuan, X. Liu, K. Zhang, Y. Hong, H. Zhang, X. Ge, K. Gao, and Z. Wu, "Quantitative coherence analysis with an X-ray Talbot-Lau interferometer," *Analytical and Bioanalytical Chemistry*, vol. 397, no. 6, pp. 2091–2094, 2010.
- [18] J. Tanaka, M. Nagashima, K. Kido, Y. Hoshino, J. Kiyohara, C. Makifuchi, S. Nishino, S. Nagatsuka, and A. Momose, "Cadaveric and in vivo human joint imaging based on differential phase contrast by X-ray Talbot-Lau interferometry," *Zeitschrift für Medizinische Physik*, vol. 23, no. 3, pp. 222–227, 2013.
- [19] Z. Wang, K. Gao, P. Zhu, Q. Yuan, W. Huang, K. Zhang, Y. Hong, X. Ge, and Z. Wu, "Grating-based X-ray phase contrast imaging using polychromatic laboratory sources," *Journal of Electron Spectroscopy and Related Phenomena*, vol. 184, no. 3–6, pp. 342–345, 2011.
- [20] A. Tkachuk, F. Duerwer, H. Cui, M. Feser, S. Wang, and W. Yun, "X-ray computed tomography in Zernike phase contrast mode at 8 keV with 50-nm resolution using Cu rotating anode X-ray source," *Zeitschrift für Kristallographie - Crystalline Materials*, vol. 222, no. 11/2007, 2007.
- [21] M. D. de Jonge, B. Hornberger, C. Holzner, D. Legnini, D. Paterson, I. McNulty, C. Jacobsen, and S. Vogt, "Quantitative Phase Imaging with a Scanning Transmission X-Ray Microscope," *Physics Review Letters*, vol. 100, no. 16, p. 163902, 2008.
- [22] A. S. Kumar, P. Mandal, Y. Zhang, and S. Litster, "Image segmentation of nanoscale Zernike phase contrast X-ray computed tomography images," *Journal of Applied Physics*, vol. 117, no. 18, p. 183102, 2015.
- [23] X. Wu and H. Liu, "Clarification of aspects in in-line phase-sensitive x-ray imaging," *Medical Physics*, vol. 34, no. 2, pp. 737–743, 2007.
- [24] S. Mohammadi, E. Larsson, F. Alves, S. Dal Monego, S. Biffi, C. Garrovo, A. Lorenzon, G. Tromba, and C. Dullin, "Quantitative evaluation of a single-distance phase-retrieval method applied on in-line phase-contrast images of a mouse lung," *Journal of Synchrotron Radiation*, vol. 21, no. 4, pp. 784–789, 2014.
- [25] A. Burvall, U. Lundström, P. A. C. Takman, D. H. Larsson, and H. M. Hertz, "Phase retrieval in X-ray phase-contrast imaging suitable for tomography," *Optics Express*, vol. 19, no. 11, p. 10359, 2011.
- [26] R. C. Chen, L. Rigon, and R. Longo, "Comparison of single distance phase retrieval algorithms by considering different object composition and the effect of statistical and structural noise," *Optics Express*, vol. 21, no. 6, p. 7384, 2013.
- [27] M. Langer, P. Cloetens, J.-P. Guigay, and F. Peyrin, "Quantitative comparison of direct phase retrieval algorithms in in-line phase tomography," *Medical Physics*, vol. 35, no. 10, pp. 4556–4566, 2008.
- [28] R. S. Bradley, A. McNeil, and P. J. Withers, "An examination of phase retrieval algorithms as applied to phase contrast tomography using laboratory sources," in *Proc. SPIE*, S. R. Stock, Ed., 2010, p. 780404.
- [29] X. Wu, H. Liu, and A. Yan, "Phase-contrast X-ray tomography: Contrast mechanism and roles of phase retrieval," *European Journal of Radiology*, vol. 68, no. 3, pp. S8–S12, 2008.
- [30] M. Töpferwien, M. Krenkel, F. Quade, and T. Salditt, "Laboratory-based x-ray phase-contrast tomography enables 3D virtual histology," in *Advances in Laboratory-based X-Ray Sources, Optics, and Applications V*, A. M. Khounsary and G. E. van Dorsen, Eds., vol. 9964. SPIE, 2016, p. 99640I.

- [31] A. Momose, "Recent Advances in X-ray Phase Imaging," *Japanese Journal of Applied Physics*, vol. 44, no. 9A, pp. 6355–6367, 2005.
- [32] S. W. Wilkins, T. E. Gureyev, D. Gao, A. Pogany, and A. W. Stevenson, "Phase-contrast imaging using polychromatic hard X-rays," *Nature*, vol. 384, p. 335, 1996.
- [33] J. Kastner, B. Plank, and G. Requena, "Non-destructive characterisation of polymers and Al-alloys by polychromatic cone-beam phase contrast tomography," *Materials Characterization*, vol. 64, pp. 79–87, 2012.
- [34] S. C. Mayo, A. W. Stevenson, and S. W. Wilkins, "In-Line Phase-Contrast X-ray Imaging and Tomography for Materials Science," *Materials*, vol. 5, no. 12, pp. 937–965, 2012.
- [35] S. Mayo, A. Stevenson, S. Wilkins, D. C. Gao, S. Mookhoek, S. Meure, T. Hughes, and J. Mardel, "X-Ray Phase-Contrast Tomography for Quantitative Characterisation of Self-Healing Polymers," *Materials Science Forum*, vol. 654-656, pp. 2322–2325, 2010.
- [36] M. Krenkel, M. Töpperrwien, C. Dullin, F. Alves, and T. Salditt, "Propagation-based phase-contrast tomography for high-resolution lung imaging with laboratory sources," *AIP Advances*, vol. 6, no. 3, p. 035007, 2016.
- [37] C. M. Laperle, T. J. Hamilton, P. Wintermeyer, E. J. Walker, D. Shi, M. A. Anastasio, Z. Derdak, J. R. Wands, G. Diebold, and C. Rose-Petrucci, "Low density contrast agents for x-ray phase contrast imaging: the use of ambient air for x-ray angiography of excised murine liver tissue," *Physics in Medicine and Biology*, vol. 53, no. 23, pp. 6911–6923, 2008.
- [38] M. Bartels, V. H. Hernandez, M. Krenkel, T. Moser, and T. Salditt, "Phase Contrast Tomography of the Mouse Cochlea at Microfocus X-Ray Sources," *Applied Physics Letters*, vol. 103, no. 8, p. 83703, 2013.
- [39] Y. S. Kashyap, P. Yadav, T. Roy, P. Sarkar, M. Shukla, and A. Sinha, "Laboratory-based X-ray phase-contrast imaging technique for material and medical science applications," *Applied Radiation and Isotopes*, vol. 66, no. 8, pp. 1083–1090, 2008.
- [40] A. Pogany, D. Gao, and S. W. Wilkins, "Contrast and resolution in imaging with a microfocus x-ray source," *Review of Scientific Instruments*, vol. 68, no. 7, pp. 2774–2782, 1997.
- [41] Y. I. Nesterets, S. W. Wilkins, T. E. Gureyev, A. Pogany, and A. W. Stevenson, "On the optimization of experimental parameters for x-ray in-line phase-contrast imaging," *Review of Scientific Instruments*, vol. 76, no. 9, 2005.
- [42] T. E. Gureyev, Y. I. Nesterets, A. W. Stevenson, P. R. Miller, A. Pogany, and S. W. Wilkins, "Some simple rules for contrast, signal-to-noise and resolution in in-line x-ray phase-contrast imaging," *Optics Express*, vol. 16, no. 5, p. 3223, 2008.
- [43] A. Balles, S. Zabler, T. Ebersperger, C. Fella, and R. Hanke, "Propagator based formalism for optimizing in-line phase contrast imaging in laboratory X-ray setups," *Review of Scientific Instruments*, vol. 87, no. 9, 2016.
- [44] D. Paganin, *Coherent X-Ray Optics*. Oxford University Press, 2006.
- [45] F. Ouardji, E. Potter, W. R. Chen, and H. Liu, "<title>Impact of focal spot size on the spatial resolution of a digital x-ray imaging system for small-animal studies</title>," in *Proc. SPIE, T. Vo-Dinh, D. A. Benaron, and W. S. Grundfest, Eds., 2002*, pp. 109–116.
- [46] E. L. Ritman, "Micro-Computed Tomography Current Status and Developments," *Annual Review of Biomedical Engineering*, vol. 6, no. 1, pp. 185–208, 2004.
- [47] B. D. Arhatari and a. G. Peele, "Optimisation of phase imaging geometry," *Optics express*, vol. 18, no. 23, pp. 23727–39, 2010.
- [48] M. Reichardt, T. Salditt, M. Toepferwien, J. Frohn, F. Alves, A. Markus, and J.-D. Nicolas, "Nanoscale holographic tomography of heart tissue with x-ray waveguide optics," in *Developments in X-Ray Tomography XI*, B. Müller and G. Wang, Eds. SPIE, 2017, p. 4.
- [49] M. Töpperrwien, M. Krenkel, D. Vincenz, F. Stöber, A. M. Oelschlegel, J. Goldschmidt, and T. Salditt, "Three-dimensional mouse brain cytoarchitecture revealed by laboratory-based x-ray phase-contrast tomography," *Scientific Reports*, vol. 7, no. July 2016, pp. 1–8, 2017.
- [50] D. Paganin, S. C. Mayo, T. E. Gureyev, P. R. Miller, and S. W. Wilkins, "Simultaneous phase and amplitude extraction from a single defocused image of a homogeneous object," *Journal of Microscopy*, vol. 206, no. 1, pp. 33–40, 2002.
- [51] T. Weitkamp, D. Haas, D. Wegrzynek, and A. Rack, "ANKAphase : software for single-distance phase retrieval from inline X-ray phase-contrast radiographs," *Journal of Synchrotron Radiation*, vol. 18, no. 4, pp. 617–629, 2011.
- [52] J. Taylor, "X-Ray Complex Refraction Coefficient," *CSIRO CSS eToolbox Home*, 2015. [Online]. Available: ts-imaging.net/Services/Simple/ICUtilXdata.aspx



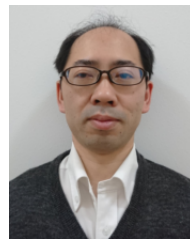
Dominika Kalasová was born in 1992. She received her M.Sc. degree from Brno University of Technology, Czech Republic, in 2016. She is currently a Ph.D. candidate at Brno University of Technology under the supervision of Professor Jozef Kaiser. Her main focus is imaging of soft materials by X-ray computed tomography.



Tomáš Zikmund was born in 1984. He received his M.Sc. and Ph.D. degrees from Brno University of Technology, Brno, Czech republic, in 2008 and 2014, respectively. He is the head of the Laboratory of X-ray micro and nano Computed Tomography at CEITEC BUT. His research interest is focused on X-ray computed tomography and image processing of soft tissue (cartilage tissue, mouse brain, bile duct system in liver, bio-degradable composites, stem cells) and correlations of 2D imaging techniques with 3D data of X-ray Computed tomography.



Ladislav Pina was born in 1946. He received M.Sc. and Ph.D. degrees from the Faculty of Nuclear Sciences and Physical Engineering, Czech Technical University in Prague, in 1972 and 1978, respectively. From 1980 to 1981, he was on a study stay at the Department of Pure and Applied Physics of the Queen's University of Belfast which included experimental work using ion and X-ray diagnostics of laser plasma in Rutherford Appleton Laboratory. In 1983, he started to work with the Department of Physical Electronics as A. Professor and has been teaching electricity and magnetism, quantum electronics and X-ray physics. He supervises MSc. and Ph.D. students. His research interests include physics of generation, detection and imaging in EUV to X-ray radiation bands. A.Prof. Pina is a member of SPIE.



Yoshihiro Takeda was born in 1979. He received the B.Sc. and M.Sc. from Osaka Prefecture University, Osaka, Japan, in 2002 and 2004, and the Ph.D. degree from Tsukuba University, Ibaragi, in 2007. From 2007 to 2008, he was a postdoctoral fellow with Graduate School of Frontier Sciences, the University of Tokyo, Tokyo, Japan. At 2008 he was a Specially Appointed Assistant Professor with Keio University School of Medicine. Currently he is a researcher of X-ray research laboratory of Rigaku corporation. His research interests include X-ray phase imaging and X-ray computed tomography.



Martin Horváth was born in 1970. He received M.Sc. and Ph.D. degrees from the Charles University, Prague, the Czech Republic, in 1994 and 2002, respectively. From 1999 to 2008, he was a development scientist in Reflex s.r.o., Prague. From 2008, he works as a development scientist in Rigaku Innovative Technologies Europe, s.r.o. His research interests include design and development of X-ray detectors.



Kazuhiko Omote received Ph.D. degrees in engineering from the University of Nagoya in 1991. He works as a general manager in X-Research Laboratory, Rigaku Corporation. He has developed a lot of instruments and software for X-ray analysis of Rigaku Corporation. His research interests include structural analysis of thin films and nanomaterials, X-ray diffraction/scattering theory, and X-ray optics.



Jozef Kaiser was born in 1974. He received his M.Sc. and Ph.D. degrees from Brno University of Technology, Brno, Czech Republic, in 1997 and 2001, respectively. In 2013, he was promoted to professor at Brno University of Technology. He absolved long term internships at the University of Pcs, Hungary (1998-2001); University of Orleans, France (2003); University of LAquila, Italy (2006) and several short term research stays at Synchrotron Elettra in Trieste, Italy (2005-2014). Currently, he is the Research Group Leader of Materials Characterization and Advanced Coatings group. His research activity is aimed on laser-based analytical methods (LIBS, LA-ICP methods, and Raman spectroscopy) and X-Ray computed tomography. He is also focused on the development of high-end LIBS instrumentation and the technology transfer of LIBS technology to industry.

Correlation of X-ray Computed Nanotomography and Scanning Electron Microscopy Imaging of Collagen Scaffolds

Dominika Kalasová^{1,*}, Veronika Pavliňáková¹, Tomáš Zikmund¹, Lucy Vojtová¹ and Jozef Kaiser¹.

¹. CEITEC - Central European Institute of Technology, Brno University of Technology, Brno, Czech Republic

* Corresponding author, dominika.kalasova@ceitec.vutbr.cz

Many tissue engineering approaches involve an application of 3D scaffolds. Numerous scaffolds produced from a variety of biomaterials (collagen, chitosan, elastin, etc.) are used in many fields to regenerate different tissues and organs such as bones [1] and for cartilage and cardiovascular repair [2]. As an example, the collagen is a popular extracellular matrix of molecules of connective tissues because of its abundance, biodegradability, and biocompatibility [3]. The morphology of porous scaffolds is usually observed using scanning electron microscopy (SEM). X-ray computed nanotomography (nCT) imaging is a technique enabling a 3D investigation of scaffold's structure and thus a quantification of cell's and scaffold's characteristics such as their size, 3D distribution, porosity, thickness etc. [4, 5].

In the present study, the collagen scaffold structure was observed using a nCT RIGAKU Nano3DX and a SEM Tescan MIRA3. These two machines have completely different geometrical arrangements. To be able to locate the same region of interest of the sample in both nCT and SEM measurements, a sample holder compatible with nCT and SEM had to be manufactured. Consequently, the sample didn't have to be removed from the holder during measurements on either machine. The sample holder was designed as a rounded bar split in two parts (Fig. 1). The upper part (12 mm height) allows fastening the sample to the MIRA3, whereas the entire sample holder allows fastening the sample to the Nano3DX (Fig. 2). For an easy dismantling, the upper part is connected by M2 set screw and can be demounted easily by bare hands. Both parts of the holder are made of stainless steel grade 1.4305 (AISI 303). This grade was chosen for its good temperature stability and excellent machinability.

To locate precisely the same regions of interest, e.g. cells on scaffold, it is advantageous that the marker is placed on a sample and easily recognizable in both measurement methods. A test of several markers was performed to select the best one for both nCT and SEM. Tested materials were red and silver nail polish, carbon tape, carbon tape with pieces of aluminium foil, and handle tape. All of these were applied to the collagen scaffold and imaged with a light microscope (LM), SEM and nCT (Fig. 3). nCT data were processed in VGSTUDIO MAX 3.1 software and the markers were segmented and rendered in 3D (Fig. 3 bottom left). For the comparison of 3D nCT and 2D LM and SEM, the surface of the sample was rendered in the nCT data to obtain a similar view as in the SEM and LM.

All markers containing metals (aluminium foil, handle tape) caused noticeable metal artefacts, which strongly decreased quality of nCT data (Fig. 3, nCT slice 2). Carbon tape does not have such a contrast at SEM as nail polish. Eventually, silver nail polish was chosen as the best marker, because of its easy detection and no artefacts in both nCT and SEM.

The proper matching of SEM and nCT data by the use of a sample holder and a suitable marker allows to confirm the position of the cells within the scaffold. In this way of material's determination in nCT data, it will be possible to study cell's distribution within scaffold and determine its characteristics such as

volume, 3D distribution or amount of proliferation [6].

References:

[1] E. Prosecká *et al*, J. Biomed. Mater. Res. A **99A** (2011) 307.
 [2] Ch. Bermueller *et al*, Tissue Eng. Pt. A **19** (2013) 2201.
 [3] J. Glowacki and S. Mizuno, Biopolymers **89** (2008) 338.
 [4] K. Brockdorf *et al*, Microsc. Microanal. **13** (2007) 1572.
 [5] R. S. Bradley *et al*, Macromol. Biosci. **17** (2017) 1600236.
 [6] This research has been financially supported by the MEYS CR under the project CEITEC 2020 (LQ1601) and CEITEC Nano Research Infrastructure (MEYS CR, 2016–2019), and TACR (TJ01000382).

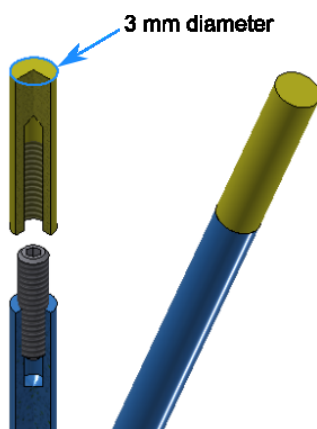


Figure 1. SEM-nCT holder for samples. The upper (yellow) part can be unscrewed and inserted into microscope.

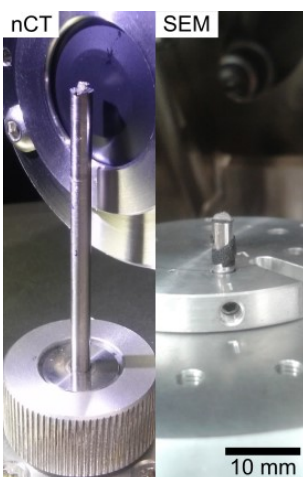


Figure 2. SEM-nCT holder for samples in nCT and SEM.

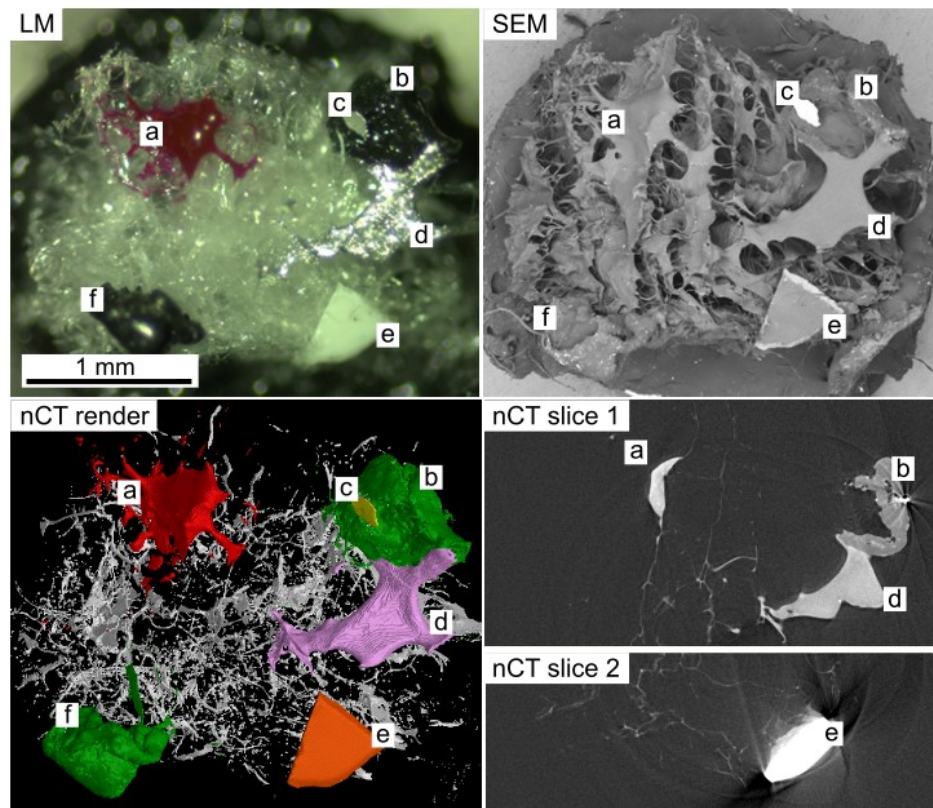
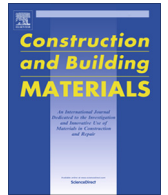


Figure 3. Test of makers for correlation of light microscopy (LM), scanning electron microscopy (SEM) and X-ray computed nanotomography (nCT). Selected markers are applied on the collagen scaffold: a) red nail polish, b) carbon tape + c) piece of aluminum film, d) silver nail polish, e) handle tape, f) carbon tape. All images have the same scale.



Contents lists available at ScienceDirect

Construction and Building Materials

journal homepage: www.elsevier.com/locate/conbuildmat

Characterization of inner structure of limestone by X-ray computed sub-micron tomography



Dominika Kalasová^{a,*}, Karel Dvořák^b, Marek Slobodník^c, Dalibor Všíanský^c, Tomáš Zikmund^a, Jiří Dluhoš^d, Rostislav Váňa^d, Jaroslav Bureš^b, Jozef Kaiser^a

^a CEITEC – Central European Institute of Technology, Brno University of Technology, Purkyňova 123, 612 00 Brno, Czech Republic

^b Faculty of Civil Engineering, Brno University of Technology, Veverí 331/95, 602 00 Brno, Czech Republic

^c Department of Geological Sciences, Faculty of Science, Masaryk University, Kotlářská 2, 611 37 Brno, Czech Republic

^d TESCAN Brno, s.r.o., Libušina třída 1, 62300 Brno, Czech Republic

HIGHLIGHTS

- X-ray computed tomography (CT) is used to visualize limestone inner structure.
- Limestone containing coarser cement of calcite with fluid inclusions is studied.
- Characterization of material is performed by classical petrographic methods.
- 3D distribution of fluid inclusions and air voids in volume is shown by CT.
- CT data are correlated with light microscopy and 3D EDS analysis using FIB-SEM.

ARTICLE INFO

Article history:

Received 7 November 2017

Received in revised form 16 April 2018

Accepted 17 April 2018

Available online 25 April 2018

Keywords:

Limestone

Petrography

X-ray computed tomography

Fluid inclusions

Microthermometry

ABSTRACT

Limestones are fundamental industrial and building materials. Sparry calcite as a principal petrographic component of limestones can contain fluid inclusions. A certain amount of fluid inclusions directly influences decrepitation which plays an important role in decarbonisation processes.

In this paper, a limestone with a high content of fluid inclusions and carbon was investigated. Presence of chlorine and alcaic elements was confirmed with microthermometry, mineralogical and chemical analyses. X-ray computed tomography with sub-micron resolution (CT) was applied to obtain a 3D distribution of cavities. CT data were correlated with some light microscopy images and also with the same sample's tomography data which were gathered using the 3D X-ray energy dispersive spectroscopy (3D EDS) by a scanning electron microscope equipped with a focused ion beam (FIB-SEM). The latter further determined dolomites and metals in the CT data of limestone.

© 2018 Elsevier Ltd. All rights reserved.

1. Introduction

Limestone is a very important industrial rock and a raw material. It is used for the production of lime and cement and also serves as a desulphurization of flue gases of large energy sources. It is also used as a filler in the manufacture of paper with high white balance requirements, in the chemical industry and, last but not least, as a fertilizer. Limestones occur in various sedimentary basin environments, hence they differ in their geological age, crystallinity, petrographic structure, chemical purity and in the porous structure as a result of lithofacial conditions. All of these properties influence not only their behaviour during firing process but also the reactivity with acids in the process of mutual reactions. Many scientific works have been focused on finding and describing the relationship of limestone properties to their behaviour [1–3].

In the process of firing of limestones, some volumetric changes occur, which significantly affects the decarbonation process, especially in shaft kilns. There is only a very small number of publications dealing with this issue and searching for some more general dependence of the limestone properties on their volume changes during firing. Wolter et al. carried out a relatively extensive study in this area on 21 limestone samples [4]. However, the available

tary basin environments, hence they differ in their geological age, crystallinity, petrographic structure, chemical purity and in the porous structure as a result of lithofacial conditions. All of these properties influence not only their behaviour during firing process but also the reactivity with acids in the process of mutual reactions. Many scientific works have been focused on finding and describing the relationship of limestone properties to their behaviour [1–3].

* Corresponding author.

E-mail addresses: dominika.kalasova@ceitec.vutbr.cz (D. Kalasová), dvorak.k@fce.vutbr.cz (K. Dvořák), marek@sci.muni.cz (M. Slobodník), dalibor@sci.muni.cz (D. Všíanský), tomas.zikmund@ceitec.vutbr.cz (T. Zikmund), jiri.dluhos@tescan.cz (J. Dluhoš), rostislav.vana@tescan.cz (R. Váňa), jaroslav.bures@gmail.com (J. Bureš), jozef.kaiser@ceitec.vutbr.cz (J. Kaiser).

works deal mostly with the expansion of pure calcite grains, possibly also with the influence of various impurities on this quantity. This relatively frequently observed phenomenon is related to the volumetric changes of limestone during firing, e.g. a loss of compactness due to the development of net cracks, so called decrepitation.

The process of decrepitation has been investigated by various authors, especially from the viewpoint of the influence of a particle size [5]. This phenomenon makes some types of limestone absolutely unusable for the production of lime. A similar issue was observed in the case of flue gas desulphurization by the fluid combustion technology [6].

The only reasonable way to explain the “decrepitation” of limestones is to take into account the presence of fluid inclusions in sparry carbonate minerals, mostly calcite that is a coarse crystalline component of limestones. Fluid inclusions are common objects in natural minerals. They originate as defects during the growth of crystalline lattice leaving voids which are filled by ambient solution (fluids). Consequently, natural crystal/mineral phases precipitate from this solution. Sparry calcite in most limestones is formed from simple pore-filling cement among allochems (particles forming structural framework of limestones – intraclasts, oolites, fossils and pellets of microcrystalline calcite). The sparry calcite crystallizes from pore solutions and its amount differs according to a particular type of limestones. Thanks to the presence of a particular genetic type of calcite cement, it is possible to observe various properties and behaviour of limestone within industrial processing.

One of standard methods for investigation of nature of fluids trapped inside inclusions is optical microthermometry. This method is based on the phase transitions during temperature changes and also on the interpretation and thermodynamic calculations of fluid properties [7,8]. In studies of micro and nanostructures of rocks, nano-detection methods are applied. The scanning electron microscopy (SEM) is commonly used for obtaining information about the morphology of the sample surface [9]. The transmission electron microscopy (TEM) shows a connection between fluid inclusions and crystal structure defects [10]. A sample can be only observed layer by layer, which are removed by a focused ion beam (FIB). The electron microscopy can be further supported by a quantitative analysis such as energy dispersive X-ray spectroscopy or wavelength dispersive X-ray spectroscopy [10,11]. They provide a good resolution below 1 nm [12], thus they enable the observation of structures in more detail than the previously mentioned petrographic methods.

Density discontinuities in materials have been studied using X-ray computed tomography (CT) [13,14]. CT is a non-destructive method applied for 3D visualizations of materials' inner structure [15,16]. A sample is placed on a rotational table and scanned with the X-ray from many angles of rotation to get X-ray projections [17]. On the basis of these projections, virtual slices through the sample are reconstructed. The slices are stacked together to get 3D data. Gray values in slices correspond to the linear attenuation coefficient of the material. Based on different X-ray attenuations, different materials can be distinguished, segmented and quantified [18,19]. Modern laboratory CT devices are capable of reaching a voxel resolution (voxel is a volumetric element of CT data) of hundreds of nm [20,21]. Nevertheless, an observation with a small voxel size is only possible with adequately small samples due to a smaller field of view.

CT has been applied in various fields in geology, from hydrology, soil science, geodynamics up to planetary science. This technique is used to visualize the distribution and determination of a volume fraction in different phases of rock [22,23]. It has been applied for the detection of nano-inclusions of solids and fluid inclusions in diamonds [24], for the detection of cracks in rocks

[25] and even for the identification of phases inside fluid inclusions [26]. The CT is often combined with various petrographic methods [11,24,25].

This paper introduces a novel approach for investigation of the limestone's inner structure. It is focused on the identification and quantification of air voids and fluid inclusions, which play an important role in the decrepitation of limestone during firing. For this investigation, the laboratory-based X-ray computed tomography that provides a sufficiently high resolution and sensitivity to image fluid inclusions was applied. CT data reveal some parameters (such as the volume fraction of inclusions and their 3D distribution) which have not been determined so far by any other method. This approach was demonstrated on a selected limestone sample which was subjected to both chemical and mineralogical analyses and to microthermometry. To interpret the CT data correctly, also the two following techniques were used. Firstly, the light microscopy (LM) was used to verify the inclusions detected in CT data. Secondly, the serial-sectioning 3D analysis with X-ray energy dispersive spectroscopic analysis (3D EDS) by a scanning electron microscope equipped with a focused ion beam (FIB-SEM) was applied as a supplementary method for the determination of sample composition. As a consequence, this paper presents a unique combination of these three imaging techniques which were implemented on one sample in a special order showing a correlation between the outputs.

2. Materials

26 samples of limestones coming from various locations and geological units were collected. They differ in structure, petrographic character and chemical composition. Chemical and mineralogical analyses were made on all samples, the procedures were the same as described further in Section 3.1. The LM was applied on samples which might contain fluid inclusions. For the investigation, a sample which contained coarser cement of calcite (sparry calcite) and plenty of fluid inclusions was selected. The statement was based on the highest amount of chlorine and the LM (Fig. 1).

The examined sample was a hard, compact limestone classified as bioclastic grainstone according to Dunham classification [27]. It had been taken from a limestone deposit near Koněprusy, Czech Republic, from Lower Devonian sedimentary sequence of the Czech Karst area. The sample was prepared in several forms corresponding to the employed methods: homogenized powder of the rock

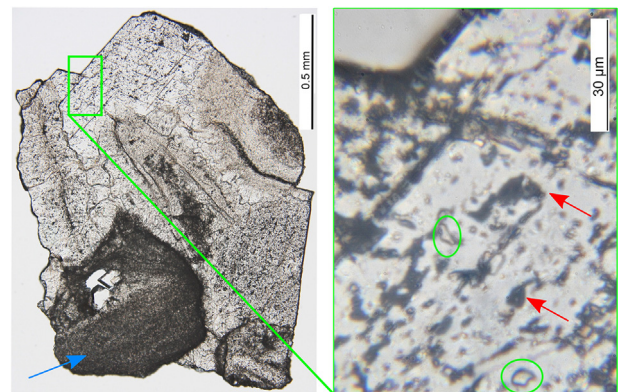


Fig. 1. Fragment of the double-sided polished limestone section from LM shows an enormous number of fluid inclusions spread within dotted brighter areas of sparry calcite. Among tiny black dots in calcite (defects in crystal lattice, pointed by red arrow), dominate the fluid inclusions (circled in green). Dark areas (pointed by the blue arrow) present allochems. (For interpretation of the references to colour in this figure legend, the reader is referred to the web version of this article.)

was used for a bulk chemical analysis and a double-sided polished 80 μm thin section for LM, microthermometry and CT.

3. Methods

Petrographic, mineralogical and chemical analyses together with microthermometry were performed to achieve a complete petrographic description of the sample. In order to examine the same piece of the sample, one thin section was scanned with the CT and an area rich in fluid inclusions selected with the LM (detail in Fig. 1) was examined with 3D EDS analysis.

3.1. Petrographic, mineralogical and chemical analysis

Fundamental petrographic and mineralogical observations of rocks were performed on thin sections with an optical microscope Olympus BX51. To avoid an inaccurate identification of fluid inclusions in the LM, a statistical evaluation was made followingly: the average number of inclusions was found out based on their counting in several focused planes in sectors $20 \times 20 \mu\text{m}^2$ throughout the sample and then recalculated to the area of interest $100 \times 70 \mu\text{m}^2$.

For the mineralogical analysis, it was necessary to remove CaCO_3 due to a high purity of the selected limestone. An insoluble residue was obtained by limestone dissolution in acetic acid using a slightly modified method according to Jeppsson and Dalton [28,29]. The total limestone dosage was 1500 g. The acetic acid concentration was 10% and was maintained by a pH measurement throughout the dissolution time. The total dissolution time was 3 months at a stable temperature of 21 $^\circ\text{C}$. After the limestone dissolution had been finished, the insoluble residue was washed several times with distilled water, dried at room temperature and analysed. A XRD analysis was carried out using a Panalytical Empyrean X-ray diffractometer with a Cu anode (current of 40 mA, voltage of 45 kV), 0.013° 2Theta step size, 298.09 s scan step time in continuous scanning mode. Data were processed with the HighScore+ software with PDF 2 and ICSD 2012 databases. Only qualitative analysis was performed.

To calculate the weight percent of major elements or oxides, a chemical analysis of the limestone samples was carried out using several supplementary methods: the gravimetric analysis, atomic absorption spectroscopy (AAS, instrument iCE™ 3500) and X-ray fluorescence spectroscopy (XRF, instrument Panalytical Axios). The method of the determination is always given for the relevant oxide/element in Table 1.

3.2. Microthermometry

Thin sections and doubly polished thin sections (thickness 80 μm) were prepared for fluid inclusion studies. The only relevant positions for an investigation of fluid inclusions were growth zones, short trails and clusters. Linkam stage THMSG600 mounted on Nikon Eclipse80i was used for microthermometric measurements calibrated by synthetic fluid inclusions. Measured temperatures were $(0.0 \pm 0.1)^\circ\text{C}$ (melting point of pure H_2O), $(-21.2 \pm 0.2)^\circ\text{C}$

$^\circ\text{C}$ (eutectic melting point of $\text{H}_2\text{O}-\text{NaCl}$) and $(-56.6 \pm 0.2)^\circ\text{C}$ (temperature of CO_2 melting in $\text{H}_2\text{O}-\text{CO}_2$ fluid system) of synthetic standards. The estimated accuracy of measurements on samples was within $\pm 0.1^\circ\text{C}$ during freezing runs. The melting temperature of ice (T_m) had to be measured to calculate salinity and also the eutectic temperature (T_e) to assess the fluid system composition. The salinity of solutions in aqueous inclusions was calculated according to Bodnar [30]. Programmes of the FLUIDS 1 [31] were used for calculations of fluid density.

3.3. 3D EDS analysis

The serial-sectioning 3D analysis with X-ray energy dispersive spectroscopic analysis (3D EDS) by a scanning electron microscope equipped with a focused ion beam (FIB-SEM) was applied on the area defined by the earlier results from the CT and LM. Then, an analysis using a TESCAN FERA 3 Xe^+ Plasma FIB-SEM [32] equipped with an EDAX Octane Elite energy-dispersive X-ray spectrometer was carried out. The sample had been carbon-coated in order to prevent charging artefacts. The region of interest (ROI) was identified on the basis of the correlative electron and light microscopy. The ROI was cropped by FIB (300 nA at 30 keV) to avoid shadowing and backscattering of analytical signal in the ROI surroundings. The sample surface was protected by placing a thin silicon mask on the top of it. This way, a clean FIB cross section without curtaining artefacts was obtained (Fig. 2).

The ROI was sliced in order to acquire 3D data (using 100 nA FIB current). A volume of $125 \times 125 \times 50 \mu\text{m}^3$ was gradually sliced off with a step of $0.5 \times 0.5 \times 0.5 \mu\text{m}^3$. Afterwards, each slice was analysed as follows: backscattered electron (BSE) image, EDS mapping and full X-ray spectra storage for each voxel. The electron and EDS data acquisition was done at 10 keV and 20 nA SEM beam current. During post-processing, from each slice the individual elemental maps for selected elements were extracted. HyperSpy toolbox [33] was used to obtain 3D elemental maps and then they were correlated with CT data. The 3D correlation was done using ORS Visual SI software.

3.4. X-ray computed tomography

The sample was scanned using the RIGAKU Nano3DX device with Mo target operating at 50 kV, $3300 \times 2500 \text{px}^2$ X-ray CCD camera and $0.27 \times 0.27 \mu\text{m}^2$ pixel size. An exposure time of 20 s was used, the number of projections was 800. Binning 2 was set (information from $2 \times 2 \text{px}^2$ area was summed up) to reach the linear voxel size of 0.53 μm . The tomographic reconstruction was realized using RIGAKU software. Data after reconstruction were filtered with nonlocal means filter for noise removal [34]. In CT data, a region of $456 \times 41 \times 259 \mu\text{m}^3$ (the total volume of area without outer air was $4.5 \times 106 \mu\text{m}^3$) was selected for further analysis in VGStudio Max 3.0. The darkest cavities were segmented by global thresholding, where the threshold was chosen manually by an operator. The minimum volume of cavity was set to 8 voxels. Furthermore, CT data were correlated with the 3D EDS analysis to determine several occurrences of Mg rich regions. These were seg-

Table 1

Chemical analysis of the limestone sample (LOI – loss of ignition, GA – gravimetric analysis, AAS – atomic absorption spectroscopy, XRF – X-ray fluorescence microscopy).

Element/oxide	wt [%]	Method	Element/oxide	wt [%]	Method
CaO	55.24	GA	K_2O	0.0039	GA
SiO_2	0.06	GA	SO_3	0.010	AAS
Al_2O_3	0.02	GA	Cl	62 [ppm]	GA
MgO	0.47	GA	Others	0.099	GA
Fe_2O_3	0.04	XRF	LOI (1000 $^\circ\text{C}$)	44.05	GA
Na_2O	0.007	GA			

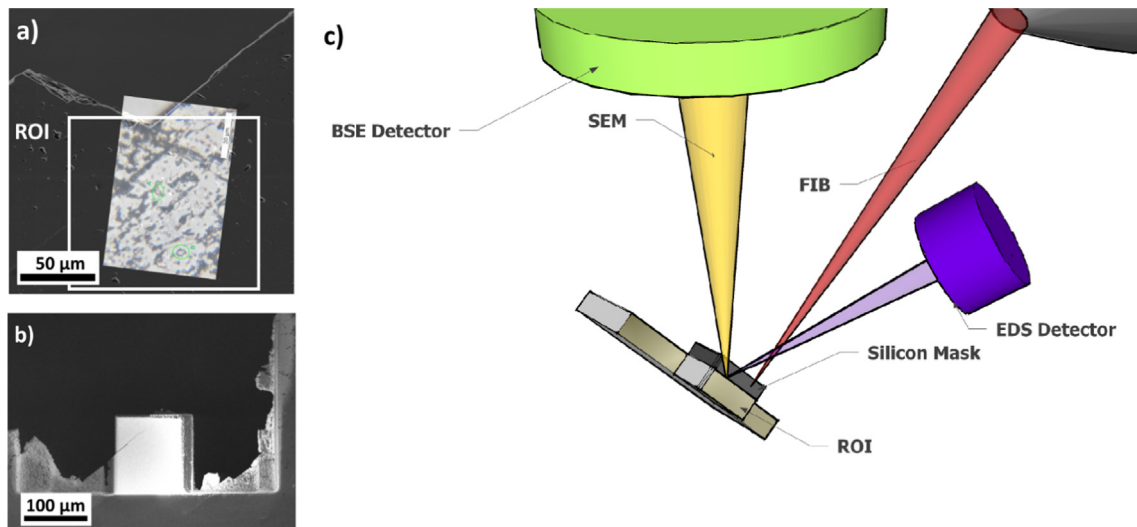


Fig. 2. 3D EDS analysis. a) Location of ROI using correlative SEM and LM image, b) preparation of ROI by FIB, c) 3D EDS static-acquisition geometry (ROI in cross section view), BSE means backscattered electrons.

mented by global thresholding, but only large areas were taken into account thanks to their sufficient contrast against surrounding calcite. The thresholding segmentation method was inaccurate in areas around air voids, therefore the region with a high content of Mg was manually corrected based on the correlation with 3D EDS analysis.

4. Results

4.1. Petrographic, mineralogical and chemical analysis

From LM images (Fig. 1), the number of inclusions in sparry calcite within the sample's investigated region with volume of $100 \times 70 \times 80 \mu\text{m}^3$ was determined. The number is between 80 and 200 inclusions which corresponds to 10^8 inclusions per cm^3 . The sample contained numerous tiny fluid inclusions with size up to 2–3 μm , only a few inclusions were of a size 5–10 μm . Their shape was rounded or irregular and they were rather randomly distributed. Fluid inclusions were one-phase and two-phase and there

was no difference in distribution and shape of inclusions of these two types.

A mineralogical analysis showed that the prevailing bioclasts in the sample were echinoderms and crinoids. Bryozoans, rugose corals and ostracodes were also common. Rugose corals, as well as the bryozoans, occurred as complete branches. Syntaxial calcite cement overgrowths appeared due to diagenesis. Calcite crystals reached the maximum size of about 2 mm. Depositional setting could be interpreted as shallow-marine, above the fair-weather wave base.

An XRD analysis of insoluble residue (Fig. 3) showed that minerals such as calcite and dolomite had been still presented in the sample after three months of dissolution, however, their content decreased enough to enable an identification of other phases. Common minerals in the samples were quartz, fluorapatite, goethite, illite/mica, kaolinite, orthoclase, gypsum, smectite (vermiculite/chlorite) and also pyrite.

According to the chemical analysis, the predominating chemical component was CaCO_3 . The content of CaCO_3 was higher than 98% (Table 1). A small amount of magnesium in form of MgCO_3 was

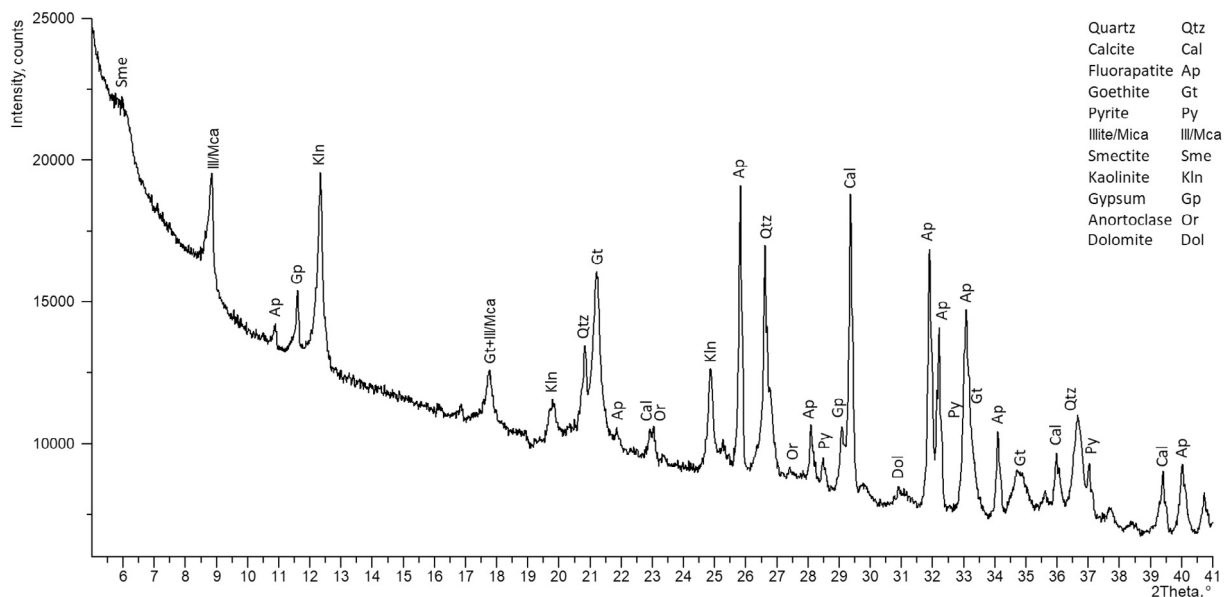


Fig. 3. Mineralogical analysis of the insoluble residue.

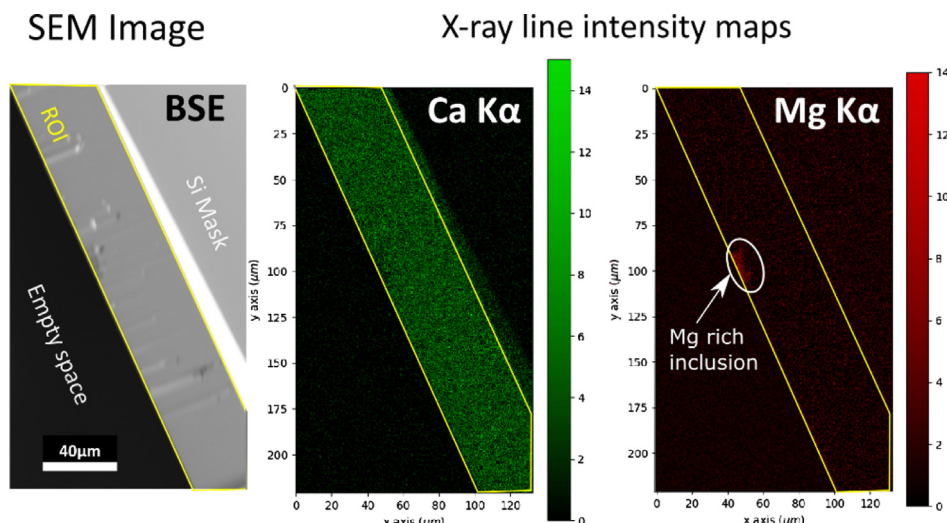


Fig. 4. 2D data output for a single FIB slice (ROI cross section): BSE – backscattered electron SEM image, Ca K α , Mg K α – EDS elemental maps extracted from the spectral data cube according to the selected peak intensity.

present as well. Some salt components such as Na⁺ and Cl⁻ were also detected, pointing out the presence of salt in fluid inclusions. Chemical analyses are in a good agreement with a mineral composition. Fairly pure limestone apparently contained a high amount of CaCO₃ and other minor and accessory mineral phases, as detected by XRD, which were responsible for other elements. A relatively ubiquitous dolomite contained some Mg, however Mg was a component in smectite/vermiculite/chlorite ((Mg, Fe⁺⁺, Al)₃(Al, Si)₄O₁₀(OH)₂·4(H₂O)) as well. Other discovered mineral phases contained also the following elements: quartz (SiO₂), illite/mica (KAl₂(Si₃Al)O₁₀(OH,F)₂), kaolinite (Al₂Si₂O₅(OH)₄), orthoclase (KAlSi₃O₈), gypsum (CaSO₄), pyrite (FeS₂) and goethite (Fe⁺⁺⁺O(OH)). Relatively high contents of chlorine and sodium denoted a presence of salt in the fluid inclusions.

4.2. Microthermometry

The majority of inclusions (80–90 %) contained a one-phase system only, i.e. they contained only liquid. By contrast, two-phase fluid inclusions contained liquid and vapour (L + V type). These facts indicate that fluids, which represent diagenetic conditions of the limestone, were trapped at temperature below +50 °C [7]. Cryothermometry was applied to obtain data on the composition and salinity of the fluids. Eutectic temperatures of the system were around -22 °C and -20 °C which indicates presence of the H₂O-NaCl and possibly H₂O-NaCl-KCl system as dominant components [35]. The temperature at which the last solid (ice) melts ranges between -0.3 °C and -0.9 °C which means that the salinity of aqueous fluids is between 0.5 and 1.5 mass% NaCl eq. [30]. In accordance with those salinities, a density of the aqueous solution inside the inclusions is between 1.0020 and 1.0094 g·cm⁻³.

4.3. 3D EDS analysis

The 3D EDS analysis showed presence of some individual Mg rich regions in a small area of the sample (Fig. 4). This method did not enable detection of the salt content of fluid inclusions due to their low salinity. The liquid evaporated immediately after opening of the inclusion and the size of remaining salt crystals was below the resolution limit.

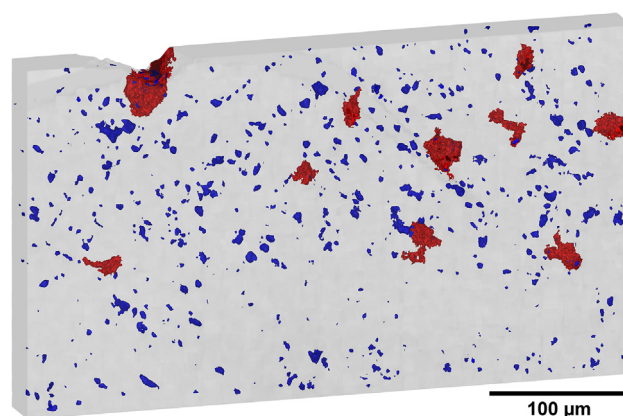


Fig. 5. 3D transparent render of CT data. Cavities are labelled by blue colour, magnesium rich regions are labelled by red colour. (For interpretation of the references to colour in this figure legend, the reader is referred to the web version of this article.)

4.4. X-ray computed tomography

The CT data of examined sample showed nearly a uniform distribution of cavities (Fig. 5). It was not possible to distinguish air voids from fluid inclusions, since they have similar gray values in CT data. These cavities were segmented and their total volume was determined in VGStudio MAX as $19.4 \times 10^3 \mu\text{m}^3$, resulting in 0.43 vol.% in volume of the examined region.

A stack of LM images was aligned with CT images so that the edges of the samples fitted (Fig. 6). Some fluid inclusions with the same shape and position as seen in LM were recognized in the CT data. According to CT analysis, there were 107 cavities within an area of $100 \times 70 \mu\text{m}^2$ (indicated in the Fig. 1).

To further verify the presence of fluid inclusions in the limestone sample, the CT data were correlated with the 3D EDS analysis (Fig. 7), but this method failed to show the distribution of inclusions. However, Mg rich regions were recognized in the CT data (Fig. 6d). The total volume of Mg rich area segmented in the CT data was $23.1 \times 10^3 \mu\text{m}^3$, resulting in 0.51 vol.%. According to the results from chemical and mineralogical analyses, these areas corresponded to dolomites.

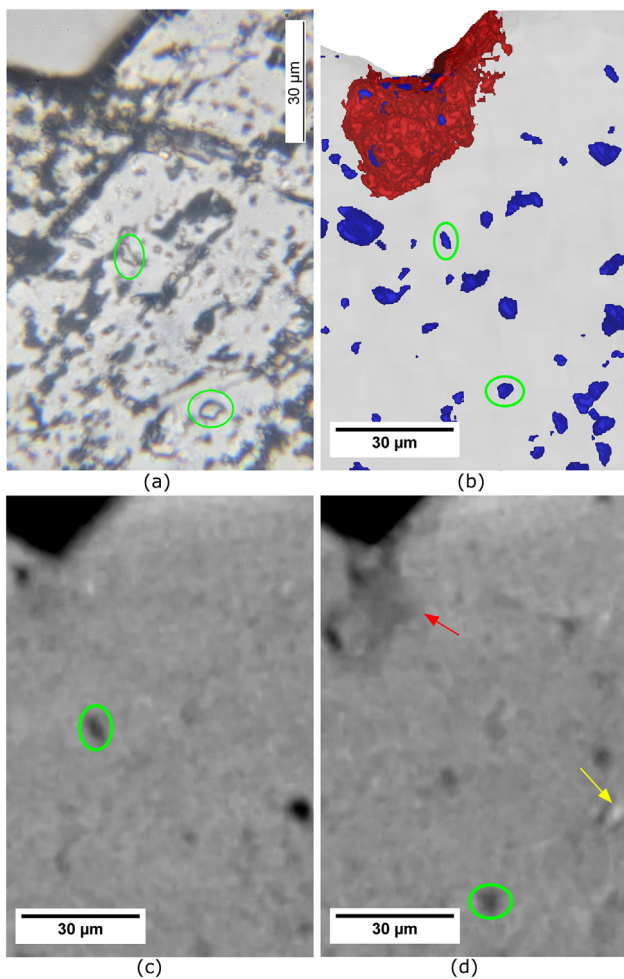


Fig. 6. (a) LM image: focused 2D images are stacked together, selected fluid inclusions are circled in green; (b) 3D transparent render of CT data. Blue colour represents air voids and fluid inclusions, red colour represents magnesium rich area; (c), (d) CT slices with selected fluid inclusions, red arrow marks magnesium, yellow arrow marks material with very high density. (For interpretation of the references to colour in this figure legend, the reader is referred to the web version of this article.)

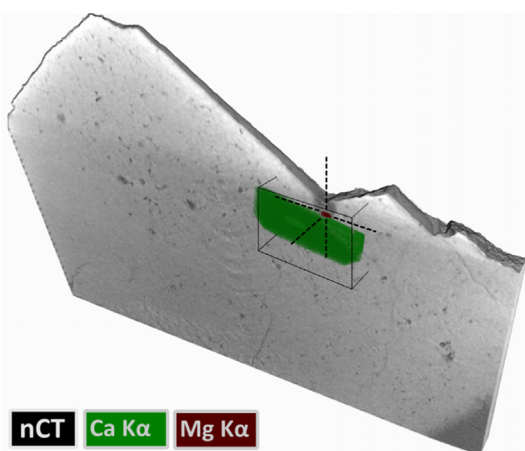


Fig. 7. 3D visualization of limestone plate as a correlative CT analysis (grayscale volume rendering) with 3D EDS elemental maps (Ca $K\alpha$ – green, Mg $K\alpha$ – red). Location of Mg rich region is marked by the cross. (For interpretation of the references to colour in this figure legend, the reader is referred to the web version of this article.)

Furthermore, some bright regions with significantly higher X-ray absorption were detected (Fig. 6d). These regions might contain some heavy elements (such as Fe), which was confirmed by the results of the chemical analysis.

5. Discussion

The number of cavities shown by the CT analysis corresponds to the LM result. 10^8 inclusions per cm^3 in minerals is considered rather high if a reference Roedder [37] is taken – 10^9 inclusions per cm^3 were reported in his study as a high number. Consequently, the volume of cavities derived by CT (0.43 vol.%) could be considered as rather high as well. All presented data explain behaviour of investigated limestone in firing process.

The smallest diameter of inclusion detectable by the CT is $1.3 \mu\text{m}$ (diameter of sphere with volume of 8 voxels). It is possible to study tiny individual inclusions with synchrotron CT devices [26], but the field of view is restricted to only one inclusion at a time. The larger field of view of laboratory-based CT allows to visualize a 3D distribution of a high amount of inclusions in the sample's volume.

In the proposed procedure, the LM is used as a method to get an overview of the sample and to select the region of interest for further study. But once the CT data are acquired, the selection of the region for further investigation is faster in comparison with the LM. It is because all inclusions, voids, cracks and grains from different materials are visible in 3D data of the sample. In LM, all the inclusions do not have to be visible due to the fractures along cleavage planes in the calcite structure. Besides that, some small fractures or grains may be confused with inclusions and the number of inclusions results in inaccurate number or could be undervalued.

The shape of the sample must be taken into account while planning an experiment as it affects quality of the CT data. For the sake of the experiment, the sample was polished in form of a thin section which was required for the LM analysis. However, such an asymmetric shape leads to an occurrence of artefacts in CT data. The fact that X-rays pass through very different thicknesses of the sample results in some false intensity gradients [36]. This is visible in the CT data in Fig. 7: the top of the sample is significantly brighter than the thicker part at the bottom although there is no big material difference. To avoid these artefacts, it is advisable to shape a sample to a cylinder form with no regular straight planes. However, this recommendation is applicable only for CT measurements. Breaking the sample and picking the most suitable fragment could often be sufficient and useful as it saves time and effort during sample preparation.

The 3D EDS analysis results do not confirm the presence of inclusions, however, the technique was used to identify a Mg rich region. In general, the application of this method helps with a material identification in CT data and with an interpretation of the 3D CT analysis results.

6. Conclusion

Fluid inclusions in sparry calcites as cement in limestones have an influence on its behaviour during industrial processing. When firing in shaft kilns, fluids trapped inside of fluid inclusions explode and expand (decrepitation), which results in a dense network of plenty of tiny fissures in rock and hence the limestones undergo some volumetric changes. This process is directly influenced by the amount and distribution of fluid inclusions. A high amount of fluid inclusions increases the decrepitation tendency of the limestone in the process of firing. A visualization and a direct study of fluid inclusions distribution in limestone predict its behaviour

during firing. The light microscopy is a standard technique of fluid inclusions' imaging. Using this technique, the visibility of fluid inclusions is restricted by disturbances of the calcite structure. The aim of this paper is to demonstrate the use of the laboratory-based X-ray computed tomography for a detection of fluid inclusions, a precise determination of their volume and a visualization of 3D distribution of inclusions in the volume of the sample.

A study of a hard, compact limestone from Koněprusy, Czech Republic is shown. The sample of a high purity limestone selected for investigation with CT contained a lot of fluid inclusions, a small amount of dolomite, clay minerals and Fe rich minerals which was confirmed by mineralogical and chemical analyses and microthermometry. To observe the fluid inclusions, one piece of the sample was studied using three methods: the CT, the LM for verification, and the 3D EDS analysis as a supplement method. The sample had to be prepared in the form of a thin section for the LM and the microthermometry although it was a very disadvantageous shape for the CT. The CT data show segmented cavities even though it is not possible to distinguish directly air voids from fluid inclusions. Images and results from all methods were correlated and some of fluid inclusions, dolomites and Fe-rich minerals such as pyrite and goethite were identified in the limestone CT data. Some of these inhomogeneities such as Mg and Fe rich areas were unidentified or only partially identified in the LM. The distribution of cavities and Mg rich areas in the volume was shown in a 3D model and their volume was determined based on the CT data.

This paper shows that the state of the art laboratory-based CT device is capable of a material analysis with the sufficient resolution to describe the fine inner structure of limestone. Unlike the commonly used optical microscopy, the CT requires an easier sample preparation and brings a non-destructive 3D characterization of materials' structure.

Conflict of interest

There are no known conflicts of interest.

Acknowledgements

This research was carried out under the project CEITEC 2020 (LQ1601) with financial support from the Ministry of Education, Youth and Sports of the Czech Republic under the National Sustainability Programme II. The work is further supported by National Sustainability Program under Grant LO1401 and by Preamium Academiae from CAS. Also, this work was financially supported by project No. LO1408 "AdMaS UP" – **Advanced Materials, Structures and Technologies**, supported by the Ministry of Education, Youth and Sports under "National Sustainability Programme I" and by project No. 15-08755S: "Study of the effects of samples preparation on the final properties of inorganic binders". Part of the work was carried out with the support of CEITEC Nano Research Infrastructure (MEYS CR, 2016–2019).

References

- [1] J.J. Wuhler, *Zement-Kalk-Gips Int.* 6 (1953) 354.
- [2] J. Wuhler, G. Rademacher, W. Lahl, *J. TIZ Int.* 80 (100) (1956).
- [3] J. Wuhler, *Über den Einfluss der Kristallgröße und von Fehlern auf die Reaktionsfähigkeit von Kalk*, Schriftenreihe des Bundesverbandes der Deutschen Kalkindustrie 10 (1970) 119–141.
- [4] A. Wolter, S. Hogewoning, *Vorhersage und Beeinflussung der Reaktivität von Branntkalk*. 2011. Forschungsbereich für die Forschungsgemeinschaft Kalk und Mörtel e.V.: 94 S, TU Clausthal.
- [5] D. Dollimore, J.G. Dunn, Y.F. Lee, B.M. Penrod, *The decrepitation of dolomite and limestone*, *Thermochim. Acta* 237 (1) (1994) 125–131, [https://doi.org/10.1016/0040-6031\(94\)85191-3](https://doi.org/10.1016/0040-6031(94)85191-3). ISSN 00406031.
- [6] P.M. Crnkovic, W.L. Polito, C.G. da Silva Filho, F.E. Milioli, J.D. Pagliuso, *The particle size effect on decrepitation during the thermal decomposition of limestones and coal*, *Química Nova* 27 (1) (2004) 58–61, <https://doi.org/10.1590/S0100-40422004000100012>. ISSN 0100-4042.
- [7] R.H. Goldstein, *Fluid inclusions in sedimentary and diagenetic systems*, *Lithos* 55 (1–4) (2001) 159–193, [https://doi.org/10.1016/S0024-4937\(00\)00044-X](https://doi.org/10.1016/S0024-4937(00)00044-X). ISSN 00244937.
- [8] A. Anderson, D.D. Marshall, I. Samson (Eds.), *Fluid Inclusions: Analysis and Interpretation*, Mineralogical Association of Canada, Ottawa, 2003. ISBN 09-212-9432-8.
- [9] M.R. Lee, C.L. Smith, *Scanning transmission electron microscopy using a SEM: Applications to mineralogy and petrology*, *Mineral. Mag.* 70 (5) (2006) 579–590, <https://doi.org/10.1180/0026461067050351>. ISSN 0026461x.
- [10] C. Viti, M.-L. Frezzotti, *Transmission electron microscopy applied to fluid inclusion investigations*, *Lithos* 55 (1–4) (2001) 125–138, [https://doi.org/10.1016/S0024-4937\(00\)00042-6](https://doi.org/10.1016/S0024-4937(00)00042-6). ISSN 00244937.
- [11] M. van Geet, R. Swennen, P. David, *Quantitative coal characterisation by means of microfocus X-ray computer tomography, colour image analysis and back-scattered scanning electron microscopy*, *Int. J. Coal Geol.* 46 (1) (2001) 11–25, [https://doi.org/10.1016/S0166-5162\(01\)00006-4](https://doi.org/10.1016/S0166-5162(01)00006-4). ISSN 01665162.
- [12] G. Möbus, B.J. Inks, *Nanoscale tomography in materials science*, *Mater. Today* 10 (12) (2007) 18–25, [https://doi.org/10.1016/S1369-7021\(07\)70304-8](https://doi.org/10.1016/S1369-7021(07)70304-8). ISSN 13697021.
- [13] V. Cnudde, M.N. Boone, *High-resolution X-ray computed tomography in geosciences: a review of the current technology and applications*, *Earth-Sci. Rev.* 123 (2013) 1–17, <https://doi.org/10.1016/j.earscirev.2013.04.003>. ISSN 00128252.
- [14] H.S. Barnard, A.A. Macdowell, D.Y. Parkinson, et al., *Synchrotron X-ray micro-tomography at the Advanced Light Source: Developments in high-temperature in-situ mechanical testing*, *J. Phys.* 849 (2017), <https://doi.org/10.1088/1742-6596/849/1/012043>. ISSN 1742-6588.
- [15] J. Friml, K. Procházková, G. Melnyk, T. Zikmund, J. Kaiser, *Investigation of Cheb relief intarsia and the study of the technological process of its production by micro computed tomography*, *J. Cult. Heritage* 15 (6) (2014) 609–613, <https://doi.org/10.1016/j.culher.2013.12.006>. ISSN 12962074.
- [16] M. Kaučeka, T. Zikmund, M. Tesarova, et al., *Oriented clonal cell dynamics enables accurate growth and shaping of vertebrate cartilage*, *ELife* 6 (2017), <https://doi.org/10.7554/eLife.25902>. ISSN 2050-084x.
- [17] J. Hsieh, *Computed tomography: principles, design, artifacts, and recent advances*. 2nd ed. Bellingham, Wash.: SPIE Press, 2009. ISBN 978-0-8194-7533-6.
- [18] F. Mees, R. Swennen, M. Van Geet, P. Jacobs, *Applications of X-ray computed tomography in the geosciences*, *Geol. Soc. London, Spec. Publ.* 215 (1) (2003) 1–6, <https://doi.org/10.1144/GSL.SP.2003.215.01.01>. ISSN 0305-8719.
- [19] W.D. Carlson, T. Rowe, R.A. Ketcham, M.W. Colbert, *Applications of high-resolution X-ray computed tomography in petrology, meteoritics and palaeontology*, *Geol. Soc. London, Spec. Publ.* 215 (1) (2003) 7–22, <https://doi.org/10.1144/GSL.SP.2003.215.01.02>. ISSN 0305-8719.
- [20] M. Kampschulte, A. Langheinrich, J. Sender, et al., *Nano-computed tomography: technique and applications*, *RöFo - Fortschritte auf dem Gebiet der Röntgenstrahlen und der bildgebenden Verfahren*. 188 (02) (2016) 146–154, <https://doi.org/10.1055/s-0041-106541>. ISSN 1438-9029.
- [21] F. Peyrin, P. Dong, A. Pacureanu, M. Langer, *Micro- and Nano-CT for the Study of Bone Ultrastructure*, *Curr. Osteoporosis Rep.* 12 (4) (2014) 465–474, <https://doi.org/10.1007/s11914-014-0233-0>. ISSN 1544-1873.
- [22] W.D. Carlson, *Three-dimensional imaging of earth and planetary materials*, *Earth Planet. Sci. Lett.* 249 (3–4) (2006) 133–147, <https://doi.org/10.1016/j.epsl.2006.06.020>. ISSN 0012821x.
- [23] L.A. Taina, R.J. Heck, T.R. Elliot, *Application of X-ray computed tomography to soil science: a literature review*, *Can. J. Soil Sci.* 88 (1) (2008) 1–19, <https://doi.org/10.4141/CJSS06027>. ISSN 0008-4271.
- [24] D.E. Jacob, R. Wirth, F. Enzmann, A. Kronz, A. Schreiber, *Nano-inclusion suite and high resolution micro-computed-tomography of polycrystalline diamond (framesite) from Orapa, Botswana*, *Earth Planet. Sci. Lett.* 308 (3–4) (2011) 307–316, <https://doi.org/10.1016/j.epsl.2011.05.056>. ISSN 0012821x.
- [25] S. Zabler, A. Rack, I. Manke, K. Thermann, J. Tiedemann, N. Harthill, H. Riesemeier, *High-resolution tomography of cracks, voids and micro-structure in greywacke and limestone*, *J. Struct. Geol.* 30 (7) (2008) 876–887, <https://doi.org/10.1016/j.jsg.2008.03.002>. ISSN 01918141.
- [26] K. Yoshida, T. Hirajima, A. Miyake, A. Tsuchiyama, S. Ohi, T. Nakano, K. Uesugi, *Combined FIB microsampling and X-ray microtomography: a powerful tool for the study of tiny fluid inclusions*, *Eur. J. Mineral.* 28 (2) (2016) 245–256, <https://doi.org/10.1127/ejm/2015/0027-2498>. ISSN 09351221.
- [27] R.J. Dunham, *Classification of Carbonate Rocks According to Depositional Texture*, In: HAM, William E. *Classification of Carbonate Rocks—A Symposium*. 1. American Association of Petroleum Geologists, 1962, pp. 108–121.
- [28] L. Jeppsson, R. Anehus, D. Fredholm, *The optimal acetate buffered acetic acid technique for extracting phosphatic fossils*, *J. Paleontol.* 73 (05) (1999) 964–972, <https://doi.org/10.1017/S002233600040798>. ISSN 0022-3360.
- [29] L.A. Dalton, T. Bosak, F.A. Macdonald, D.J.G. Lahr, S.B. Pruss, *Preservational and morphological variability of assemblages of agglutinated eukaryotes in cryogenic cap carbonates of northern Namibia*, *PALAIOS*. 28 (2) (2013) 67–79, <https://doi.org/10.2110/palo.2012.p12-084r>. ISSN 0883-1351.
- [30] R.J. Bodnar, *Revised equation and table for determining the freezing point depression of H₂O-NaCl solutions*, *Geochim. Cosmochim. Acta* 57 (3) (1993) 683–684, [https://doi.org/10.1016/0016-7037\(93\)90378-A](https://doi.org/10.1016/0016-7037(93)90378-A). ISSN 00167037.

- [31] R.J. Bakker, Package FLUIDS 1. Computer programs for analysis of fluid inclusion data and for modelling bulk fluid properties, *Chem. Geol.* 194 (1–3) (2003) 3–23, [https://doi.org/10.1016/S0009-2541\(02\)00268-1](https://doi.org/10.1016/S0009-2541(02)00268-1). ISSN 00092541.
- [32] T. Hrnčir, et. al. In: 38th ISTFA Conference Proceedings. 2012, s. 26.
- [33] F. de la Pena, et al. 2017, May 27. hyperspy/hyperspy: HyperSpy 1.3. Zenodo. <http://doi.org/10.5281/zenodo.583693>.
- [34] P. Coupe, P. Yger, S. Prima, P. Hellier, C. Kervrann, C. Barillot, An optimized blockwise nonlocal means denoising filter for 3-D magnetic resonance images, *IEEE Trans. Med. Imaging* 27 (4) (2008) 425–441, <https://doi.org/10.1109/TMI.2007.906087>. ISSN 0278-0062.
- [35] D.W. Davis, T.K. Lowenstein, R.J. Spencer, Melting behavior of fluid inclusions in laboratory-grown halite crystals in the systems NaCl-H₂O, NaCl-KCl-H₂O, NaCl-MgCl₂-H₂O, and NaCl-CaCl₂-H₂O, *Geochim. Cosmochim. Acta* 54 (3) (1990) 591–601, [https://doi.org/10.1016/0016-7037\(90\)90355-0](https://doi.org/10.1016/0016-7037(90)90355-0). ISSN 00167037.
- [36] J.P. Kruth, M. Bartscher, S. Carmignato, R. Schmitt, L. De Chiffre, A. Weckenmann, Computed tomography for dimensional metrology, *CIRP Ann.* 60 (2) (2011) 821–842, <https://doi.org/10.1016/j.cirp.2011.05.006>. ISSN 00078506.
- [37] E. Roedder, *Fluid Inclusions. Reviews in Mineralogy*. Washington D.C.: Mineralogical Society of America, 1984, p. 12.

Segmentation of multi-phase object applying trainable segmentation

Dominika Kalasova¹, Jan Masek², Tomas Zikmund¹, Pavel Spurny³, Jakub Haloda⁴, Radim Burget², Jozef Kaiser¹

¹Central European Institute of Technology, Brno University of Technology, 616 00 Brno, Czech Republic, email: dominika.kalasova@ceitec.vutbr.cz, tomas.zikmund@ceitec.vutbr.cz, jozef.kaiser@ceitec.vutbr.cz

²Brno University of Technology, Faculty of Electrical engineering, Department of Telecommunications, 616 00 Brno, Czech Republic, email: jan.masek@vutbr.cz, burgetrm@feec.vutbr.cz

³Astronomical Institute of the Czech Academy of Sciences, Fricova 298, 25165 Ondrejov, Czech Republic, email: pavel.spurny@asu.cas.cz

⁴Czech Geological Survey, Geologicka 6, Prague 5, Czech Republic, email: jakub.haloda@geology.cz

Abstract

In X-ray computed tomography (CT), post-processing of acquired data is necessary for obtaining quantitative information of the object. As initial step, it is necessary to segment different materials of the sample. The easiest and standardly used segmentation method is based on global thresholding according to histogram, but it works well only if histogram with multi-modal character where the intensity is distributed to the separate count peaks.

In this paper, we show the possibility of segmentation of tomographic data using trainable segmentation on data, where standard global thresholding fails. Trainable segmentation is a method that combines a collection of machine learning algorithms (decision tree, neural network, etc.) with a set of selected image features to produce binary pixel-based segmentation. This method is demonstrated on a sample of meteorite consisting of multiple phases (silicates, metals, sulphides), where knowledge of volumes of different materials is important for non-destructive study of modal phase composition, meteorite microstructures and identification of lithologies with different origin and evolution.

Keywords: segmentation, trainable segmentation, machine learning, image processing

1 Introduction

During the acquisition of a tomographic data, a lot of effort is usually invested to avoid the tomographic artifacts [1–3]. For obtaining quantitative information of these images, further postprocessing is no less important. In practice, a measured sample usually consists of multiple materials. Segmentation of individual materials is a first step for consequent processing.

There are many approaches to a segmentation described in the literature [4, 5]. One of the most common and easiest method is based on global thresholding according to histogram [6–8]. In the case of a sample consists of one type of metal, in histogram there are two easily separable peaks corresponding to air background and a metal. However, if there are no easily separable peaks corresponding to constituent materials, the segmentation becomes faulty. The tomographic artifacts like cone beam artifacts [9], beam hardening [10] or metal artifacts [11] can make segmentation even more complicated.

Other approaches use more complicated algorithms and can overcome these difficulties. Segmentation techniques including local adaptive thresholding, region growing methods, deformable surfaces, probabilistic fuzzy clustering, and image enhancement [4] can be applied directly. On the other hand, there are machine-learning algorithms like artificial neural networks, trainable segmentation, and deep learning methodologies requiring prior knowledge of the sample like shape, size and texture of phases [5, 12]. The most suitable method is selected according to type of sample, occurring artifacts etc. [13].

In this paper, we show a possibility of trainable segmentation method [14] for multiphase materials. In the case of these materials different phases have similar absorption properties and simple global thresholding fails. This method is widely used for house detection from satellite images [15]. Another example is segmentation of medical images used to find boundaries and cores of brain cell [16]. We used trainable segmentation method in combination with random forest machine learning algorithm, which uses classification and regression tree decision analysis [5, 17]. The principle is firstly to learn knowledge on the basis of training input with the combination of machine learning algorithms. Then the learned knowledge is applied on the rest of image data to obtain segmented result.

We demonstrate a trainable segmentation on a sample of meteorite [18]. The meteorite includes metal parts, troilite parts, air voids and cracks. For characterization of such a geological sample, it is necessary to segment those parts and determine their volume for calculation of modal contains of metal and troilite without any destruction of studied meteorite. Phases in such material are distributed irregularly and in small pieces, and, at some parts, do not have enough contrast to be segmented by global thresholding. We show that trainable segmentation provides results with higher accuracy than segmentation by global thresholding.



2 Materials and methods

The segmentation is demonstrated on a meteorite classified as chondrite, which fell near Zdar nad Sazavou, Czech Republic, on December 9, 2014 and was found on May 2, 2015. Different phases of meteorite are labeled on a tomographic slice in Fig. 1. The bright white areas represent metals, grey areas represent troilite. Besides, air voids (surrounded by material of meteorite) and cracks (connected to background) are shown.

CT measurement of meteorite was performed in X-ray micro and nano computed tomography laboratory in CEITEC BUT. The meteorite was scanned on a GE phoenix v|tome|x L240 device with cone-beam geometry, equipped with a 180 kV/15 W maximum power nanofocus X-ray tube and high contrast flat panel detector DXR250 with 2048×2048 pixel², and $200 \times 200 \mu\text{m}^2$ pixel size. Parameters of CT measurement are summed up in Table 1. The tomographic reconstruction was realized using GE phoenix datos|x 2.0 3D computed tomography software.

Acceleration voltage	X-ray tube current	Exposure time	Number of projections	Voxel size
150 kV	190 μA	750 ms	2000	$(28 \mu\text{m})^3$

Table 1: Parameters of tomographic measurement of the meteorite.

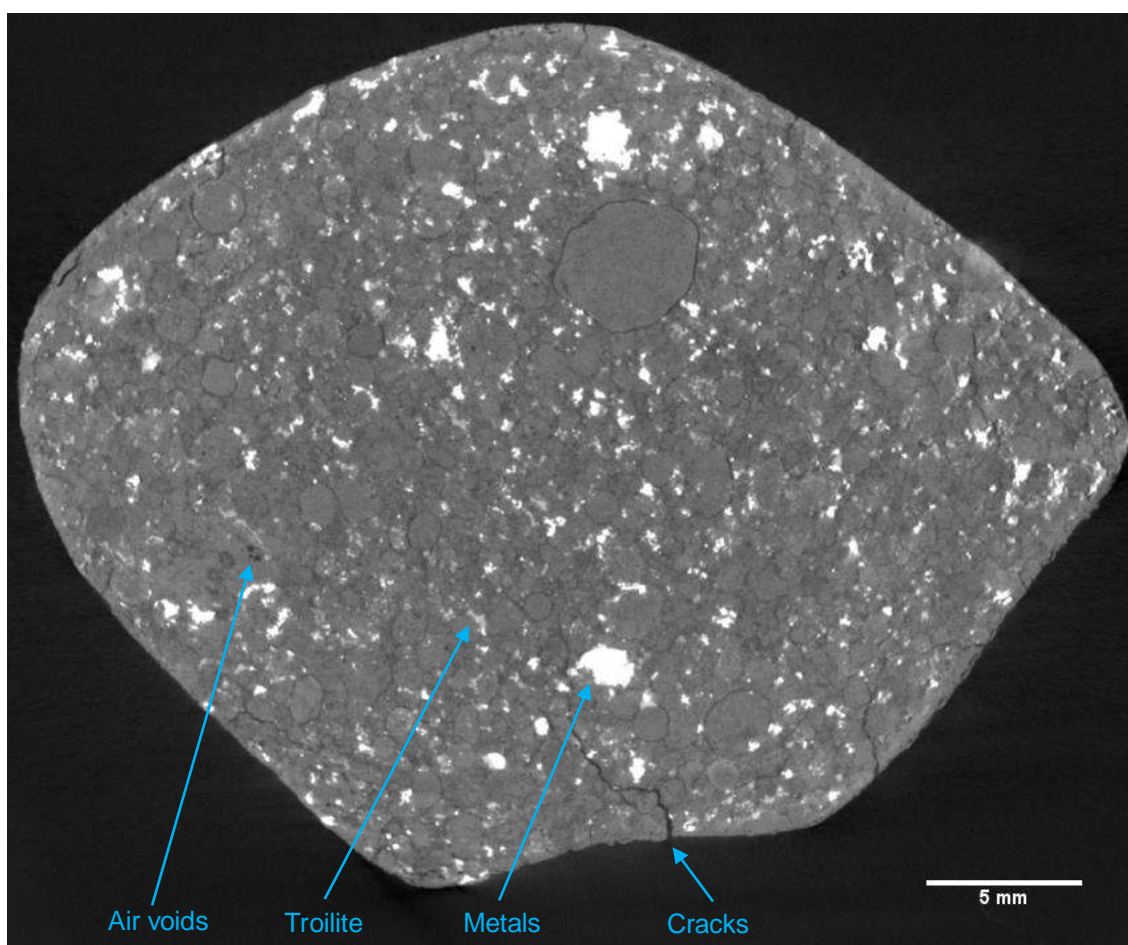


Figure 1: Tomographic slice of meteorite with description of different phases.

The segmentation of different parts of meteorite was done in several steps. In the first stage, the envelope of meteorite was created in VGStudio MAX using Surface determination tool, morphological operations and manual removal of some remaining internal parts. Secondly, air cavities were segmented from material of meteorite by global thresholding. The threshold in the histogram was placed into the valley after the first peak, which corresponded to air. Segmented air in the meteorite was divided into air voids and cracks using Pore analysis module within VGStudio MAX and morphological operations on regions.

Consequently, trainable segmentation was applied. All slices had to be normalized because of fluctuating light intensity to achieve higher accuracy in following segmentation. A trainable segmentation using algorithm of random forest considering not only intensity, but also surroundings of pixels, was used. We selected image where areas containing the segmented phase

were denoted as positive pixels and the rest of the image as negative pixels. Then this referenced image was used for training random forest model. For the evaluation of all images, the model was applied and results containing segmented troilite areas were saved.

3 Results and discussion

In histogram of tomographic data (Fig. 2), the first peak from the left corresponds to air the rest corresponds to the meteorite. There are no easily separable peaks corresponding to different phases in the material of the meteorite.

Fig. 3a) shows a detail of slice of the meteorite with metals and troilite. In Fig. 3b), the most appropriate threshold for global thresholding was set. Regions around metals were determined as troilite as well, because of their higher brightness, which led to much higher volume of troilite. Therefore we applied trainable segmentation on these phases (Fig. 3c), which delivered more accurate results.

The choice of a segmentation method has an influence on volumes of metals and troilite phases. Table 2 summarizes volumes and percentage by volume (total volume of meteorite was 12 887 mm³). Trainable segmentation gives smaller volumes than global thresholding, for troilite in particular.

The applied trainable segmentation works only on 2D slices, thus it cannot detect all cracks with thin and long shape, especially the ones which are perpendicular to examined slices. Therefore these were segmented by global thresholding (Fig. 4).

The segmentation based on thresholding in VGStudio MAX allows user to show and check a segmented region directly. It is easy and relatively fast for the user. Trainable segmentation provides more accurate results. On the other hand, it requires preliminary knowledge of appearance of the phases. Segmentation of all phases was limited by resolution, therefore it is possible that not all volume of all phases was detected.

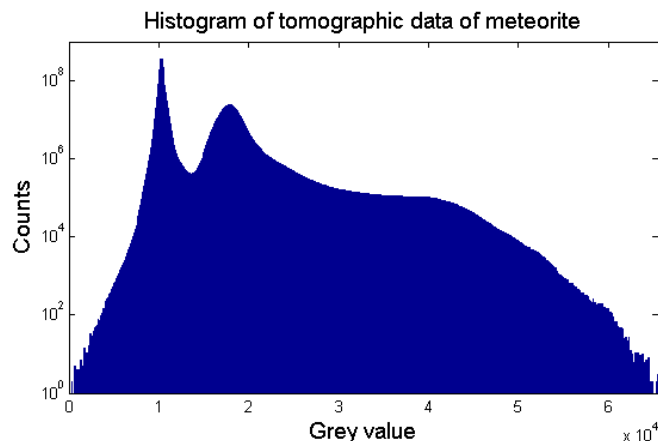


Figure 2: Histogram of tomographic data of meteorite.

	Global thresholding		Trainable segmentation	
	Volume	Percentage by volume	Volume	Percentage by volume
Metals	340 mm ³	2.6 vol%	261 mm ³	2.0 vol%
Troilite	998 mm ³	7.7 vol%	429 mm ³	3.3 vol%

Table 2: Volume and percentage by volume of metals and troilite phases in the meteorite (total volume of meteorite was 12 887 mm³).

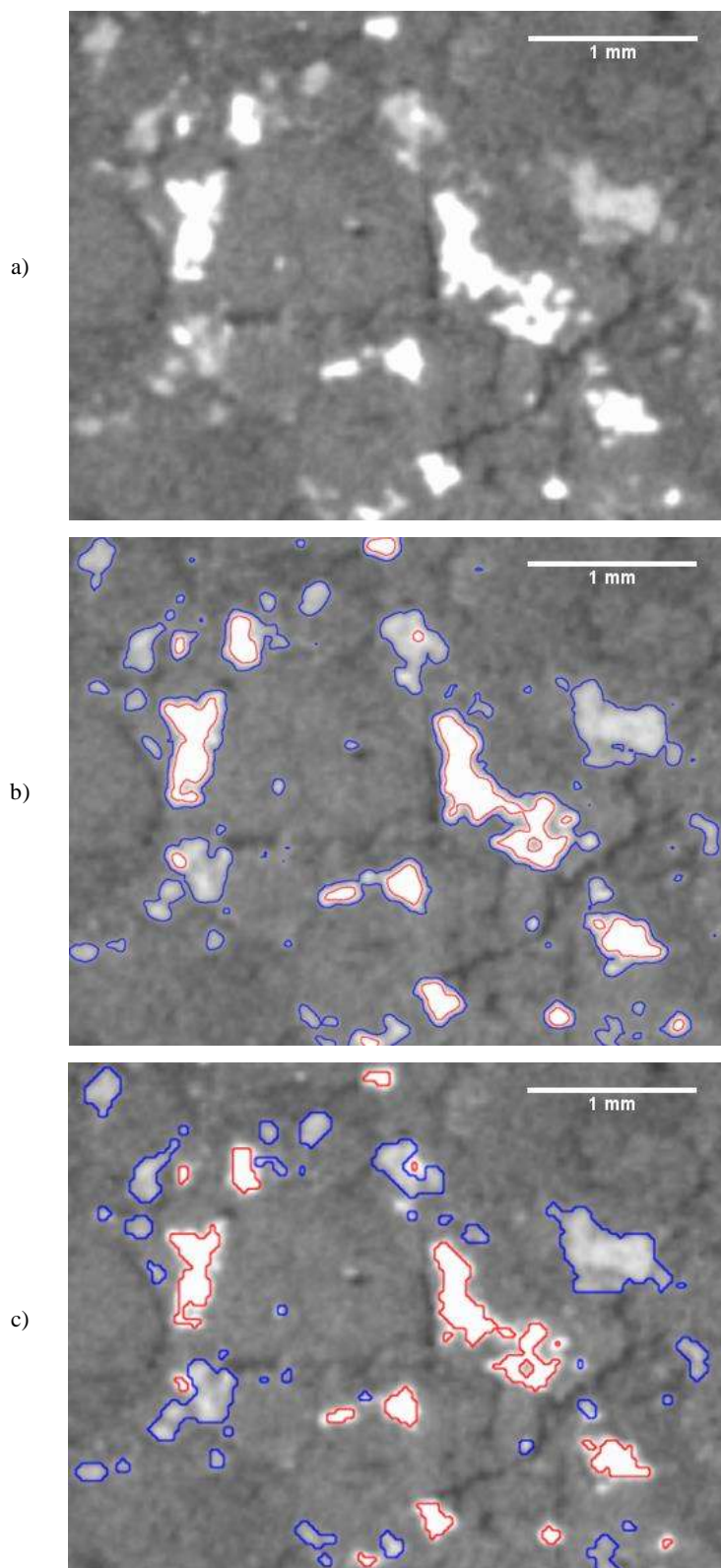


Figure 3: Slice through meteorite with results of segmentation. Red colour represents metals, blue colour represents troilite. a) Slice without segmentation, b) segmentation by global thresholding, c) trainable segmentation.

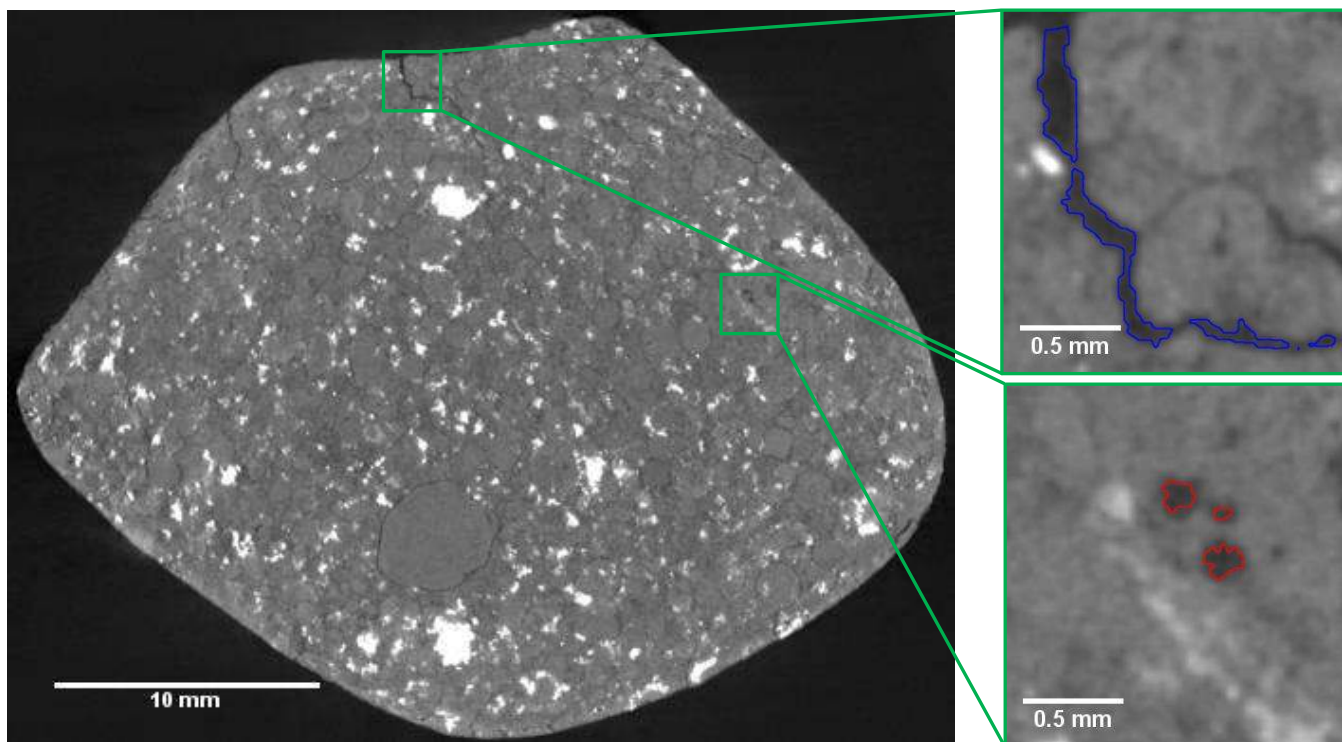


Figure 4: Slice through meteorite with detail of segmentation of air cavities. Red colour represents air voids, blue colour represents cracks.

4 Conclusion

Segmentation of multiphase materials becomes difficult when different phases have similar absorption properties and therefore do not have enough contrast to be distinguished easily. This situation is common for geological samples, where phases are distributed irregularly and in small volumes.

The method of global thresholding is a quick and easy method for segmentation if the threshold value is chosen in accordance with histogram shape. Although nowadays software provides extended options considering local surroundings of segmented region, this procedure is not sufficient for segmentation of multiphase materials such as geological samples. In these materials, different phases with similar densities do not show enough contrast to be distinguished. This brings a faulty identification of individual materials and numbers of their volume.

According to our study, the trainable segmentation is more accurate method for segmentation since it is using preliminary knowledge of appearance of different phases. The application of this method is demonstrated on a small piece of meteorite and results are compared to standard global thresholding approach. Differences of the segmentation results from both methods were imaged using a selected cross-section and the volumes of individual phases were quantified. Trainable segmentation resulted in smaller volumes of materials in comparison with global thresholding.

However, the used trainable algorithm still does not fit well for segmentation of CT data, because it is applied separately on individual slices and does not take into account volumetric character of data. Cracks characterized by thin and long shape and oriented perpendicularly to the examined slices could not be detected. For this reason, the trainable segmentation had to be combined with thresholding for determination of volume of air voids and cracks.

Acknowledgements

This research was carried out under the project CEITEC 2020 (LQ1601) with financial support from the Ministry of Education, Youth and Sports of the Czech Republic under the National Sustainability Programme II. The work is further supported by National Sustainability Program under grant LO1401 and by Preamium Academiae from CAS.

References

- [1] ANAS, Emran M. Abu, Jae G. Kim, Soo Y. Lee, Md. K. Hasan, Comparison of Ring Artifact Removal Methods using Flat Panel Detector Based CT Images, *BioMedical Engineering OnLine*, Vol. 10, no. 72, 2011.
- [2] BARRET, Julia F., Nicholas KEAT, Artifacts in CT: Recognition and Avoidance, *Radiographics*, Vol. 24, 2004. DOI: 10.1148/rg.246045065
- [3] BOAS, F. Edward, Dominik FLEISCHMANN, CT artifacts: causes and reduction techniques, *Imaging in Medicine*, Vol. 2, no. 2, 2012. DOI: 10.2217/iim.12.13.

- [4] IASSONOV, Pavel, Thomas, GEBRENEGUS, Markus TULLER, Segmentation of X-ray computed tomography images of porous materials: A crucial step for characterization and quantitative analysis of pore structures, *Water Resources Research*, Vol. 45, no. 9, 2009. DOI: 10.1029/2009WR008087.
- [5] PHAM, Dzung L., Chenyang XU, Jerry L. Prince, Current Methods in Medical Image Segmentation, *Annual Review of Biomedical Engineering*, Vol. 2, pp. 315-337, 2000. DOI: 10.1146/annurev.bioeng.2.1.315
- [6] SAHOO, P. K., S. Soltani, A. K. C. Wong, A Survey of Thresholding Techniques, *Computer Vision, Graphics, and Image Processing*, Vol. 41, no. 2, 1988. DOI: 10.1016/0734-189X(88)90022-9.
- [7] SEZGIN, Mehmet, Bülent SANKUR, Survey Over Image Thresholding Techniques and Quantitative Performance Evaluation, *Journal of Electronic Imaging*, Vol. 13, no. 1, 2004.
- [8] AARLE, van Wim, Kees Joost BATENBURG, Jan SIJBERS, Optimal Threshold Selection for Segmentation of Dense Homogeneous Objects in Tomographic Reconstructions, *IEEE Transactions on Medical Imaging*, Vol. 30, no. 4, 2011. DOI: 10.1109/TMI.2010.2104328
- [9] POLAN, Daniel F., Samuel L. BRADY, Robert A. KAUFMAN, Tissue Segmentation of Computed Tomography Images using a Random Forest Algorithm: a Feasibility Study, *Physics in Medicine and Biology*, Vol. 61, 2016.
- [10] SCHULZE, Ralf Kurt, Willy, Dorothea BERND, Bernd DHOEDT, On Cone-beam Computed Tomography Artifacts Induced by Titanium Implants, *Clinical Oral Implants Research*, Vol. 21, no. 1, 2010. DOI: 10.1111/j.1600-0501.2009.01817.x.
- [11] MEGANCK, Jeffrey A., Kenneth M. KOZLOFF, Michael M. THORTON, Stephen M. BROSKI, Steven A. GOLDSTEIN, Beam Hardening Artifacts in Micro-computed Tomography Scanning can be Reduced by X-ray Beam Filtration and the Resulting Images can be Used to Accurately Measure BMD, *Bone*, Vol. 45, no. 6, 2009. DOI: 10.1016/j.bone.2009.07.078
- [12] KALENDER, W. A., R. HEBEL, J. EBERSBERGER, Reduction of CT artifacts caused by metallic implants, *Radiology*, Vol. 164, no. 2, 1987. DOI: 10.1148/radiology.164.2.3602406
- [13] SHARMA, Neeraj, Lalit M. AGGARWAL, Automated Medical Image Segmentation Techniques, *Journal of Medical Physics*, Vol. 35, no. 1, 2010. DOI: 10.4103/0971-6203.58777.
- [14] ARGANDA-CARRERAS, Ignacio, Srinivas C. TURAGA, Daniel R. BERGER, et al., Crowdsourcing the creation of image segmentation algorithms for connectomics, *Frontiers in Neuroanatomy*, Vol. 9, 2015. DOI: 10.3389/fnana.2015.00142. ISSN 1662-5129.
- [15] MASEK, J.; BURGET, R.; UHER, V. IMMI, Interactive Segmentation Toolkit, In *Engineering Applications of Neural Networks, Communications in Computer and Information Science*, Heidelberg: Springer Berlin Heidelberg, p. 380-387, 2013. ISBN: 978-3-642-41012- 3. ISSN: 1865- 0929.
- [16] BURGET, R.; UHER, V.; MASEK, J., Trainable Segmentation Based on Local-level and Segment- level Feature Extraction, In *IEEE International Symposium on Biomedical Imaging*, 1. Barcelona: p. 17-24, 2012. ISBN: 978-1-4673-1118- 2
- [17] BREIMAN, Leo, Random forests, *Machine learning*, Vol. 45, no. 5, 2001. DOI: 10.1023/A:1010933404324.
- [18] SPURNY, Pavel, Instrumentally documented meteorite falls: two recent cases and statistics from all falls, *Asteroids: New Observations, New Models*, Proceedings of the International Astronomical Union, IAU Symposium, Volume 318, pp. 69-79, 2015. DOI: 10.1017/S1743921315009746

Determination of porosity from tomographic data of hydroxyapatite scaffold-like structures

Dominika Kalasova^{*}, Tomas Zikmund, Premysl Stastny, Martin Trunec, Jozef Kaiser

^{*}dominika.kalasova@ceitec.vutbr.cz



Central European Institute of Technology
Brno University of Technology
Brno, Czech Republic

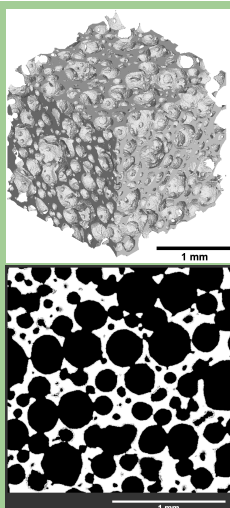


Abstract

In many fields, researchers take advantage of knowledge of material's porosity. For obtaining quantitative information of single, enclosed cavities, a lot of methods have been developed. The situation gets complicated when pores are interconnected within the structure. This is the case of foams and scaffolds, which are used in modern biology research for tissue engineering.

X-ray computed microtomography (μ CT) is a nondestructive method for 3D imaging of materials. For getting quantitative information about porosity in foams or scaffolds scanned with μ CT, many software offer various approaches. In this work, different software for pore analysis are compared. As a testing sample, a tomographic data of hydroxyapatite foam for bone replacement were used. It was scanned on GE phoenix L240 with linear voxel size 5 μ m. The material was segmented from background using Otsu method implemented in ImageJ.

Figure 1: 3D render (up) and slice (down) of segmented μ CT data of hydroxyapatite foam. Grey (in the 3D render) or white (in the slice) correspond to the material, the background colour corresponds to the air.



X-ray computed tomography

X-ray computed tomography (CT) is a nondestructive method for imaging of inner structure of materials. The sample is placed between the X-ray tube and the detector. A lot of projections from different angles of rotation of the sample are recorded. From these projections, slices through the sample are reconstructed to get 3D data. Grey values in slices correspond to linear attenuation coefficient of material.

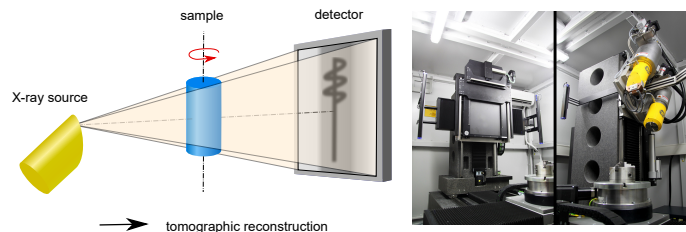


Figure 2: Scheme of X-ray computed tomography setup. **Figure 3:** CT device GE phoenix L240.

CT scan of an object visualizes its inner structure. It is possible to get a slice through an object in arbitrary direction. Based of different X-ray attenuation, and therefore different grey levels of various structures in CT data, it is possible to segment and further analyze these structures. Apart from visualization, analyses such as pore analysis, wall thickness analysis, and dimensional measurements can be carried out.

Results

Pore3D

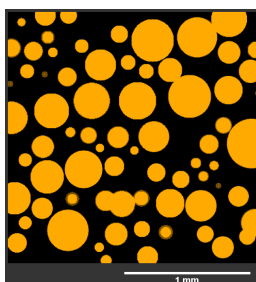
Type of software: open source for commercial IDL.

Version: Pore 3D 1.0 [1], IDL 7.0.

Result: Sizes and list of pores and joins between them ("Throats"). Skeleton visualizing connectivity of the pore space. Pore and throats space are available as a binary mask, which can be opened and visualized in VGStudio MAX.

Usage: Requires knowledge of basic programming.

Figures: Pores are marked with orange, throats with green and skeleton with blue.



VGStudio MAX

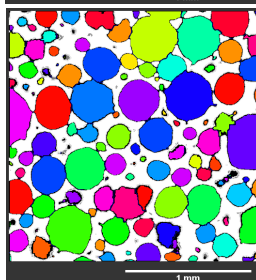
Type of software: commercial programme.

Version: 3.0. [2]

Result: Volume, list and advanced statistics of pores and contact surfaces between them ("Faces"). Thickness map of the material matrix (Strut thickness). 3D renders of analysis are available.

Usage: Easy usage, although choice of right parameters in analysis settings might be difficult.

Figures: Pores are marked with random colours for pores visualization. Faces are marked with blue colour.



MAVI

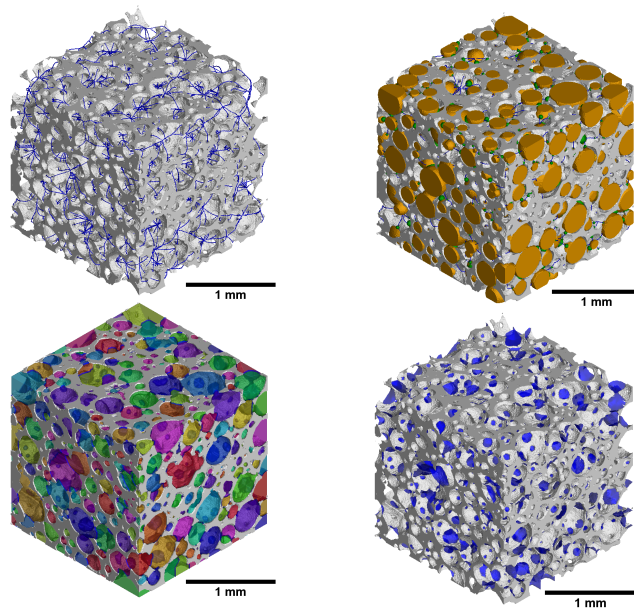
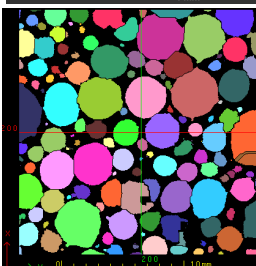
Type of software: commercial programme.

Version: 1.4.1. [3]

Result: Size and basic statistics of pores and contact surfaces between them ("Faces"). 3D renders of analysis are not available.

Usage: More complicated procedures for analysis, less user-friendly software.

Figure: Pores are marked with random colours for pores visualization.



Program	Number	Total volume of pores		Average pore volume
		mm ³	%	mm ³
VGStudio MAX	1946	5.6	70	0.0029
MAVI	2362	5.6	71	0.0024
Pore3D	917	3.7	46	0.0022

Table 1: Comparison of pore analysis of CT data of hydroxyapatite foam from different software (total volume of the examined sample was 8.00 mm³).

Summary

Different softwares for pore analysis of CT data of hydroxyapatite foam were compared. VGStudio and MAVI work on similar principle (the pore space is divided into individual pores based on input parameters) and provide similar analysis results. Pore3D creates skeleton and fits maximal spheres at joints, therefore detects less number of pores. Distances between joints (throats) are visualized by spheres of the same size. In comparison with VGStudio MAX, MAVI offers additional filtering and various morphological operations to obtain more precise results, but in this version lacks some basic features like 3D rendering of result analysis. VGStudio MAX offers additional analyses and the best visualization of results. All software show similar average pore volumes. Pore3D provides different pores number and volume than MAVI and VGStudio MAX, because it works on another principle. From this short comparison, the determination of porosity of the sample is not clearly defined and should be confirmed with another quantitative method.

Acknowledgement

This research was carried out under the project CEITEC 2020 (LQ1601) with financial support from the Ministry of Education, Youth and Sports of the Czech Republic under the National Sustainability Programme II.

References

- [1] F. Brun, L. Mancini, P. Kasae, S. Favretto, D. Drossi, G. Tromba. Pore3D: A software library for quantitative analysis of porous media. Nuclear Instruments and Methods in Physics Research A, vol. 615, nr. 3, pp. 326-332. 2010.
- [2] <https://www.volumegraphics.com/en/products/vgstudio-max.html>
- [3] <http://www.itwm.fraunhofer.de/en/departments/image-processing/microstructure-analysis/mavi.html>